

---

Theses and Dissertations

---

Spring 2010

# Modeling caveolar sodium current contributions to cardiac electrophysiology and arrhythmogenesis

Ian Matthew Besse  
*University of Iowa*

Copyright 2010 Ian Matthew Besse

This dissertation is available at Iowa Research Online: <http://ir.uiowa.edu/etd/463>

---

## Recommended Citation

Besse, Ian Matthew. "Modeling caveolar sodium current contributions to cardiac electrophysiology and arrhythmogenesis." PhD (Doctor of Philosophy) thesis, University of Iowa, 2010.  
<http://ir.uiowa.edu/etd/463>.

---

Follow this and additional works at: <http://ir.uiowa.edu/etd>



Part of the [Applied Mathematics Commons](#)

MODELING CAVEOLAR SODIUM CURRENT CONTRIBUTIONS TO  
CARDIAC ELECTROPHYSIOLOGY AND ARRHYTHMOGENESIS

by

Ian Matthew Besse

An Abstract

Of a thesis submitted in partial fulfillment of the  
requirements for the Doctor of Philosophy  
degree in Applied Mathematical and Computational Sciences  
in the Graduate College of  
The University of Iowa

May 2010

Thesis Supervisor: Assistant Professor Colleen Mitchell

## ABSTRACT

Proper heart function results from the periodic execution of a series of coordinated interdependent mechanical, chemical, and electrical processes within the cardiac tissue. Central to these processes is the action potential - the electrochemical event that initiates contraction of the individual cardiac myocytes. Many models of the cardiac action potential exist with varying levels of complexity, but none account for the electrophysiological role played by caveolae - small invaginations of the cardiac cell plasma membrane. Recent electrophysiological studies regarding these microdomains reveal that cardiac caveolae function as reservoirs of 'recruitable' sodium ion channels. As such, caveolar channels constitute a substantial and previously unrecognized source of sodium current that can significantly influence action potential morphology. In this thesis, I formulate and analyze new models of cardiac action potential which account for these caveolar sodium currents and provide computational venues in which to develop and test new hypotheses. My results provide insight into the role played by caveolar sodium currents in regulating the electrodynamics of cardiac myocytes and suggest that in certain pathological cases, caveolae may play an arrhythmogenic role.

Abstract Approved: \_\_\_\_\_  
Thesis Supervisor

\_\_\_\_\_  
Title and Department

\_\_\_\_\_  
Date

MODELING CAVEOLAR SODIUM CURRENT CONTRIBUTIONS TO  
CARDIAC ELECTROPHYSIOLOGY AND ARRHYTHMOGENESIS

by

Ian Matthew Besse

A thesis submitted in partial fulfillment of the  
requirements for the Doctor of Philosophy  
degree in Applied Mathematical and Computational Sciences  
in the Graduate College of  
The University of Iowa

May 2010

Thesis Supervisor: Assistant Professor Colleen Mitchell

Copyright by  
IAN MATTHEW BESSE  
2010  
All Rights Reserved

Graduate College  
The University of Iowa  
Iowa City, Iowa

CERTIFICATE OF APPROVAL

---

PH.D. THESIS

---

This is to certify that the Ph.D. thesis of

Ian Matthew Besse

has been approved by the Examining Committee for the thesis requirement for the Doctor of Philosophy degree in Applied Mathematical and Computational Sciences at the May 2010 graduation.

Thesis Committee: \_\_\_\_\_  
Colleen Mitchell, Thesis Supervisor

\_\_\_\_\_  
Erwin F. Shibata

\_\_\_\_\_  
Tong Li

\_\_\_\_\_  
Bruce P. Ayati

\_\_\_\_\_  
Rodica Curtu

## ACKNOWLEDGMENTS

I would like to thank my advisor, Colleen Mitchell, and my collaborators, Erwin Shibata and Thomas Hund, for their expert guidance throughout my dissertation research process. The extent to which I have become a scholar of mathematics, of computational science, and of electrophysiology over the last six years is due in large part to their tutelage and mentorship. I would also like to express my sincere appreciation to the other members of my thesis committee, Tong Li, Bruce Ayati, and Rodica Curtu, each of whom has graciously shared their time, expertise, and support with me during my graduate studies. Additionally, I wish to acknowledge the financial support I have received as a graduate teaching assistant and VIGRE trainee from the University of Iowa Mathematics Department and from the NSF VIGRE grant DMS-0602242. This generous support was of great assistance to me during my graduate studies. Finally, I wish to thank my wife, Jana, whose unwavering love, encouragement, and understanding throughout my dissertation research have played a crucial role in this accomplishment.

## TABLE OF CONTENTS

LIST OF TABLES . . . . .	vi
LIST OF FIGURES . . . . .	vii
CHAPTER	
1 INTRODUCTION . . . . .	1
1.1 A Brief Overview of Cardiac Electrophysiology . . . . .	1
1.1.1 Biophysics of Excitable Membranes . . . . .	1
1.1.2 Nernst Potential . . . . .	3
1.1.3 Cardiac Action Potential . . . . .	6
1.1.4 Excitation-Contraction Coupling . . . . .	8
1.2 Mathematical Modeling of Electrophysiology . . . . .	11
1.2.1 Membrane-Transporter Pairing as an RC Circuit . . . . .	11
1.2.2 The Hodgkin-Huxley Formalism . . . . .	13
1.2.3 The Pandit and Mitchell-Schaeffer Models . . . . .	17
1.3 Caveolae and the $\beta$ -Adrenergic Response . . . . .	19
1.3.1 Caveolae Structure . . . . .	19
1.3.2 Caveolae Function . . . . .	22
1.3.2.1 PKA-Dependent $\beta_1$ -Adrenergic Signaling Pathway . . . . .	23
1.3.2.2 PKA-Independent $\beta_1$ -Adrenergic Signaling Pathway . . . . .	24
1.4 Specific Objective . . . . .	27
2 CAVEOLAE-INCLUSIVE MODEL . . . . .	29
2.1 Introduction to the Caveolae-Inclusive Model . . . . .	29
2.2 Cardiac Caveolar Density . . . . .	30
2.3 Formulation of the Caveolae-Inclusive Model . . . . .	37
2.3.1 Model Assumptions and Framework . . . . .	39
2.4 Simulation Protocols . . . . .	43
2.4.1 Voltage-Clamp Protocol . . . . .	43
2.4.2 Action Potential Protocols . . . . .	44
2.5 Results . . . . .	45
2.5.1 Replication of Experimental Data . . . . .	45
2.5.2 Caveolar Effects on Action Potential Morphology . . . . .	47
2.5.3 Caveolar Effects on Upstroke Velocity and APD . . . . .	48
2.5.3.1 Dichotomous Time Scales Approach . . . . .	52
2.5.3.2 Stable Manifold Approach . . . . .	54

2.6	Conclusions . . . . .	58
3	SIMPLIFIED THREE-VARIABLE MODEL . . . . .	62
3.1	Introduction to the Three-Variable Model . . . . .	62
3.2	Mitchell-Schaeffer Two-Current Model . . . . .	63
3.3	Formulation of the Three-Variable Model . . . . .	66
3.3.1	Preliminary Parameter Selection . . . . .	68
3.3.1.1	Selecting $\overline{\tau_K}$ . . . . .	70
3.3.1.2	Selecting $v_p$ , $\overline{\tau_{po}}$ , and $\overline{\tau_{pc}}$ . . . . .	71
3.3.1.3	Selecting $\overline{\tau_{Ca}}$ . . . . .	74
3.3.1.4	Selecting $v_h$ , $\overline{\tau_{ho}}$ , and $\overline{\tau_{hc}}$ . . . . .	74
3.3.1.5	Selecting $\overline{\tau_{Na}}$ . . . . .	77
3.3.2	Preliminary Results . . . . .	79
3.3.2.1	Optimization of Parameter Values . . . . .	80
3.3.3	Comparison with the Pandit Model . . . . .	83
3.4	Simulation Protocols . . . . .	87
3.4.1	Voltage-Clamp Protocol . . . . .	87
3.4.2	Action Potential Protocols . . . . .	88
3.5	Results . . . . .	89
3.5.1	Replication of Experimental Data . . . . .	90
3.5.2	Caveolar Effects on Action Potential . . . . .	92
3.6	Asymptotic Analysis . . . . .	95
3.7	Conclusions . . . . .	100
4	STOCHASTIC CAVEOLAE MODEL . . . . .	102
4.1	Introduction to the Stochastic Caveolae Model . . . . .	102
4.2	Mathematical Modeling . . . . .	104
4.2.1	Conceptual Foundations . . . . .	104
4.2.2	Caveolar Opening as a Poisson Process . . . . .	106
4.2.2.1	The Poisson Random Variable . . . . .	106
4.2.2.2	First Opening Probability Density Function . . . . .	107
4.2.2.3	The Poisson Rate Parameter . . . . .	109
4.2.3	Formulation of the Stochastic Caveolae Model . . . . .	110
4.3	Simulation Protocols . . . . .	113
4.3.1	Voltage-Clamp Protocol . . . . .	113
4.3.2	Action Potential Protocol . . . . .	117
4.4	Results . . . . .	118
4.4.1	Voltage-Clamp Results . . . . .	118
4.4.2	Action Potential Morphology Results . . . . .	120
4.5	Stochasticity in the Three-Variable Model . . . . .	126
4.6	Conclusion . . . . .	130

5	CONCLUSIONS AND FUTURE WORK . . . . .	133
5.1	Summary of Key Findings . . . . .	134
5.1.1	Derivation of Caveolae Density Estimates . . . . .	134
5.1.2	Caveolar Sodium Current Increases Upstroke Velocity	135
5.1.3	Linear Upstroke Velocity Dependence . . . . .	136
5.1.4	Caveolar Dysfunction as LQTS Mechanism . . . . .	137
5.2	Future Work . . . . .	138
5.2.1	Single-Caveola Model . . . . .	138
5.2.1.1	Conceptual Foundations . . . . .	139
5.2.1.2	Formulation of a Single-Caveola Model . . . . .	141
5.2.1.3	Preliminary Work with a Deterministic Model	141
5.2.1.4	Evolution of the Closed Bulk Caveolar Space	142
5.2.2	The Capacitance Question . . . . .	144
5.2.3	A Spatially-Extended Model . . . . .	145
	APPENDIX . . . . .	148
	REFERENCES . . . . .	153

## LIST OF TABLES

### Table

3.1	Optimized parameter values for the physiologically scaled three-variable model. . . . .	84
4.1	Values of the variables at a superthreshold fixed point of the Pandit system. . . . .	124

## LIST OF FIGURES

Figure		
1.1	Idealized drawing of the phospholipid bilayer and membrane proteins that make up the cell's plasma membrane. (Image released to public domain for unrestricted use by its creator, Mariana Ruiz Villarreal.) . . . . .	2
1.2	Typical human cardiac action potential morphology exhibiting the rapid upstroke phase carried primarily by a strong inward sodium current, a long plateau phase resulting from opposing calcium influx and potassium efflux, and a repolarization phase carried primarily by an outward potassium current which drives the action potential back down toward its resting state. The relative lengths of the arrows represents the strength of the current. . . . .	9
1.3	Equivalent circuit diagram in which the cell membrane can be thought of as a plate capacitor in parallel with ion channels which act as variable resistors. Note that the driving force on each ion has an electrical and chemical component, collectively referred to as its associated electrochemical gradient. . . . .	12
1.4	Electron micrograph of an adult rat ventricular cell showing caveolae (arrow in inset) around the perimeter. Caveolae are typically spherical in shape with a diameter of 40 - 100 nm and can accumulate in a clustered structure resembling a bunch of grapes (rosettes). Under normal conditions, the necks of these caveolae are pinched tightly closed preventing any interaction between the extracellular and intracaveolar environments. Thus, any ion channels embedded in the caveolar membrane are isolated from electrical events occurring on the sarcolemma. $\beta$ -adrenergic stimulation causes these necks to open presenting caveolar membrane proteins to the sarcolemma. (Image courtesy of Erwin Shibata, Molecular Physiology and Biophysics, University of Iowa). . . . .	21
1.5	Two pathways of $\beta$ -adrenergic modulation of cardiac sodium current. (Image courtesy of Erwin Shibata, Molecular Physiology and Biophysics, University of Iowa). . . . .	26
2.1	Fluid compartment diagrams for the caveolae-inclusive model in each of its two modes. . . . .	41

2.2 Sodium current-voltage curves generated by the Pandit and caveolae-inclusive models exhibit the same general shape as those produced experimentally by Lu et al[1] and Palygin et al[2]. Model parameters were modified to simulate the low sodium concentrations at which the Lu et al[1] and Palygin et al[2] experiments were conducted. In particular, values of  $\gamma_{Na} = 2.2$  pS and  $\overline{g_{Na}} = 0.13$   $\mu$ S were substituted while all other parameter values were the same as those listed in the appendix. The solid black curve depicts baseline sodium current response to the voltage-clamp protocol generated by the unmodified Pandit model, while the two blue curves depict the augmented response due to caveolae which have opened to present the sarcolemma with additional sodium channels. The blue curves were generated using the caveolae-inclusive model. The results indicate that 20000 open caveolae will increase maximum peak sodium current by approximately 34%, and 25000 open caveolae leads to an increase of approximately 42%. . . . . 46

2.3 Action potential morphology using the Pandit model with and without caveolar sodium current. Notice that the inclusion of 25000 open caveolae results in an approximately 5.2% increase in peak overshoot of the action potential. Less evident from the graph is a 29% increase in maximum upstroke velocity, an important factor in determining the speed of the excitatory wave through the cardiac tissue. Action potential duration, however, appears to be relatively unaffected by the additional sodium conductance introduced by the open caveolae. . . . . 49

2.4 Both maximum upstroke velocity and action potential duration exhibit a nearly linear dependence upon the number of open caveolae on the sarcolemma. A. In the case of the maximum upstroke velocity, there exists a strong positive relationship with each 1000 additional open caveolae lending a 1.15% increase to maximum upstroke velocity from baseline. B. In the case of action potential duration, the relationship is negative and substantially weaker. Even the addition of 25000 open caveolae yields only about a 1% decrease in APD. . . . 50

- 2.5 Graphs of the maximum upstroke velocity as a function of the number of open caveolae from the caveolae-inclusive model simulations (blue solid line) and using the dichotomous time scales approach which results in equation (2.14) (red dashed-dotted line). Here I have assumed that  $m(V_m) = m_\infty(V_m)$ ,  $h(V_m) \equiv h_0$ , and  $j(V_m) \equiv j_0$ . A severe discrepancy is evident using this method for analytically deriving the expected linear relationship between maximum upstroke velocity and number of open caveolae. Obviously, assuming such fast changes in  $m$  and neglecting the changes in the  $h$ -gate and  $j$ -gate values during the upstroke, as well as the contributions of other ionic currents, has resulted in a substantial over estimation of the maximum upstroke velocity. . . . . 55
- 2.6 These figures show the trajectories of the activation variable  $m$  and inactivation variable  $h$  as functions of membrane potential during the upstroke phase of the action potential for various initial values of each. Trajectories were produced by initiating action potentials by instantaneously depolarizing the membrane to potentials of -50 (red dashed curves), -45 (green dotted curves), and -40 mV (blue solid curves). It appears that there does exist an attractive stable manifold to which the trajectories in  $vm$ -space tend, but no such attractive manifold in  $vh$ -space. For reference the curves  $m_\infty(V_m)$  (black dotted curve) and a curve which offers a good fit to the stable manifold (black solid curve) are superimposed in  $vm$ -space. Note that this clearly shows  $m_\infty(V_m)$  is a poor approximation to the actual trajectories in  $vm$ -space. . . . . 56
- 2.7 A discrepancy is still evident using this method for analytically deriving the expected linear relationship (black dotted line) between maximum upstroke velocity and number of open caveolae, but the discrepancy is much less pronounced than it was in Figure 2.5 (Linear relationship using dichotomous time scales approach is reproduced here as the red dash-dotted line). While this stable manifold approach for analytically extracting the linear relationship appears to work much better than the dichotomous time scales approach, there are obviously subtle interactions between membrane potential and the gating mechanisms involved in the upstroke of the action potential that have still not been captured by this method. . . . . 59

3.1 This figure shows an action potential generated by the Mitchell-Schaeffer two-current model. Note that it exhibits the characteristic four-phase morphology - upstroke, plateau, repolarization, recovery - of all cardiac action potentials, but has a much more pronounced plateau phase than a rat action potential since this model was designed to simulate the frog cardiac action potential. Nevertheless, the simplicity and analytic accessibility of this model makes it an appealing choice for use as a guide in developing a simplified model of rat cardiac action potential. . . . . 64

3.2 This plot shows the time course of the membrane permeability to calcium (—) in the Pandit model given by (3.7) and that of the three-variable model (- - -) given by (3.8) provided the time course of the membrane potential is the time course of the Pandit-model generated action potential. In (3.8)  $\bar{p}(t)$  is defined as in (3.9). The parameter values  $v_p \approx 0.8$ ,  $\bar{\tau}_{po} \approx 0.0005$  seconds, and  $\bar{\tau}_{pc} \approx 0.009$  seconds appear to offer a very close fit between (3.7) and (3.8) suggesting that these parameter values are near those which would optimize the overall fit of the calcium currents in the two models. . . . . 73

3.3 This plot shows the time course of the membrane permeability to sodium (—) in the Pandit model given by (3.15) and that of the three-variable model (- - -) given by (3.19) provided the time course of the membrane potential is the time course of the Pandit-model generated action potential. In (3.19),  $\bar{h}(t) = 0.68e^{-\frac{t}{\bar{\tau}_{hc}}}$  with  $\bar{\tau}_{hc} = 0.00045$  seconds and  $\frac{0.45}{\max\left(\bar{h}\left(\frac{\bar{v} + 81.36}{147.36}\right)^2\right)} = 11.25$ . It appears that this choice of time constant provides a reasonably good fit between (3.7) and (3.19) suggesting that this parameter value is near the value which would optimize the overall fit of the sodium currents in the two models. However, one major difference between the two plots is evident at the beginning of their time courses. In the Pandit model, the membrane permeability to sodium at the time of the stimulus is essentially zero, while in the three-variable model this permeability instantaneously jumps to approximately 0.35 upon the arrival of the stimulus, a phenomenon which is discussed further in the text. . . . 78

3.4	These plots illustrate that our initial estimates for the parameter values yield results that are quite consistent with those of the Pandit model. The action potential morphologies, calcium current time courses, and potassium current time courses are all similar in their peaks and proportions. The sodium current generated by the three-variable model, however, is larger than that generated by the Pandit model by a factor of about 4 or 5. . . . .	81
3.5	With parameter values optimized using the method explained in the text the three-variable model can generate an action potential morphology that is nearly identical to that produced by the Pandit model. Additionally, the underlying sodium, potassium, and calcium currents exhibit nearly identical morphologies between the two models. The only differences between these results are the 0.6 msec delay in action potential initiation in the three-variable model (discussed in the text) and the slightly slower decay to extinction of the potassium and calcium currents in the three-variable model. In other important respects such as peak voltage overshoot, action potential duration, and maximum upstroke velocity, there is good agreement between the models. . . . .	86
3.6	This figure illustrates the effects that caveolar sodium current has on sodium current-voltage curves in the three-variable model (A) and compares them to the corresponding changes seen in the caveolae-inclusive model (B). The solid black curves depicts baseline sodium current response to the voltage-clamp protocol, while the blue curves depict the augmented response due to caveolae which have opened to present the sarcolemma with additional sodium channels. In the case of the three-variable model, the dotted and dashed blue curves were generated by selecting $\kappa = 1.37$ and $\kappa = 1.42$ , respectively. These choices of $\kappa$ correspond to the inclusion of 20000 and 25000 open caveolae on the cell's sarcolemma and result in the desired 34% and 42% increases to maximum peak sodium current that were seen with the caveolae-inclusive model. . . . .	91
3.7	Action potential morphology using the three-variable model with and without caveolar sodium current. . . . .	93

- 3.8 The relationships between upstroke velocity and  $\kappa$  and between action potential duration and  $\kappa$  in the three-variable model exhibit similarities with the corresponding relationships seen using the caveolae-inclusive model. A. Maximum upstroke velocity exhibits a nearly linear dependence upon  $\kappa$  just as seen with the caveolae-inclusive model. However, the same proportional increase in sodium current in the three-variable model results in a much greater increase in maximum upstroke velocity than in the caveolar-inclusive model. In the case of the maximum upstroke velocity, there exists a strong positive relationship. An increase of 0.0168 to  $\kappa$  is equivalent to the addition of 1000 open caveolae in the caveolae-inclusive model. Such an increase to  $\kappa$  in the three-variable model yields a 3.6% increase to maximum upstroke velocity from baseline. This is a substantially greater rate of increase than the corresponding 1.2% increase seen with the caveolae-inclusive model. B. As with the caveolae-inclusive model, APD is relatively unaffected by increases in sodium current in the three-variable model. In the three-variable model APD as a function of  $\kappa$  exhibits a slight upward trend with the addition of 25000 caveolae (i.e.  $\kappa = 1.42$ ) leading to only a 1% increase in APD. . . . . 94
- 3.9 The computationally derived relationship between maximum upstroke velocity and  $\kappa$ -value shown along with the analytically extracted linear relationship between maximum upstroke velocity and  $\kappa$ -value. Notice that there is very close agreement between the two graphs suggesting that the dominant relationship between upstroke velocity and caveolar sodium current is, in fact, linear. . . . . 99
- 4.1 A late, persistent sodium current was observed when the membrane potential was conditioned at -140 mV and then stepped up to a sustained membrane potential of -20 mV. A. Model generated sodium current from sodium channels on the sarcolemma (---), sodium current from sodium channels in stochastically opening caveolae (···), and the sum of these two sodium currents (—). B. Experimental data from Vatta et al[3] showing significant persistent sodium currents. Note the difference in time scales between the two figures. Since the model assumes caveolar sodium current only occurs during a caveolae's first opening after stimulus, the caveolar current will persist as long as there are caveolae left which have not already opened. In contrast, the experimental results in B. demonstrate a sodium current which persists for hundreds of milliseconds with no indication of decaying to zero. (Panel B reproduced from the 2006 paper by Vatta et al[3] with permission from the sole copyright holder, Wolters Kluwer-Lippincott Williams & Wilkins.) . . . . . 119

- 4.2 Effects of stochasticity in caveolar openings on action potential morphology and afterdepolarization formation. Graphs of the action potential morphologies with (A) 14000 caveolae for a range of  $\lambda$ -values and (B) the associated action potential duration dependence on  $\lambda$ . Early afterdepolarizations, along with more substantial delays in repolarization, do occur for a range of  $\lambda$ -values when the number of caveolae is increased to 16000 (C & D). Increasing the number of caveolae further to 18000 leads to early afterdepolarizations, and in a range of  $\lambda$ -values, the system settles into a new equilibrium (E). This complete extinguishing of the repolarization phase shows up as a discontinuity in the graph of action potential duration dependence on  $\lambda$ -value (F). . . . . 122
- 4.3 This figure illustrates the differences in the time courses of the ionic currents that result from fixing  $\lambda$  at an intermediate value and varying the number of caveolae. In this scenario,  $\lambda$  is fixed at 15 and plots of A. the transient sodium current,  $I_{Na}$ , B. the potassium current,  $I_t$ , C. the caveolar sodium current,  $I_{cav}$ , and D. the L-type calcium current,  $I_{CaL}$ , associated with 14000, 16000 and 18000 stochastic caveolae have been superimposed upon one another. Notice that when 16000 and 18000 caveolae are included, calcium reactivation occurs leading to a single early afterdepolarization with 16000 caveolae and a series of afterdepolarizations with 18000 caveolae. In the case of 18000 caveolae, repolarization is delayed long enough for the slower variables to enter the basin of attraction for a new fixed point and the system settles into a new equilibrium state. . . . . 125
- 4.4 This figure shows the effects that incorporating stochastic caveolae into the three-variable model has on the simulated action potential morphology. As in Figure 4.2 action potentials have been plotted for select values of  $\lambda$  (A) and action potential duration as a function of  $\lambda$ -value (B). In this case,  $\kappa = 1.42$  was used to simulate the inclusion of 25000 stochastic caveolae in our simulated cell. These plots indicate a noticeable delay in repolarization as expected from the same computational experiment using the physiologically detailed model of stochastic caveolae. However, the delays in repolarization generated by the physiologically detailed model were substantially more pronounced even with far fewer stochastic caveolae than are the delays seen in this figure. Furthermore, the maximum delays occurred at  $\lambda$ -values that are an order of magnitude greater than those at which the maximum delays occur using this model. Also the system does not tend towards a secondary equilibrium for any caveolar densities or  $\lambda$ -values as did the physiologically detailed model. . . . . 128

4.5	The graph of $\tau_h$ showing high variability. . . . .	130
5.1	Evolution of the caveolar state from close at -80 mV steady state values . . . . .	143
5.2	Accounting for capacitance in the caveolae-inclusive model. It appears that even accounting for the added capacitance maximum upstroke velocity would be increased, but less so if the caveolar diameters were assumed to be 100 nm as opposed to 50 nm. Note that doubling the diameter of the caveolae would result in a four-fold increase in the surface area of the caveolar membrane added to the sarcolemma. While the increase in capacitance due the larger caveolae is still not enough to counteract the increase to maximum upstroke velocity due to the additional sodium current, it is enough to noticeably slow changes in $\frac{dv}{dt}$ late in the action potential leading to a slight increase in APD. . . . .	146

## CHAPTER 1 INTRODUCTION

### 1.1 A Brief Overview of Cardiac Electrophysiology

#### 1.1.1 Biophysics of Excitable Membranes

Certain cell types in the human body such as neurons and muscle cells possess a plasma membrane that is endowed with unique electrical properties allowing for the generation of so-called action potentials, transiently self-sustaining departures of the membrane potential from a locally stable resting value. Such cells are said to possess an excitable membrane and are referred to as excitable cells. The membrane forms a barrier around the cell, separating the intracellular environment from the extracellular environment and is composed of a thin ( $\approx 7.5$  nm thick[4]) double layer of phospholipid molecules. This phospholipid bilayer functions not only as a physical barrier, but also as an electric capacitor separating charges carried by ions in solution on either side of the membrane. Embedded within the membrane are numerous proteins, some of which, called ion transporters, facilitate the movement of ions from one side of the membrane to the other and in doing so allow for the production of small transmembrane electric currents. These ion transporters come in three main varieties: ion channels, ion pumps, and coupled transporters called ion exchangers. When open, ion channels selectively allow for the free flow of ions down their electrochemical gradients. Ion pumps use the cellular energy

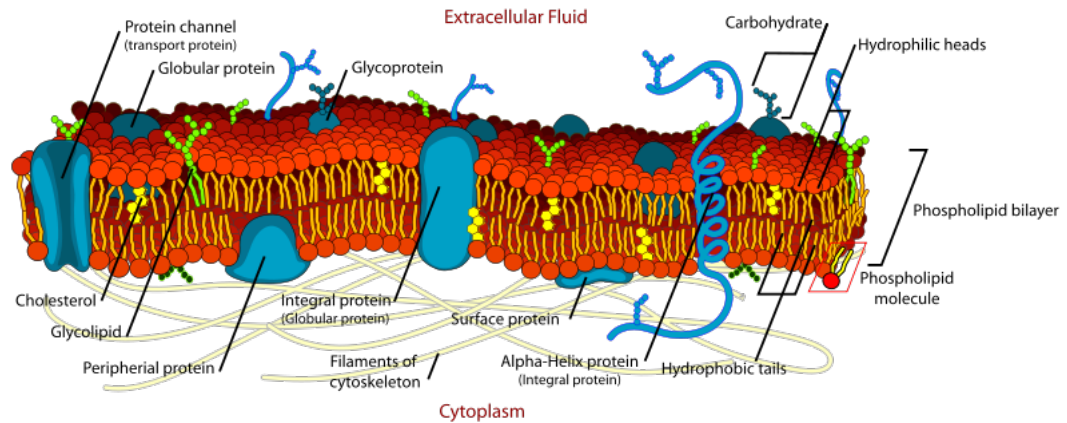


Figure 1.1: Idealized drawing of the phospholipid bilayer and membrane proteins that make up the cell's plasma membrane. (Image released to public domain for unrestricted use by its creator, Mariana Ruiz Villarreal.)

source adenosine triphosphate to move ions across the membrane against their electrochemical gradient. Ion exchangers harness the flow of one ion species along its electrochemical gradient to drive ions of another species across the membrane against their electrochemical gradient[5]. Figure 1.1 is an idealized version of the plasma membrane showing the variety of proteins, including ion transporters, embedded within it.

In the absence of an external stimulus, the membrane of most types of excitable cells tend toward a steady-state in which a fixed electric potential - typically about  $-80$  mV in cardiac cells - exists across the membrane. This steady state membrane potential is called the resting membrane potential. The resting membrane potential is the result of differential concentrations of sev-

eral types of ions in the intracellular and extracellular environments, selective permeability of the resting membrane to these ions, and the homeostatic actions of ion pumps and exchangers within the membrane. Depolarization of the membrane beyond a threshold, however, results in voltage- and time-dependent changes in the membrane's permeability that initiate a cascade of rapid interdependent ion migrations across the membrane. These ion migrations lead to a temporary reversal of the electric field across the membrane before its eventual return to the resting state. This complex, but transient, electrochemical event is the action potential. What follows is a cursory description of the basic biophysical mechanisms underlying the cardiac action potential. In reality, there are a myriad of nuanced electrochemical interactions involved in its generation, but the details of these interactions are beyond the scope of this research.

### 1.1.2 Nernst Potential

In order to understand the electrochemical processes that generate an action potential, one must understand the forces acting on ions in solution. The following discussion of the relevant physical laws and their mathematical formulations is adapted from the textbook, *Ion Channels of Excitable Membranes*, by Bertil Hille[6].

Movement of ions in solution occurs due to two fundamental mechanisms - diffusion and electrophoresis. Diffusion is the movement of a solute

from regions of relatively high concentration toward regions of relatively low concentration due to the random thermal motion of particles. Particles diffuse according to Fick's First Law of Diffusion:

$$J_D = -D_S \frac{\partial [S]}{\partial x} \quad (1.1)$$

where  $J_D$  is the molar flux due to diffusion,  $D_S$  is the diffusion coefficient associated with ion species  $S$ , and  $[S]$  is the concentration of the ion  $S$ . In this case, we call  $\frac{\partial [S]}{\partial x}$  the concentration (or chemical) gradient for ion  $S$ . The Nernst-Einstein relationship provides us with

$$D_S = \frac{\mu_S RT}{F} \quad (1.2)$$

where  $R$  is the ideal gas constant,  $T$  is the temperature of the solution in degrees Kelvin,  $\mu_S$  is the mobility of the ion species  $S$ , and  $F$  is Faraday's constant.

So we may write

$$J_D = -\frac{\mu_S RT}{F} \cdot \frac{\partial [S]}{\partial x} \quad (1.3)$$

Electrophoresis refers to the movement of charged particles due to the force applied by an electric field. Charged particles moving due to electrophoresis are governed by the equation

$$J_E = -\mu_S z_S [S] \frac{\partial v}{\partial x} \quad (1.4)$$

where  $J_E$  is the molar flux due to electrophoresis,  $z_S$  is the valence of the ion  $S$ , and  $v$  is electric potential. We call  $\frac{\partial v}{\partial x}$  the electrical gradient in this case. The total molar flux,  $J_T$ , is given by the sum of these two fluxes in what is known

as the Nernst-Planck molar flux equation:

$$J_T = -\mu_S \left( \frac{RT}{F} \cdot \frac{\partial [S]}{\partial x} + z_S [S] \frac{\partial v}{\partial x} \right) \quad (1.5)$$

The Nernst potential for ion  $S$  is defined to be the membrane potential that results in zero net flux of that ion across the membrane. In order to determine this value for a given ion, we set the total flux equal to zero and solve the resulting equation for  $\Delta v$  as follows.

$$J_{tot} = 0 \Rightarrow \frac{\partial v}{\partial x} = -\frac{kT}{z_S q} \cdot \frac{1}{[S]} \cdot \frac{\partial [S]}{\partial x} \quad (1.6)$$

which by the chain rule is equivalent to

$$\frac{\partial v}{\partial x} = -\frac{RT}{z_S F} \cdot \frac{\partial \ln [S]}{\partial x} \quad (1.7)$$

Then integrating both sides across the membrane yields

$$\int_{x_o}^{x_i} \frac{\partial v}{\partial x} dx = -\frac{RT}{z_S F} \int_{x_o}^{x_i} \frac{\partial \ln [S]}{\partial x} dx \quad (1.8)$$

where  $o$  denotes the outside of the cell and  $i$  denotes the inside. Note that we may choose any position  $x_o$  in the extracellular environment and any position  $x_i$  in the intracellular environment, since we assume that the only voltage drop occurs across the membrane and no concentration gradient exists within each compartment. Thus, the result of integration is

$$v_i - v_o = -\frac{RT}{z_S F} (\ln [S]_i - \ln [S]_o) \quad (1.9)$$

where  $v_o = v(x_o)$ ,  $v_i = v(x_i)$ ,  $[S]_o = [S](x_o)$ , and  $[S]_i = [S](x_i)$ . We call  $\Delta v = v_i - v_o$  the Nernst potential for the ion  $S$  and denote it  $E_S$ . So more concisely the

formulation of the Nernst potential is

$$E_S = \frac{RT}{z_S F} \ln \frac{[S]_o}{[S]_i} \quad (1.10)$$

The difference between the membrane potential and the Nernst potential for the ion  $S$  is the composite electrochemical gradient acting on that ion and is called the driving force associated with ion species  $S$ . The Nernst potential will be important later in the mathematical formulation of transmembrane ionic currents.

### 1.1.3 Cardiac Action Potential

The cardiac action potential depends upon numerous electric currents carried by a variety of ion species. The most prominent of these currents are those carried by sodium, calcium, and potassium ions through their respective ion channels. Other currents play a less substantial role in the generation of the action potential and so will be neglected in this description of cardiac action potential.

Many ion channels in excitable membranes are deemed voltage-gated because changes in voltage across the membrane lead to changes in their conformation. At any given moment a voltage-gated ion channel can be in one of three states - closed, open, or inactive. Channels in their closed state can be opened by an appropriate change in the membrane potential from its resting membrane voltage. Channels in their open state allow for conductance of a particular permeable ion species. Channels in their inactive state have en-

tered a transient non-conducting refractory period at depolarized potentials in which no changes in membrane potential can re-open them. After this refractory period, inactive channels can return to their closed state at hyperpolarized potentials[7]. It must be emphasized, though, that these voltage- and time-dependent alterations in channel conformation are stochastic processes. A change in the membrane voltage and the time since the voltage change merely results in a change in the probability that a given ion channel is in a certain state. Due to the high number of channels embedded in the membrane of each cell, we may average over the collection of all ion channels and consider the membrane's overall conductance to each ion as deterministic continuous functions of membrane voltage and time.

At the resting membrane potential of approximately  $-80$  mV, sodium channels, calcium channels, and to a lesser extent, potassium channels assume conformations which generally prohibit ions from passing through them, so the membrane is virtually impermeable to sodium and calcium and only slightly permeable to potassium. Additionally, there exists a relatively high concentration of sodium and calcium and a relatively low concentration of potassium in the extracellular environment with respect to the intracellular environment. Because of the membrane's higher permeability to potassium, the resting membrane potential stabilizes near the voltage required to exactly oppose the potassium concentration gradient, the potassium Nernst potential.

Upon the arrival of a brief, sufficiently strong depolarizing stimulus,

voltage-gated sodium channels embedded in the resting membrane begin to open allowing for the rapid flux of sodium ions into the cell down its electrochemical gradient. This influx of positively charged sodium ions further depolarizes the membrane resulting in the opening of more sodium ion channels and progressively increasing sodium influx. Sodium ion channels then rapidly begin entering their inactive state in which no amount of stimulus will re-open them and sodium current quickly decays to zero. Meanwhile, the calcium and potassium channels, which exhibit slower kinetics than sodium channels, also open in response to the depolarization. The resulting influx of positive calcium ions is opposed by an efflux of positive potassium ions leading to a period of little change to the membrane potential called the plateau of the action potential. Eventually, calcium ion channels begin to inactivate and potassium efflux through potassium channels repolarizes the membrane back toward the resting membrane potential. Ion pumps and exchangers within the membrane then return the extracellular and intracellular ion concentrations to their original states so that the cell is ready to be excited by a subsequent depolarizing stimulus[8]. Figure 1.2 provides a simple graphical representation of the previous description.

#### 1.1.4 Excitation-Contraction Coupling

In cardiac cells, the action potential serves as the impetus for contraction. The influx of calcium ions that occurs during the plateau phase of the

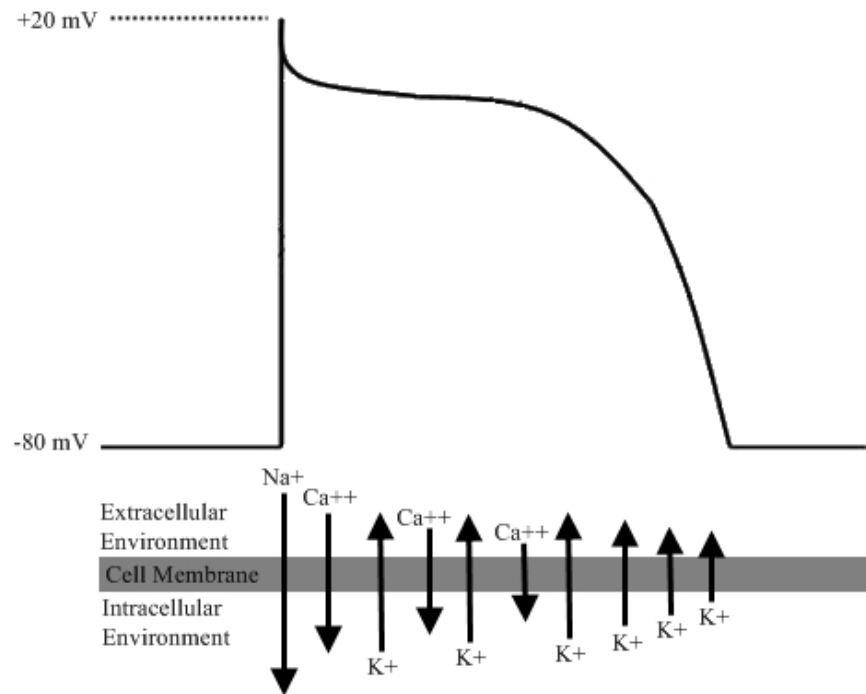


Figure 1.2: Typical human cardiac action potential morphology exhibiting the rapid upstroke phase carried primarily by a strong inward sodium current, a long plateau phase resulting from opposing calcium influx and potassium efflux, and a repolarization phase carried primarily by an outward potassium current which drives the action potential back down toward its resting state. The relative lengths of the arrows represents the strength of the current.

action potential initiates a process called calcium-induced calcium release in which calcium ions entering the cell bind with specialized calcium channels called ryanodine receptors in the membrane of the sarcoplasmic reticulum, an intracellular calcium-storing organelle. Upon opening of these calcium-activated channels, calcium exits the sarcoplasmic reticulum in large quantities and raises the intracellular calcium concentration substantially. The excess free calcium ions in the cytosol rapidly bind to a protein called troponin C. This calcium-troponin pair interacts with tropomyosin which, along with actin, forms an activated thin filament. Adjacent to and parallel to the thin filaments are so called thick filaments composed primarily of the protein myosin. Upon the calcium-troponin-tropomyosin interaction, myosin binding sites on the actin are vacated so that the myosin heads that run the length of the thick filaments can bind to the thin filament. A ratcheting action ensues and filaments are pulled in opposite directions resulting in contraction of the cell. This process by which the excitatory wave induces contraction of the cardiac cell is called excitation-contraction coupling[9]. Excitation-contraction coupling terminates as calcium is re-sequestered by the sarcoplasmic reticulum and expelled from the cell via ATP-dependent calcium pumps. In addition, calcium is forced across the plasma membrane into the extracellular space by the sodium-calcium exchange protein which uses the sodium ion gradient as the driving force.

The coordinated coupling of excitation and contraction throughout the

heart results in the contraction of the ventricles which eject blood into the pulmonary and systemic circulations. The human heart undergoes a two-phase heartbeat approximately once each second. The first phase is the contraction of the atria which forces blood from the two chambers of the atria into the two larger chambers called the ventricles. The second phase is the contraction of the ventricles which pumps blood from the right ventricle to the lungs for oxygenation and oxygen-rich blood from the left ventricle to every cell in the body. The excitatory wave originates in a region of the right atrium called the sinoatrial node (primary oscillator) and propagates from one cell to its neighbors through gap junctions linking adjacent cells. Depolarizing influxes of sodium in one cell are rapidly transmitted to adjacent cells through these gap junctions leading to their depolarization. In this manner, the electrical impulse propagates rapidly throughout the tissue and results in a coordinated contraction of the heart[10].

## **1.2 Mathematical Modeling of Electrophysiology**

### **1.2.1 Membrane-Transporter Pairing as an RC Circuit**

Just as the plasma membrane has an electrical analogue, the capacitor, so too do ion channels. Ion channels constitute variable resistors in parallel with this plasma membrane capacitor. From an electrodynamic standpoint then the plasma membrane and the ion channels, along with the electrochemical gradients associated with each ion, behave together like the RC circuit

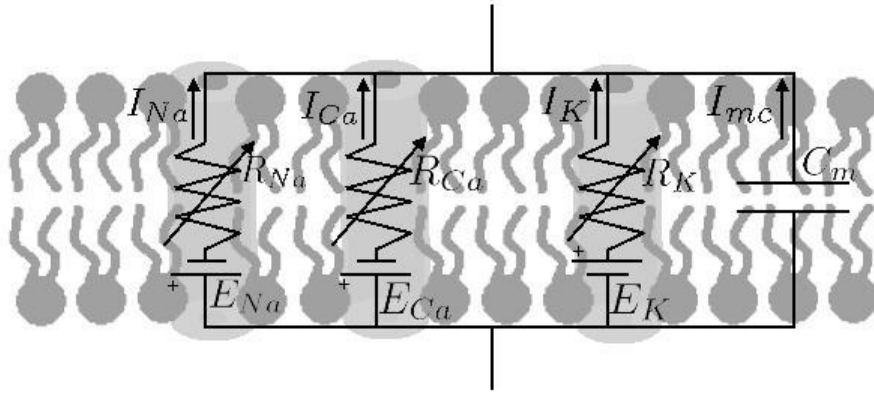


Figure 1.3: Equivalent circuit diagram in which the cell membrane can be thought of as a plate capacitor in parallel with ion channels which act as variable resistors. Note that the driving force on each ion has an electrical and chemical component, collectively referred to as its associated electrochemical gradient.

shown in Figure 1.3.

Applying Kirchoff's current law to this circuit we may conclude that

$$I_{Na} + I_{Ca} + I_K + I_{C_m} = 0 \quad (1.11)$$

Note that the physics of ideal capacitors dictates that  $C_m V_m = Q_m$  where  $C_m$  is the capacitance of the membrane (assumed constant),  $V_m$  is the membrane potential, and  $Q_m$  is the accumulated charge on the membrane. Differentiating both sides of this equation with respect to time, yields

$$C_m \frac{dV_m}{dt} = \frac{dQ_m}{dt} \quad (1.12)$$

and since  $I_{C_m} = \frac{dQ_m}{dt}$ , we can rewrite 1.11 as

$$\frac{dV_m}{dt} = - \left( \frac{1}{C_m} \right) (I_{Na} + I_{Ca} + I_K) \quad (1.13)$$

or more generally as

$$\frac{dV_m}{dt} = - \left( \frac{1}{C_m} \right) \left( \sum_{S \in \Omega} I_S \right) \quad (1.14)$$

where the sum is taken over the set,  $\Omega$ , of all ion species involved in the transmembrane currents via ion channels, ion exchangers, and ion pumps. Each of these currents exhibits a dependence on membrane voltage, ion concentrations, time, or a combination of all three factors. It was the seminal work of A.L. Hodgkin and A.F. Huxley who investigated these various dependencies as they pertained to action potentials in the giant nerve axon of squid that laid the foundations of modern electrophysiological modeling. At the heart of their model is equation 1.14 which serves as the basis for virtually every model that has followed.

### 1.2.2 The Hodgkin-Huxley Formalism

The original Hodgkin-Huxley neuronal model[11] included the contributions of the membrane capacitance current, the transient sodium current responsible for the action potential upstroke, the potassium current responsible for repolarization of the axon, and a non-specific leak current. With the addition of an inward calcium current, this model has been adapted to simulate cardiac action potentials. Since 1952, the Hodgkin-Huxley model has spawned countless models, most notably the DiFrancesco–Noble sinoatrial model[12],

the McAllister–Noble–Tsien Purkinje fiber model[13], the Beeler–Reuter ventricular model[14] and the many incarnations of the original 1991 Luo-Rudy ventricular model[15]. The last fifty years have seen a tremendous increase in model complexity. Modern models now account for the multitude of currents known to be involved in cardiac dynamics and include sophisticated channel kinetics based on evolving experimental discoveries, but most are still formulated with what has become known as the Hodgkin-Huxley formalism.

The genius of Hodgkin and Huxley’s work stems from their innovative use of the voltage clamp. The voltage clamp devised by Kenneth Cole, in conjunction with George Marmont, is a device that provides an excitable cell with current in such a way as to exactly oppose any changes in voltage. The utility of such a device is that one may “clamp” the membrane voltage at a specific value, and then by monitoring the currents needed to maintain that voltage, one immediately knows how much transmembrane current is passing through ion channels at each moment in time. By selectively blocking certain types of ion channels, Hodgkin and Huxley were able to plot time courses of specific ionic currents for various fixed voltages.

To understand how these experiments led to the development of their ingenious model, we must first consider Ohm’s law,  $V = IR$ , as applied to a simple electrical circuit. In such a circuit, the voltage drop depends only upon the resistance in the circuit and the current through that circuit. In the circuit illustrated in Figure 1.3 defined by the membrane capacitance and the cur-

rent flow across that membrane through ion channels, the voltage drop is due to concentration differences as well as a the transmembrane electric current carried by ions. So the movement of an ion species  $S$  across the membrane results in a voltage drop equal to the sum of these two contributions (i.e. we get  $V = I_S R_S + E_S$  where  $I_S$  is the current carried by the ion species  $S$ ,  $R$  is the bulk resistance of the membrane to the passage of that ion species, and  $E_S$  is the Nernst potential associated with that ion species). Solving for  $I_S$  yields the current-voltage relationship

$$I_S = g_S (V_m - E_S) \quad (1.15)$$

where, by convention the conductance for ion species  $S$ ,  $g_S$ , replaces  $\frac{1}{R_S}$ . [16]

This formulation should seem natural in the context of the earlier discussion of Nernst potential. Recall that the Nernst potential for a given ion species is the membrane voltage at which the electrical and concentration gradients for that ion species would be equal and opposing (i.e. the voltage at which there is no net electrochemical force felt by that ion species). Consequently,  $(V_m - E_S)$ , provides the net electrochemical driving force exerted on that ion species. When  $V_m = E_S$ , current associated with that ion species is extinguished. The current-voltage relationship states that the transmembrane current carried by a particular ion species depends upon the force that ion species feels and the membrane conductance associated with that ion species.

Hodgkin and Huxley's experiments related to sodium and potassium currents across a nerve cell's membrane showed that  $g_{Na}$  and  $g_K$  exhibited a highly

nonlinear dependence upon membrane voltage and time. Their voltage clamp experiments showed that a sufficiently strong step towards less negative membrane potentials (depolarizing step) would activate a transient sodium current that peaked quickly and subsequently decayed in a slightly slower manner back to zero current. They recognized that since the only change in driving force associated with sodium occurred at the time of the voltage step, the changes in current were due to changes in  $g_{Na}$ . Hodgkin and Huxley went on to fully characterize the time- and voltage-dependencies of  $g_{Na}$  by expressing it as the product of a maximum possible sodium current,  $\overline{g_{Na}}$ , and several gating variables, each governed by their own differential equation. The formulation for the sodium current under this so called Hodgkin-Huxley formalism is then

$$I_{Na} = \overline{g_{Na}} m^3 h (V_m - E_{Na}) \quad (1.16)$$

$$\frac{dm}{dt} = \frac{m_\infty(V_m) - m}{\tau_m(V_m)} \quad (1.17)$$

$$\frac{dh}{dt} = \frac{h_\infty(V_m) - h}{\tau_h(V_m)} \quad (1.18)$$

where  $m_\infty \in [0, 1]$ ,  $h_\infty \in [0, 1]$ ,  $\tau_m$ , and  $\tau_h$  are themselves nonlinear functions of membrane voltage.

Similar experiments confirmed the time- and voltage-dependence of  $g_K$  yielding the corresponding formulation

$$I_K = \overline{g_K} n^4 (V_m - E_K) \quad (1.19)$$

where  $n$  satisfies a differential equation analogous to those satisfied by  $m$  and  $h$ .

The variables  $m$ ,  $h$ , and  $n$  have come to be known as gating variables since more recent imaging of ion channel proteins has shown that sodium and potassium channels each have four substructures which act as physical gates regulating the flow of ions through the channel pore. That the model was most accurately formulated with four gating variables in each term is a remarkable instance of mathematics predicting subsequent scientific discovery. In general, the fundamental structure of the model is as follows:

$$\frac{dv}{dt} = - \left( \frac{1}{C_m} \right) \sum I_S \quad (1.20)$$

where the sum is taken over all of the transmembrane currents each given by a term of the form

$$I_S = \bar{g}_S z_1^{k_1} z_2^{k_2} \cdots z_p^{k_p} (V_m - E_S) \quad (1.21)$$

and where the gating variables  $z_i$  obey a differential equation of the form

$$\frac{dz_i}{dt} = \frac{z_{i\infty}(V_m) - z_i}{\tau_{z_i}(V_m)} \quad (1.22)$$

While models of cell excitability have become increasingly complex as scientific knowledge about the molecular structure and function of the plasma membrane increases, most still adhere to this basic Hodgkin-Huxley formalism.

### 1.2.3 The Pandit and Mitchell-Schaeffer Models

One such physiologically detailed model of cardiac action potential used in this research is a system of 26 nonlinear, coupled ordinary differential equa-

tions devised by Pandit et al[17]. This model accounts for ten different ionic currents in addition to changes in ion concentrations and the effects of calcium buffering. The Pandit model was originally developed to model the rat cardiac action potential and since we base this research on experimental data gleaned from rat studies, the Pandit model provides an ideal computational setting in which to investigate the effects of caveolar sodium current on rat cardiac action potential. In this research, the Pandit model is used to provide baseline simulation data to which we compare simulations which account for caveolar sodium current.

The physiological accuracy of this, and other complex models of cardiac action potential, comes at a cost, though. While a high degree of complexity may yield extremely realistic results, it prevents a thorough mathematical analysis of the system and obscures dependencies between variables and parameter values. Therefore, in this research, we also seek to develop a model of rat cardiac action potential which retains the essential dynamics of the Pandit model and generates similar results upon incorporation of caveolar sodium current, but is simple enough to allow a detailed analysis.

The Mitchell-Schaeffer two-current mode[18] is one such simplified model of cardiac action potential, consisting of only two differential equations, but nonetheless providing accurate simulations of cardiac action potential. In their 2003 paper, Mitchell and Schaeffer demonstrate that dynamic restitution experiments exhibit the same transition from one-to-one pacing to alternans as

seen in experimental trials. This model also accurately predicts the experimentally observed hysteresis in the bifurcation diagram when the pacing protocol is reversed. In addition the low dimensionality in the Mitchell-Schaeffer model means that specific relationships between parameter values and overall dynamics can be extracted directly from analysis of the system without reliance on numerical approximations.

For this reason, we have chosen to investigate the effects of caveolar sodium current in a simplified model of rat cardiac action potential that we base largely on the Mitchell-Schaeffer model. Our modified Mitchell-Schaeffer model is similar to the original model in many respects, but accounts for three ionic currents and is composed of three differential equations instead of two. This three-variable model permits us to more thoroughly examine, from a mathematical perspective, the role of caveolar sodium current in shaping overall cardiac electrodynamics.

### **1.3 Caveolae and the $\beta$ -Adrenergic Response**

#### **1.3.1 Caveolae Structure**

Caveolae, Latin for “little caves,” are small, invaginations of the plasma membrane protruding into the cytosol of several varieties of cells including cardiac myocytes. Many have a nearly spherical shape with a diameter of 40-100 nm, though they may also occur in clusters resembling a bunch of grapes (rosettes)[19]. In comparison, a typical cardiac myocyte is somewhat cylin-

dricial in shape with a diameter of approximately 10-20  $\mu\text{m}$  and a length of approximately 100  $\mu\text{m}$ . Figure 1.4 shows an electron micrograph of a rat cardiac myocyte cross section with caveolae distributed densely around the subsarcolemma.

Caveolae typically maintain a conformation in which the caveolar neck is tightly closed, establishing an intracaveolar environment distinct from both the intracellular and extracellular environments. Recent investigations of caveolar function suggest that in addition to being a prominent structural feature on the cardiac subsarcolemma, caveolae also play a significant role in modulating sodium current. These investigations reveal that not only do caveolae contain  $\text{Na}_v1.5$  channels (the sodium channels responsible for the current driving the action potential upstroke), but perfusion of the cardiac cell with the  $\beta$ -adrenergic agonist ( $\beta$ -agonist), isoproterenol, causes the caveolar necks to open thereby creating an electrically continuous path between functional caveolar sodium channels and the extracellular environment[1, 20, 21]. Caveolae are therefore reservoirs of 'recruitable' ion channels, and as such, caveolar sodium current constitutes a substantial and previously unrecognized inward current that can significantly influence action potential morphology and conduction velocity.

A model of cardiac action potential that accounts for these caveolar spaces and the additional currents that result from the opening of caveolae would provide researchers with the means to more accurately predict a cardiac cell's  $\beta_1$ -

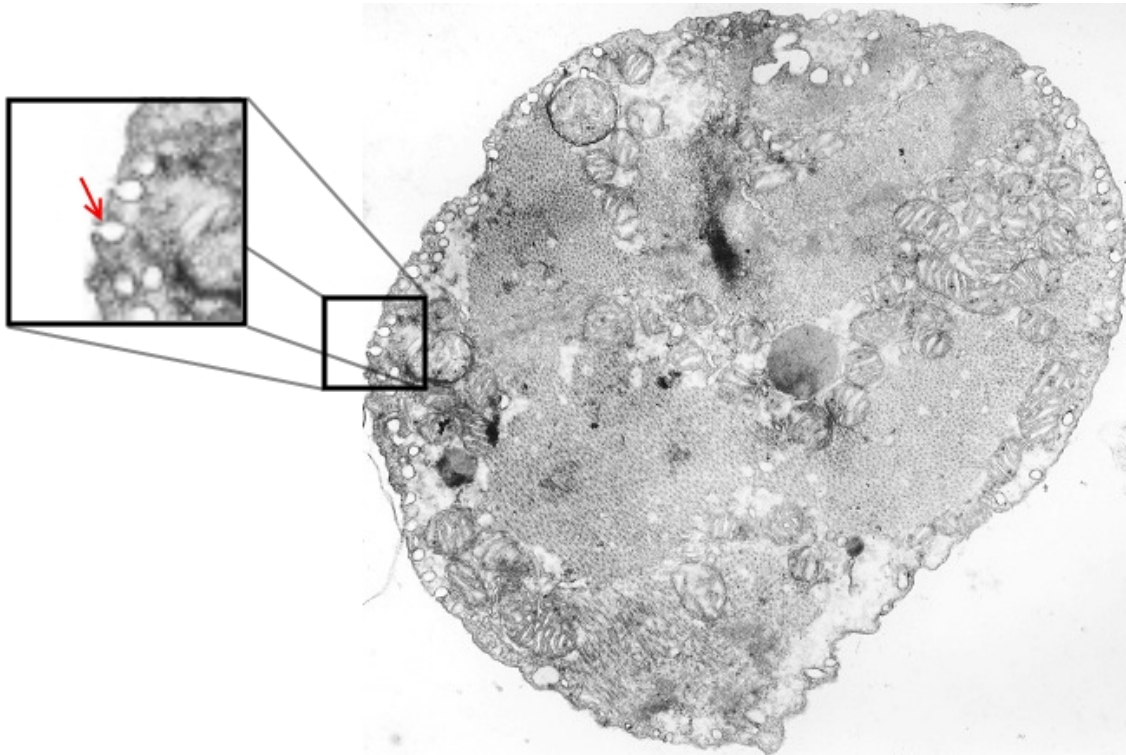


Figure 1.4: Electron micrograph of an adult rat ventricular cell showing caveolae (arrow in inset) around the perimeter. Caveolae are typically spherical in shape with a diameter of 40 - 100 nm and can accumulate in a clustered structure resembling a bunch of grapes (rosettes). Under normal conditions, the necks of these caveolae are pinched tightly closed preventing any interaction between the extracellular and intracaveolar environments. Thus, any ion channels embedded in the caveolar membrane are isolated from electrical events occurring on the sarcolemma.  $\beta$ -adrenergic stimulation causes these necks to open presenting caveolar membrane proteins to the sarcolemma. (Image courtesy of Erwin Shibata, Molecular Physiology and Biophysics, University of Iowa).

adrenergic response.  $\beta_1$ -agonists are sympathomimetic drugs that mimic the de novo neurotransmitter, norepinephrine, and the hormone, epinephrine. These drugs are used extensively in enhancing contractility, but have been shown to increase the risk of cardiovascular dysfunction especially in patients with an existing cardiac condition[22]. A more complete understanding of the effects of  $\beta_1$ -agonists on cardiac myocytes is paramount to developing new treatments that do not compromise heart health.

### 1.3.2 Caveolae Function

To fully appreciate the novelty of this caveolae-associated  $\beta_1$ -adrenergic mechanism, one must understand the nuances of the cardiac neurohumoral response. Neurohumoral modulation of cardiac electrophysiology refers to the modulation of ionic currents across the sarcolemma by sympathetic and parasympathetic signaling. Physiological characteristics such as the heart rate, contraction strength, and conduction velocity of the excitatory wave can be altered by the actions of the sympathetic and parasympathetic nervous systems. Chemicals, called neurohumors, secreted by these nerves bind to receptors on the cell membrane which in turn initiate cellular signaling cascades within the cells. Ultimately, these signaling cascades affect the kinetics of the cell's ion transporters thereby changing its electrical properties.

### 1.3.2.1 PKA-Dependent $\beta_1$ -Adrenergic Signaling Pathway

Parasympathetic nerves secrete acetylcholine and act primarily on the supraventricular tissues where their innervation is much more extensive than in the ventricles. Acetylcholine's main effect is to slow phase 4 depolarization in the sinoatrial node resulting in a slower overall heart rate. In contrast, the sympathetic nervous system employs the neurohumors epinephrine and norepinephrine to cause increases in heart rate, contraction strength, and conduction velocity. It is the sympathetic response that is most relevant to this research since norepinephrine and epinephrine are both  $\beta_1$ -agonists.

There are two main types of  $\beta$ -receptors in cardiac cells,  $\beta_1$ - and  $\beta_2$ -receptors, but the details of their functional differences are beyond the scope of this research. What is important is the signaling cascade, called the receptor-effector coupling, that occurs when a cardiac myocyte is treated with a  $\beta$ -agonist. To isolate the  $\beta$ -adrenergic effects, the chemical isoproterenol is used in place of norepinephrine or epinephrine since both of these also bind to so-called  $\alpha$ -receptors, while isoproterenol is purely a  $\beta$ -agonist. When isoproterenol binds to a  $\beta$ -receptor which itself is bound on the subsarcolemma to a stimulatory G-protein, the receptor undergoes a conformational change. This conformational change drastically decreases its G-protein's affinity for GDP and increases its affinity for GTP. The binding of GTP to the stimulatory G-protein causes the disassociation of its  $\alpha$ -subunit from its  $\beta\gamma$ -subunit. The stimulatory G-alpha ( $G_s\alpha$ ) subunit is then free to activate adenylyl cyclase which

converts ATP to cyclic AMP (cAMP). The cAMP then binds to the regulatory subunit of protein kinase-A (PKA) resulting in the release of the PKA's catalytic subunit which increases the phosphorylation at various target sites.[19, 23]

The target sites that are most affected are the sodium-potassium pump and the ion channels responsible for the delayed rectifier potassium current,  $I_{Ks}$ , the L-type calcium current,  $I_{CaL}$ , and the inward sodium current,  $I_{Na}$ . In the sinoatrial node,  $\beta$ -adrenergic stimulation also causes a shift in the the hyperpolarization-activated “funny” current activation curve toward higher voltages, resulting in more rapid phase 4 depolarization and an increase in heart rate[19, 23]. In each of these cases, the interaction of PKA's catalytic subunit with an ion transporter changes that transporter's kinetics.

### 1.3.2.2 PKA-Independent $\beta_1$ -Adrenergic Signaling Pathway

While this PKA-dependent receptor-effector coupling pathway has been thoroughly studied, we focus on a new mechanism for modulating ionic currents in cardiac myocytes that is caused by a direct interaction between the  $G_s\alpha$ -subunit and caveolin-3, the primary scaffolding protein for cardiac caveolae. A study has shown that this direct mechanism is in fact a distinct means for  $\beta$ -adrenergic stimulation to affect whole cell sodium current without changing single channel dynamics. It was demonstrated that in the presence of PKA inhibitor, which eliminates sodium current increases due to phosphorylation, perfusion of the cardiac myocyte membrane with isoproterenol still resulted

in a 30% increase in whole cell sodium current in rat ventricular myocytes[1]. This direct mechanism of sodium current increase has never been accounted for in mathematical models of cardiac action potential and forms the primary focus of this research.

In 2002, researchers demonstrated the presence of  $\text{Na}_v1.5$  sodium channels within rat cardiac caveolae[20] and in 2006 the same research group produced data supporting the hypothesis that the direct pathway of sodium current enhancement was the result of conformational changes in the caveolae themselves[21]. The key experiment proceeded as follows: After elimination of the indirect mechanism by application of a PKA inhibitor, myocytes were bathed in QX-314, a long-lasting, membrane-impermeant sodium channel blocker. This resulted in complete abolition of the  $\text{Na}_v1.5$  sodium current. However, upon subsequent  $\beta$ -adrenergic stimulation, sodium current was recovered to approximately 25% of control. The hypothesis supported by these findings, and the hypothesis underpinning this research, is that  $\beta$ -adrenergic stimulation initiates a mechanism by which caveolar necks open, resulting in the recruitment of otherwise sequestered sodium channels, and that this physical addition of ion channels, rather than changes in single channel kinetics, causes the observed increase to sodium influx. The schematic in Figure 1.5 illustrates the differences between this direct mechanism of sodium current modulation and the indirect PKA-dependent mechanisms.

Increases in this sodium current, which is responsible for the rapid de-

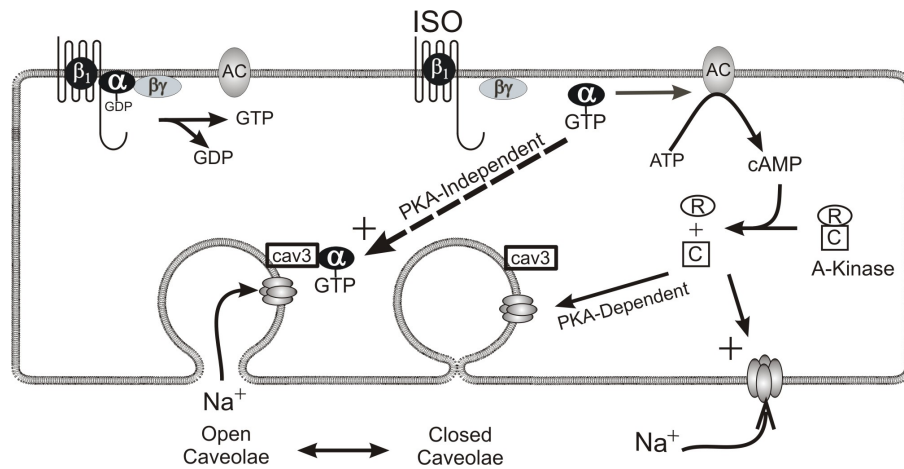


Figure 1.5: Two pathways of  $\beta$ -adrenergic modulation of cardiac sodium current. (Image courtesy of Erwin Shibata, Molecular Physiology and Biophysics, University of Iowa).

polarization of the plasma membrane, are known to increase the rate at which this depolarization occurs. The quantity most often used as a measure of this rate is the maximum upstroke velocity - the maximum rate of membrane voltage change attained during the initial upstroke phase of the action potential. Experiments have shown that there exists a nearly linear relationship between peak inward ionic current during the upstroke and the maximum upstroke velocity of the action potential[24, 25]. In addition, it has been shown that the conduction velocity of the excitatory wave through cardiac tissue is directly proportional to the square root of the maximum upstroke velocity[26, 27].

Much is yet unknown about the manner in which caveolae open and about the molecular constituents of the caveolar membrane. It has been shown

that a single  $G_s\alpha$  amino acid (41histidine) is responsible for the interaction between the  $G_s\alpha$ -subunit and caveolin-3[2], but how this interaction causes opening of the caveolar neck and what sort of opening characteristics result remain unknown. Also, since no long-lasting, membrane-impermeant calcium or potassium channel blocker analogous to the sodium channel blocker QX-314 exists, the full profile of caveolar ion channels remains unclear. Perhaps each caveolae contains a mosaic of ion transporters or perhaps there are different varieties of caveolae with distinct combinations of ion channels, pumps, and exchangers. Since it is only known with certainty that treatment with a  $\beta$ -agonist increases sodium current, we focus on the incorporation of a caveolar sodium current in this research.

#### **1.4 Specific Objective**

The primary objective of this research is to develop mathematical models of cardiac action potential that lend insight into the role that caveolar sodium currents play in determining action potential morphology and in contributing to arrhythmogenesis.

This research is comprised of three distinct parts: The first is the development of a physiologically detailed three-compartment model of rat cardiac action potential that incorporates caveolar sodium current. This model allows us to test how caveolar sodium currents may affect action potential morphology and how the intracaveolar environment evolves when the caveolae are closed.

The second is the development of a simplified mathematical model that incorporates the results gleaned from the first, but which is simple enough to allow for a more thorough mathematical analysis. From this model I extract relationships between physiologically relevant quantities and the parameter value associated with the number of open caveolae. The third part is the development of a model of stochastic caveolar opening that is used to investigate possible pathological caveolar mechanisms and their arrhythmogenic potential. We use this model to offer a hypothesis related to the cause of cardiac arrhythmias that are characterized by delayed repolarization of the cells.

## CHAPTER 2 CAVEOLAE-INCLUSIVE MODEL

### 2.1 Introduction to the Caveolae-Inclusive Model

Classic single-cell models of cardiac action potential assume that the sarcolemma provides a static boundary between two compartments, the cytosol and the extracellular environment. In such models, ionic interactions between these two compartments are governed by the voltage- and time-dependent kinetics of the ion channels, pumps, and exchangers embedded in this static membrane. As mentioned in the introduction, however, new findings related to cardiac caveolae and their  $\beta$ -adrenergic response suggest that the sarcolemma itself can exhibit current modulating kinetics[1, 20, 21, 2]. A model that accounts for the additional currents resulting from the opening of caveolae could provide insight into their effects on action potential morphology and a more accurate simulations of their overall cardiac  $\beta$ -adrenergic response.

I seek here to provide such a model. Additionally, much is still unknown about the physical attributes of cardiac caveolae - their density on the subsarcolemma, their molecular constituents, and their opening dynamics - so I use computational means to explore these open questions. In this chapter, I derive an estimate of caveolae density and use this estimate to develop a caveolae-inclusive model of cardiac action potential. The model is based on an existing model, but incorporates a variable caveolar sodium current that simulates the

effects of PKA-independent  $\beta$ -adrenergic modulation of sodium current. With this model, I can replicate the same caveolar sodium currents seen experimentally and simulate their expected effects on action potential morphology. The results are consistent with other studies of sodium current modulation which indicate a positive, nearly linear relationship between sodium current and action potential maximum upstroke velocity[24, 26, 27].

## 2.2 Cardiac Caveolar Density

I am interested in quantifying the density of caveolae on the sarcolemma of a typical ventricular cardiac cell so the number of caveolae contained in a model cell can be estimated. I achieve this by noting first that the whole-cell maximum sodium conductance,  $\overline{g_{Na}}$ , divided by the sodium single-channel conductance,  $\gamma_{Na}$ , yields the number of sodium channels on the sarcolemma. Thus, in the absence of changes to single-channel kinetics, the quotient of any increase in whole-cell sodium conductance,  $\Delta\overline{g_{Na}}$ , and  $\gamma_{Na}$  (i.e.  $\frac{\Delta\overline{g_{Na}}}{\gamma_{Na}}$ ) provides a good estimate for the number of additional sodium channels present on the sarcolemma. However, there is undoubtedly variation in caveolar density across cell types, and perhaps transmurally within the same cell type, so these estimates are rough and additional experimental work is necessary to establish more accurate estimates. It should be noted that whole-cell conductance is often reported as conductance per unit cell capacitance so that results are normalized across different cell sizes. I use this same convention in

the calculations that follow.

Assuming  $S_{cav}$  sodium channels per caveolae,  $\frac{\Delta \overline{g_{Na}}}{\gamma_{Na} \cdot S_{cav}}$  is the number of caveolae which have opened and presented their sodium channel to the sarcolemma and thus provides a lower bound on the number of caveolae contained in that cell. If these conductances are given, as they often are, in units of conductance per unit cell capacitance,  $C_m$ , then this lower bound on the number of caveolae in the cell is given by  $\frac{\Delta \overline{g_{Na}}}{\gamma_{Na} \cdot S_{cav}} C_m$ .

Of course this method requires accurate measurements of  $\overline{g_{Na}}$ ,  $\gamma_{Na}$ , and  $C_m$ . While no measurements of  $\overline{g_{Na}}$  were reported in the papers related to caveolar sodium current, we can infer  $\overline{g_{Na}}$  from an examination of the sodium current-voltage (I-V) curves that are reported.

Sodium I-V curves are one of several standard approaches employed by electrophysiologists to help characterize the sodium currents that result from changes in membrane potential. The general procedure for producing a sodium I-V curve is as follows: First, the cell membrane is held (a.k.a. conditioned) at a fixed voltage at (or hyperpolarized relative to) the resting membrane potential using a voltage-clamp until the cell membrane has reached equilibrium. The membrane potential is then instantaneously stepped up to a new sustained voltage (a.k.a. test potential) at which activation of sodium channels occurs and the time course of the sodium current is recorded. This process is repeated over a wide range of depolarizing test potentials and the peak sodium current attained in each trial is plotted as a function of the test potential. I-

V curves provide a graphical representation of important quantities such as the membrane potential at which activation of sodium begins, the potential at which maximum sodium current is elicited, and the sodium Nernst potential (a.k.a. reversal potential). We are interested in identifying changes in whole-cell sodium conductance from inspection of sodium I-V curves.

Note that sodium I-V curves are well fit by functions of the form:

$$I_{Na,peak} = \frac{\overline{g_{Na}}(V_m - E_{Na})}{1 + e^{\frac{(V_{1/2} - V_m)}{k}}} \quad (2.1)$$

where  $V_{1/2}$  is the membrane potential at half-maximal sodium conductance and  $k$  is the slope factor. Since  $e^{\frac{(V_{1/2} - V_m)}{k}} \rightarrow 0$  rapidly as  $V_m$  increases beyond  $V_{1/2}$  (which is at approximately -25 mV in the cases we will consider), the ascending limb of the sodium I-V curve is well approximated by the linear function,

$$I_{Na,peak} = \overline{g_{Na}}(V_m - E_{Na}) \quad (2.2)$$

So, the slope of this nearly linear portion of a sodium I-V curve, provides an accurate estimate of the value of  $\overline{g_{Na}}$  in the experiment. Comparing increases in the slope of the ascending limbs from two I-V curves then provides an effective method for deriving  $\Delta\overline{g_{Na}}$ .

I apply this method to two relevant sets of I-V curves: Figure 6.A. from the 1999 paper by Lu et al[1] and Figure 2.B. from the 2008 paper by Palygin et al[2]. Both experiments test the extent to which the introduction of  $1 \mu M$  of  $G_s\alpha$  into the cytosol of rat cardiac myocytes modulates sodium current density via the direct PKA-independent signaling pathway. The experiments are con-

ducted at the same temperature ( $22^{\circ}C$ ) and since the currents are measured in terms of current density (with units  $pA/pF$ ), differences in cell size need not be considered. However, in the Lu et al study[1], the experiments were conducted with an extracellular sodium concentration of 20 mM, while in the Palygin et al study[2], they were conducted with an extracellular sodium concentration of 10 mM. This difference will become important in our estimations of  $\gamma_{Na}$  in each experiment.

The slope of the ascending limb of an I-V curve provides a good estimate of  $\overline{g_{Na}}$ . By superimposing well fitting lines on the ascending limbs of the I-V curves in figures from the Lu et al[1] and Palygin et al[2] papers, I derive estimates for  $\overline{g_{Na}}$  in each case. In the figure from Lu et al[1], it appears that the line associate with the control I-V plot intersects the axes at approximately (0,-150) and (24,0), while the line associated with the application of  $G_s\alpha$  intersects the axes at approximately (0,-210) and (27,0), yielding maximum sodium conductances of  $\frac{150}{24} = 6.25 \text{ pA/pF}\cdot\text{mV} = 6.25 \text{ nS/pF}$  and  $\frac{210}{27} = 7.7 \text{ pA/pF}\cdot\text{mV} = 7.7 \text{ nS/pF}$ , respectively, and a  $\Delta\overline{g_{Na}}$  of  $1.527 \text{ nS/pF}$ . This is a 24% increase in whole-cell sodium conductance (yielding a maximum peak  $I_{Na}$  increase of 45%).

In the figure from Palygin et al[2], it appears that the line associate with the control I-V plot intersects the axes at approximately (0,-39) and (23,0), while the line associated with the application of  $G_s\alpha$  intersects the axes at approximately (0,-51) and (21,0), yielding maximum sodium conductances of  $\frac{39}{23} \approx 1.7 \text{ pA/pF}\cdot\text{mV} = 1.7 \text{ nS/pF}$  and  $\frac{51}{21} \approx 2.43 \text{ pA/pF}\cdot\text{mV} = 2.43 \text{ nS/pF}$ , respectively,

and a  $\Delta\overline{g_{Na}}$  of  $\approx 0.73$  nS/pF. This is a 43% increase in whole-cell sodium conductance (yielding a maximum peak  $I_{Na}$  increase of 36%).

The substantial differences between the estimates that each experiment provides and the order of magnitude differences in the peak sodium current densities that are evident in these two I-V curves are possibly due to variations in the types of cells used in the related experiments. It is also possible that these differences are the result of problems controlling for cell size that may have affected the experimental results or from differences in the methods of activation used.

It is important to note that perfusion of a cardiac cell with 10  $\mu$ M of the  $\beta$ -agonist isoproterenol and injection of 1 nM of  $G_s\alpha$  result in markedly smaller increases in sodium current (a 20-30% increase in maximum peak  $I_{Na}$ ) than injection of 1  $\mu$ M  $G_s\alpha$  (a 35-45% increase in maximum peak  $I_{Na}$ ). Since the mechanism (caveolae opening to present the sarcolemma with additional sodium channels) is the same in all cases, this differential increase must be attributed to more caveolae opening at higher concentrations of intracellular  $G_s\alpha$  suggesting some saturation point at which all the caveolae must be opened. Thus, we only know that the number of caveolae in a cell is at least enough to produce the increase in sodium current associated with the injection of 1  $\mu$ M of  $G_s\alpha$ .

The sodium single-channel conductance,  $\gamma_{Na}$ , must also be determined in order to calculate the change in the number of sodium channels on the sar-

colemma. Before doing so, it is important to understand what single-channel conductance measures, and to contrast conductance with permeability because their difference is important and not immediately obvious. The permeability of a membrane to a certain ion measures the ease with which the membrane allows ions of that type to cross the membrane, while conductance to that particular ion measures the membrane's ability to carry current associated with that ion across the membrane. Consider a solution separated into two compartments by a membrane in which many open sodium channels reside, and suppose the solution contains a nearly negligible concentration of sodium ions. In such a case, the permeability of the membrane to sodium would be high, while its sodium conductance would be low since the probability of any sodium ion encountering a sodium channel and crossing the membrane is very low. Sodium single-channel conductance therefore is not only dependent upon the molecular structure of the channel, but also upon the concentration of sodium ions in the intracellular and extracellular environments[19].

For this reason, the ionic conditions under which the aforementioned experiments were performed must be considered when calculating  $\gamma_{Na}$ . Recall that in the first experiment, extracellular sodium concentration is 20 mM. If sodium reversal potential is assumed to be approximately 25 mV, as it appears to be in the figure from Lu et al[1] then the Nernst equation[6] suggests that intracellular sodium concentration is approximately 7.5 mM. A similar calculation using data from the second experiment gives an intracellular sodium

concentration of approximately 4.2 mM (This is in good agreement with the value of 5 mM reported for the second experiment).

A 2006 study of cardiac and neuronal sodium channel isoforms in rat cardiac myocytes[28] reports that single-channel conductance for  $\text{Na}_v1.5$  channels can be assumed to be 2.2 pS when extracellular and intracellular sodium concentrations are 20 mM and 10 mM, respectively, and the temperature is fixed at  $23^\circ\text{C}$ . Therefore, one should expect  $\gamma_{\text{Na}}$  to be at most 2.2 pS in both the Lu et al[1] and Palygin et al[2] experiments, and perhaps even lower in the Palygin et al[2] experiment due to the lower concentrations of sodium ions in this case.

Recall from the current-voltage curves we were able to extract changes in whole-cell sodium conductance of  $\Delta\bar{g}_{\text{Na}} \approx 1.527 \text{ nS/pF}$  and  $\Delta\bar{g}_{\text{Na}} \approx 0.73 \text{ nS/pF}$ , respectively. Since  $\gamma_{\text{Na}}$  is expected to be at most 2.2 pS in these experiments, the value  $\frac{1527.7 \text{ pS/pF}}{2.2 \text{ pS/channel}} \approx 694 \text{ channels/pF}$  and  $\frac{730 \text{ pS/pF}}{2.2 \text{ pS/channel}} \approx 332 \text{ channels/pF}$  then provide lower bounds on the amount by which the sarcolemmal sodium channel density increases as a result of caveolae opening in the first and second experiments, respectively. Thus, the estimates of caveolae density are  $\frac{694}{S_{\text{cav}}} \text{ caveolae/pF}$  and  $\frac{332}{S_{\text{cav}}} \text{ caveolae/pF}$ . Notice that even though the units for these quantities are  $\text{caveolae/pF}$ , they are referred to as caveolae *densities*. This because whole-cell capacitance provides one measure of cell surface area since capacitance per unit area is essentially fixed for the plasma membrane at about  $1 \text{ } \mu\text{F/cm}^2$ [5, 6]. For this reason cell size is often reported in terms of whole-cell capacitance. I will

use this fact in the next section where I formulate the mathematical model.

It is noteworthy to mention that the density of cardiac caveolae on the subsarcolemma can also be estimated by inspection of electron micrographs which illustrate the colocalization of voltage-gated sodium channels and caveolin-3. Since caveolin-3 is the primary structural protein for cardiac caveolae, clustering of the targets which are bound to caveolin-3 with targets which are bound to  $\text{Na}_v1.5$  channels likely indicates a sodium channel-containing caveolae. Calculating the density of caveolae in this manner suggests there are approximately  $5 \text{ caveolae}/\mu\text{m}^2$  which corresponds to  $500 \text{ caveolae}/pF$  assuming  $1 \mu F/cm^2$ [19]. Additionally, a study of plasmalemmal folds and caveolae in rabbit right ventricular papillary myocytes[29] reports a density of  $4 \text{ caveolae}/\mu\text{m}^2$  which corresponds to  $400 \text{ caveolae}/pF$ . Clearly, both of these values are in very good agreement with the previous two estimates suggesting that the use of sodium I-V curves to calculate caveolar density is accurate.

### 2.3 Formulation of the Caveolae-Inclusive Model

Since the data I seek to replicate comes from experimental work done on rat cardiac myocytes, I incorporate caveolar effects into an existing model of rat cardiac action potential. One of the few such models, devised by Pandit et al[17] in 2001, consists of a system of 26 nonlinear coupled differential equations. This highly detailed model uses the Hodgkin-Huxley formalism and accounts for ten types of transmembrane ionic currents: the inward sodium

current ( $I_{Na}$ ) responsible for the upstroke of the action potential, the L-type calcium current ( $I_{CaL}$ ), the calcium-independent transient outward potassium current ( $I_t$ ), the steady-state outward potassium current ( $I_{ss}$ ), inwardly rectifying potassium current ( $I_{K1}$ ), the hyperpolarization-activated (“funny”) current ( $I_f$ ), a linear background current ( $I_B$ ) carried by sodium, potassium, and calcium, and currents generated by the sodium-potassium pump ( $I_{NaK}$ ), the calcium pump ( $I_{CaP}$ ), and the sodium-calcium exchanger ( $I_{NaCa}$ ). In addition, it accounts for changes in ion concentration due to these currents, and in the case of calcium, it accounts for changes in ion concentration due to the regulatory effects of the sarcoplasmic reticulum and intracellular calcium-buffering. Since this model’s complexity prohibits a concise formulation, I have included it in Appendix A and limit the discussion of it here to a brief overview.

Of most relevance to the caveolae-inclusive model is the Pandit model formulation of the sodium current:

$$I_{Na} = \overline{g_{Na}} m^3 h j (V_m - E_{Na}) \quad (2.3)$$

Recall that the standard Hodgkin-Huxley formalism includes only two gating variables - the activation variable  $m$  and the inactivation variable  $h$ . The Pandit model[17], in contrast, includes a second slow inactivation variable  $j$ . Pandit et al included this additional inactivation gate since they based their sodium current formulation on that of Luo and Rudy[30]. It is possible that this variable is slow enough that setting it to a constant value may not play a significant role in the overall behavior of the model, but throughout this work

I have elected to retain it as a variable so that when comparisons are made between the Pandit model and the caveolae-inclusive model, I have controlled for any variation its exclusion might cause.

### 2.3.1 Model Assumptions and Framework

First, it is well established experimentally that in the absence of a  $\beta$ -agonist, caveolae and their sodium channels are electrically isolated from the extracellular environment[21]. Given the relative scales of ions and caveolar necks, it is not unreasonable to assume that little change in caveolar conformation is necessary to produce a pore with virtually no series resistance. Thus, for the purposes of this caveolae-inclusive model it will be assumed that the caveolar neck exists in one of two states, either open enough to allow for the free diffusion of ions or closed enough to prevent any diffusion, and that the transitions between the two states occur rapidly enough to be neglected.

Second, single-caveolae patch clamp experiments suggest that most caveolae contain only a single sodium channel, so it will also be assumed that each closed caveolae sequesters exactly one sodium channel, and no other ion channels, pumps, or exchangers[19]. Undoubtedly, caveolae contain other ion conductances, and in fact studies have shown colocalization of calcium and potassium channels to isolated caveolar membranes[21], but caveolar calcium and potassium currents have yet to be experimentally measured. Therefore, I exclude them in the caveolae-inclusive model since which transport proteins to

include would be a guess and their exclusion simplifies the mathematics.

I shall enforce the first assumption throughout this work, since elimination of this assumption would require more detailed knowledge than currently exists about the biophysics involved in the opening of caveolar necks and would require an accounting for changes in diffusion rates of ions caused by changes in the caveolar neck radius. Modeling this scenario would likely require an intricate three-compartment PDE model. Such a task is outside the scope of this project, but provides a path that future related research may take.

For the purposes of this research I formulate a quasi-three-compartment model in which interactions between compartments occur in two different modes depending upon whether a  $\beta$ -agonist is present or not. When no  $\beta$ -agonist is present and the caveolae are closed, interactions between the intracellular and extracellular compartments are modeled with the unmodified Pandit model, and the interactions between the intracaveolar and intracellular compartments are modeled by a system of ordinary differential equations whose form is dictated by the density and type of ion transporters embedded in the caveolar membrane. In this mode there are no interactions between the intracaveolar and extracellular environments. On the other hand, when a  $\beta$ -agonist is present causing caveolae to open their intracaveolar compartments become part of the extracellular environment and the ion transporters they contain behave the same as their counterparts on the sarcolemma. The diagrams in 2.1 illustrate the model's two modes.

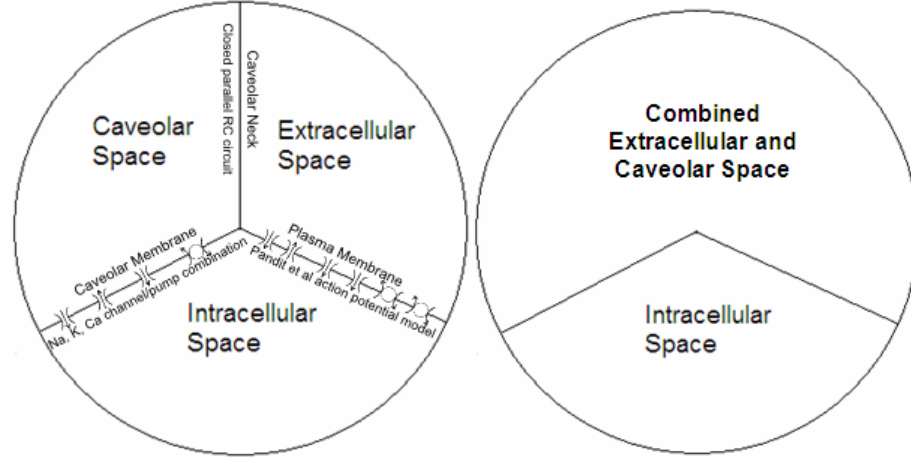


Figure 2.1: Fluid compartment diagrams for the caveolae-inclusive model in each of its two modes.

Under the two aforementioned assumptions we shall see that no interactions occur between the intracaveolar and intracellular environments, so the model merely reduces to the Pandit model with a variable sodium conductance. The resulting caveolar sodium current is

$$I_{cav} = n\gamma_{Na}m^3hj(V_m - E_{Na}) \quad (2.4)$$

where  $n$  is the number of the cell's caveolae which have opened to present their sodium channels to the sarcolemma.

In order to determine a reasonable range of values for  $n$ , let us refer back to the estimates of channel density increase due to injection of  $G_s\alpha$  calculated earlier in this chapter. The estimates were  $332 \text{ channels/pF}$  and  $694 \text{ channels/pF}$ , so for cells the size of the ones modeled by Pandit et al ( $C_m = 100 \text{ pF}$ ), one would expect between 33200 and 69400 additional sodium channels to be added to

the sarcolemma. Assuming one sodium channel per caveolae, these are also estimates for the number of caveolae which open due to the injection of  $G_s\alpha$ .

Given that the Pandit model assumes a whole-cell sodium conductance  $\overline{g_{Na}} = 1064000 \text{ pS}$  and a whole-cell capacitance  $C_m = 100 \text{ pF}$ , and given that under physiologically normal sodium concentrations, such as those assumed in the Pandit model, sodium single-channel conductance is  $\gamma_{Na} \approx 18 \text{ pS}$ [5, 31], the density of sarcolemmal sodium channels assumed by the Pandit model should be approximately  $591 \text{ channels/pF}$ . In this case even the addition of  $332 \text{ channels/pF}$  would increase  $\overline{g_{Na}}$  by over 50%. This seems too high to be a reasonable estimate for increase in whole-cell conductance due to the opening of caveolae.

If on the other hand, it is assumed that the cells on which the Pandit model is based experience the same proportional increase to  $\overline{g_{Na}}$  as those seen in the Lu et al[1] and Palygin et al[2] experiments, (24%-43%), then we would expect the addition of caveolar sodium channels to increase the channel density by between  $144 \text{ channels/pF}$  and  $258 \text{ channels/pF}$  (i.e. it shall be expected the cells to contain between 14400 and 25800 caveolae). For the purposes of this study let us assume the actual number is in the higher end of this more conservative range and consider model cells with 25000 caveolae (i.e. it shall be assumed that  $n$  in the formulation of caveolar sodium current is between 0 and 25000, depending upon the strength of the PKA-independent  $\beta$ -adrenergic response). Note that more refined estimates of caveolar density are necessary to narrow the expected range of values. As mentioned previously, the inconsistencies in

caveolar density estimates I derived from the experimental results may have resulted from problems with controlling for cell size and/or type in the original experiments or from differences in activation methods.

## 2.4 Simulation Protocols

There are two things I wish to test with this model. First, I wish to test whether it can replicate the electrophysiological data related to the PKA-independent  $\beta$ -adrenergic response that have been shown experimentally. Second, I wish to test the effects of these additional sodium currents on action potential morphology, in particular on quantities such as maximum upstroke velocity, maximum overshoot, and action potential duration (APD). To do this, I consider simulations using the unmodified Pandit model to be baseline, and then I compare the results generated by simulations with caveolae-inclusive model to these.

### 2.4.1 Voltage-Clamp Protocol

The key electrophysiological experiments illustrating the degree to which the opening of caveolae modulate whole-cell sodium current are voltage-clamp experiments, so I conduct the same voltage-clamp experiments computationally. Whole-cell  $I_{Na}$  is elicited from cells conditioned at a holding potential of -100 mV before clamping the cell at test potentials between -80 and +50 mV in 5 mV increments. These voltage clamp experiments are done first using the unmodified Pandit model and the results provide the baseline whole-cell

response. Then the experiments are conducted using the caveolae-inclusive model and the results are compared to baseline. As with the corresponding laboratory experiments, I report my results in the form of I-V curves. The simulated extracellular sodium concentration is fixed at 20 mM as was done in the experiments by Lu et al[1] so that meaningful comparisons can be made between the experimental results and the computational results.

#### 2.4.2 Action Potential Protocols

While several studies exist which investigate caveolar sodium currents in the voltage-clamp context, none have investigated their effects on action potential morphology. The caveolae-inclusive model provides a computational setting in which to conduct such an investigation. Again I use the simulated action potential generated by the unmodified Pandit model as baseline and compare its morphology to the morphology of a an action potential generated by the caveolae-inclusive model. To elicit these action potentials, I use the same protocol employed by Pandit et al[17] in which an inward depolarizing stimulus,  $I_{stim}$ , has the form of a rectangular pulse with an amplitude of 0.6 nA and a duration of 5 msec. Initial conditions are chosen to be consistent with the cell's resting state and a stimulus is applied at  $t = 25$  msec. In the absence of any external stimuli, the membrane potential tends toward a steady-state value of approximately -81.3 mV, so the initial conditions are the steady-state values associated with this membrane potential.

Since  $\frac{dv}{dt}$  is directly proportional to the sum of the ionic currents, an increase in sodium current, in the absence of a changes in other ionic currents, must cause an increase in the rate at which membrane voltage changes. I seek to quantify this change by plotting maximum upstroke velocity of the action potential as a function of the number of open caveolae,  $n$ . To do this I elicit action potentials using increasing values of  $n$  in increments of 1000 between 0 and 25000, recording the maximum upstroke velocity in each trial and plotting these velocities against  $n$ . I also record the APD in each trial and plot these durations against  $n$  to expose any dependence that might exist. Note that since the opening of caveolae merely increases the number of sodium channels on the sarcolemma, it is equivalent to increasing whole-cell sodium conductance. The results should be consistent with studies which investigate the effects of increased sodium conductance on action potential morphology.

## 2.5 Results

### 2.5.1 Replication of Experimental Data

As illustrated in Figure 2.2, the caveolae-inclusive model can replicate the effects of  $G_s\alpha$  on sodium current that were seen experimentally by Lu et al[1] and Palygin et al[2]. As expected, the inclusion of caveolar sodium channels in the Pandit model results in current-voltage curves that exhibit similar increases to maximum peak sodium density and to the slopes of the ascending limbs.

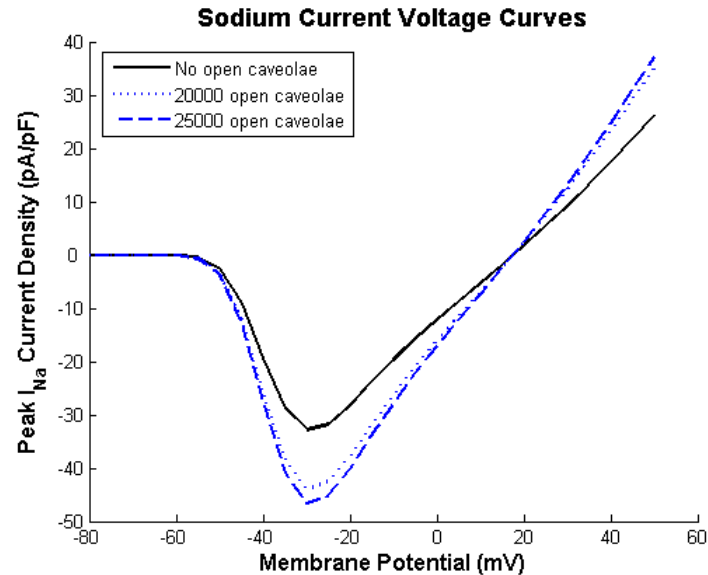


Figure 2.2: Sodium current-voltage curves generated by the Pandit and caveolae-inclusive models exhibit the same general shape as those produced experimentally by Lu et al[1] and Palygin et al[2]. Model parameters were modified to simulate the low sodium concentrations at which the Lu et al[1] and Palygin et al[2] experiments were conducted. In particular, values of  $\gamma_{Na} = 2.2$  pS and  $\bar{g}_{Na} = 0.13 \mu\text{S}$  were substituted while all other parameter values were the same as those listed in the appendix. The solid black curve depicts baseline sodium current response to the voltage-clamp protocol generated by the unmodified Pandit model, while the two blue curves depict the augmented response due to caveolae which have opened to present the sarcolemma with additional sodium channels. The blue curves were generated using the caveolae-inclusive model. The results indicate that 20000 open caveolae will increase maximum peak sodium current by approximately 34%, and 25000 open caveolae leads to an increase of approximately 42%.

One can see from Figure 2.2 that the increases in maximum peak sodium current caused by the inclusion of open caveolae are consistent with the increases measured experimentally. While the peak current densities are an order of magnitude smaller than those produced by Lu et al[1] and about half of those produced by Palygin et al[2], the degree to which the model-generated I-V curves replicate the overall shapes of those produced experimentally suggests that the choice of 20000 - 25000 caveolae per model cell is sensible and that the caveolae-inclusive model provides a good computational venue in which to conduct this investigation. Again note that it is possible that the differences in peak sodium current densities are the result of variations in the types of cells used in the related experiments. It is also possible that these differences are due to problems controlling for cell size that may have affected the experimental results or from differences in the methods of activation used.

### 2.5.2 Caveolar Effects on Action Potential Morphology

Simulations of action potentials with the caveolae-inclusive model show that the inclusion of caveolar sodium currents lead to increases in peak voltage overshoot and maximum upstroke velocity. Furthermore, the maximum upstroke velocity appears to increase linearly with respect to the number of open caveolae (Figure 2.3). This second result is consistent with much of the literature regarding sodium current effects on action potential morphology in which action potential upstroke velocity is shown to increase linearly with increases

in inward sodium current (Figure 2.4).

The most noticeable effect of caveolar sodium current is an increase in peak voltage from approximately 47.8 mV to 54.5 mV, and increase of approximately 5.2% in overall height of the action potential. Less apparent from the graph are its effects on the maximum upstroke velocity and APD. These simulations indicate that the opening of all 25000 caveolae results in an increase of 55 mV per msec in maximum upstroke velocity. This is an increase of approximately 29%. Aside from these differences, the overall action potential morphology is changed very little by the inclusion of a caveolar sodium current. Changes in maximum upstroke velocity, however, are known to have significant effects on conduction velocity of the excitatory wave in cardiac tissue, so we also seek to quantify how maximum upstroke velocity depends upon the amount of caveolar sodium current.

### 2.5.3 Caveolar Effects on Upstroke Velocity and APD

The plot in Figure 2.4.A. illustrates the relationship between maximum upstroke velocity and the number of caveolae which present their sodium channels to the sarcolemma.

Note that the nearly linear relationship between maximum upstroke velocity and percent increase in sodium current is in good agreement with other studies, both experimental[24, 25] and computational[26, 27]. These studies investigated the relationship between maximum upstroke velocity and sodium

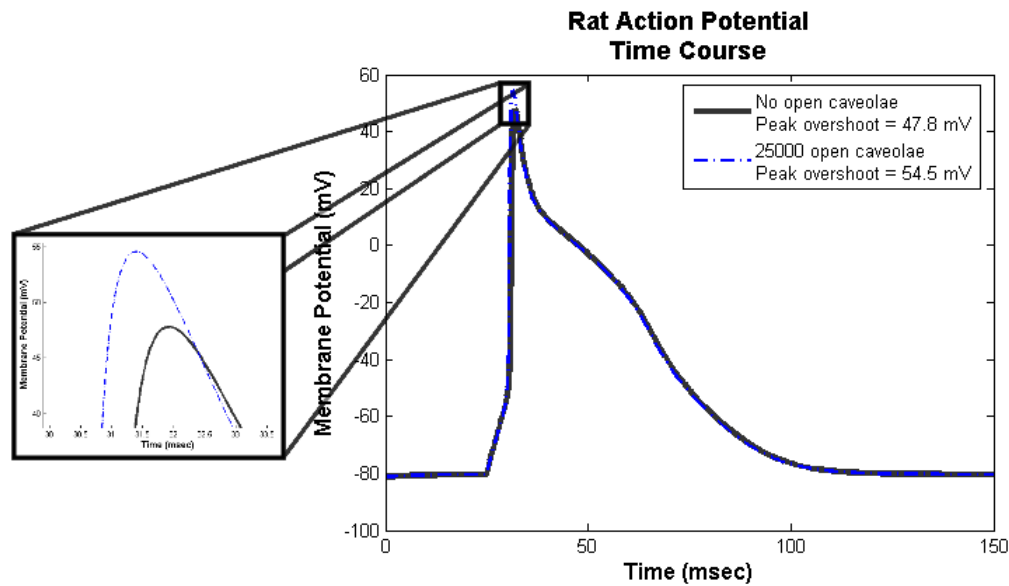


Figure 2.3: Action potential morphology using the Pandit model with and without caveolar sodium current. Notice that the inclusion of 25000 open caveolae results in an approximately 5.2% increase in peak overshoot of the action potential. Less evident from the graph is a 29% increase in maximum upstroke velocity, an important factor in determining the speed of the excitatory wave through the cardiac tissue. Action potential duration, however, appears to be relatively unaffected by the additional sodium conductance introduced by the open caveolae.

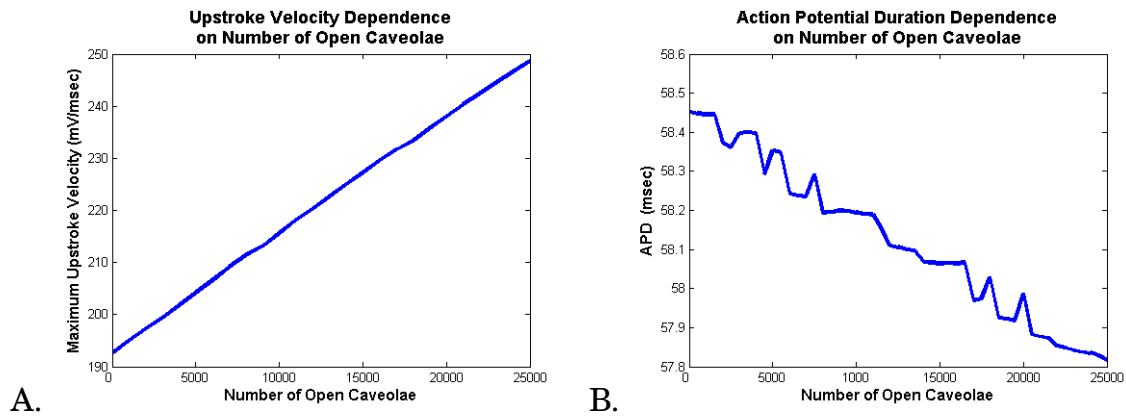


Figure 2.4: Both maximum upstroke velocity and action potential duration exhibit a nearly linear dependence upon the number of open caveolae on the sarcolemma. A. In the case of the maximum upstroke velocity, there exists a strong positive relationship with each 1000 additional open caveolae lending a 1.15% increase to maximum upstroke velocity from baseline. B. In the case of action potential duration, the relationship is negative and substantially weaker. Even the addition of 25000 open caveolae yields only about a 1% decrease in APD.

conductance, a measure of total sodium current.

These results suggest that the dominant relationship between sodium current and maximum upstroke velocity is linear, so I seek to derive that linear relationship directly from the model equations. Recall that during the upstroke, sodium current contributions far outweigh contributions from calcium and potassium since these currents activate at more depolarized potentials and their kinetics are significantly slower. Thus, if one is only concerned with the electrodynamics involved in the upstroke, the reduced system (2.5) provides a suitable model.

$$\begin{aligned}
\frac{dV_m}{dt} &= -\frac{1}{C_m} (\overline{g_{Na}} m^3 h j (V_m - E_{Na}) + n \gamma_{Na} m^3 h j (V_m - E_{Na})) \\
&= -\frac{1}{C_m} (\overline{g_{Na}} + n \gamma_{Na}) m^3 h j (V_m - E_{Na}) \\
\frac{dm}{dt} &= \frac{m_\infty(V_m) - m}{\tau_m(V_m)} \\
\frac{dh}{dt} &= \frac{h_\infty(V_m) - h}{\tau_h(V_m)} \\
\frac{dj}{dt} &= \frac{j_\infty(V_m) - j}{\tau_j(V_m)}
\end{aligned} \tag{2.5}$$

where the voltage-dependencies of the steady-state values and the time constants are given in Appendix A and where the very small changes in  $E_{Na}$  that occur during the action potential are neglected. The goal is to derive from system (2.5)  $\max\left(\frac{dV_m}{dt}\right)$  as a linear function of  $n$  alone, but while substantially simpler than the full Pandit model, system (2.5) still defies a rigorous analysis due to the high degree of coupled nonlinearity it retains. Two options present themselves. One is to exploit a dichotomy between the time scales associated with voltage and the gating variable  $m$  and the time scales associated with the

gating variables  $h$  and  $j$ . Since the gating variables  $h$  and  $j$  change much lower than voltage and the gating variable  $m$ , the system we be reduced to

$$\frac{dV_m}{dt} = -\frac{1}{C_m} (\overline{g_{Na}} + n\gamma_{Na}) m_\infty^3(V_m) h_0 j_0 (V_m - E_{Na}) \quad (2.6)$$

where  $h_0$  and  $j_0$  are the initial values.

On the other hand, if during the upstroke there exist manifolds in the  $V_m m$ -,  $V_m h$ -, and  $V_m j$ -phase planes to which trajectories are attracted, then  $m$ ,  $h$ , and  $j$  can be approximated as functions of  $V_m$  leading to the more accurate reduced system

$$\frac{dV_m}{dt} = -\frac{1}{C_m} (\overline{g_{Na}} + n\gamma_{Na}) m^3(V_m) h(V_m) j(V_m) (V_m - E_{Na}) \quad (2.7)$$

Note in both cases, it is assured that  $\max\left(\frac{dV_m}{dt}\right)$  will be a linear function of  $n$ .

This is because both (2.6) and (2.7) are of the form  $\frac{dV_m}{dt} = (\overline{g_{Na}} + n\gamma_{Na}) \phi(V_m)$ ,

so

$$\frac{d^2V_m}{dt^2} = (\overline{g_{Na}} + n\gamma_{Na}) \frac{d\phi}{dV_m} \frac{dV_m}{dt} \quad (2.8)$$

and since  $\max\left(\frac{dV_m}{dt}\right)$  obviously does not occur when  $\frac{dV_m}{dt} = 0$  and we have  $(\overline{g_{Na}} + n\gamma_{Na}) > 0$ ,  $\max\left(\frac{dV_m}{dt}\right)$  must occur when  $\frac{d\phi}{dV_m} = 0$ . This implies that there exists a  $V_m^*$  satisfying  $\frac{d\phi}{dV_m}(V_m^*) = 0$  such that  $\frac{dV_m}{dt} = (\overline{g_{Na}} + n\gamma_{Na}) \phi(V_m^*)$  is maximal.

### 2.5.3.1 Dichotomous Time Scales Approach

Given that  $C_m = 10^{-4} \mu\text{F}$ ,  $E_{Na} \approx 66 \text{ mV}$ ,  $h_0 = j_0 \approx 0.67$ , and  $m_\infty =$

$$\frac{1}{1 + e^{-\frac{(V_m + 45)}{6.5}}},$$

$$\phi(V_m) \approx -\frac{4500(V_m - 66)}{1 + e^{-\frac{(V_m+45)}{6.5}}} \quad (2.9)$$

so,

$$\frac{d\phi}{dV_m} = -\frac{4500}{1 + e^{-\frac{(V_m+45)}{6.5}}} \left( 1 + \frac{(V_m - 66) e^{-\frac{(V_m+45)}{6.5}}}{6.5 \left( 1 + e^{-\frac{(V_m+45)}{6.5}} \right)} \right) \quad (2.10)$$

Thus, if a maximum upstroke velocity must occur when either

$$\frac{4500}{1 + e^{-\frac{(V_m+45)}{6.5}}} = 0 \quad (2.11)$$

or

$$1 + \frac{(V_m - 66) e^{-\frac{(V_m+45)}{6.5}}}{6.5 \left( 1 + e^{-\frac{(V_m+45)}{6.5}} \right)} = 0 \quad (2.12)$$

Equation (2.11) cannot be satisfied for  $V_m \in \mathbb{R}$ , so we may conclude that  $V_m^*$  is a solution to equation (2.12). To solve equation (2.12) we must resort to numerical methods and doing so shows that in the interval  $[V_{rest}, E_{Na}]$  (which encompasses all of the physiologically relevant values of  $V_m$  during the action potential) equation (2.12) is satisfied by  $V_m^* \approx -28.1$ . Since at the endpoints of the interval  $\frac{dV_m}{dt} = 0$  and since  $\frac{d^2\phi}{dV_m^2}(V_m^*) < 0$ , we may conclude that the maximum of  $\phi$  occurs at  $V_m^* \approx -28.1$  mV. Given this,  $\phi(-28.1) \approx 394170$ , and with  $\overline{g_{Na}} = 1.064 \mu\text{S}$  and  $\gamma_{Na} = 0.000018 \mu\text{S}$

$$\max \frac{dV_m}{dt} = \frac{dV_m}{dt}(V_m^*) = 394170 (\overline{g_{Na}} + n\gamma_{Na}) \approx 7.1n + 419000 \text{ mV/sec} \quad (2.13)$$

In mV/msec the linear relationship becomes

$$\max \frac{dV_m}{dt} \approx 0.0071n + 419 \text{ mV/msec} \quad (2.14)$$

Figure 2.5 provides a plot of this linear relationship compared with the relationship between upstroke velocity and number of open caveolae show in Figure 2.4.A. Obviously, a substantial discrepancy exists between the two relationships suggesting that the changes in the  $h$ -gate and  $j$ -gate values during the upstroke, as well as the contributions of other ionic currents, cannot be ignored. A method which accounts for these changes would likely provide much better agreement between the analytically derived linear relationship and the relationship that exists in the simulations.

### 2.5.3.2 Stable Manifold Approach

I seek here to identify stable manifolds in the various voltage-gating variable phase planes. Due to the slow kinetics of the  $j$ -gate, the calculations can be simplified somewhat by assuming that  $j(V_m) \equiv j_0$ , then for a variety of initial conditions, let us consider the trajectories in the  $V_m m$ - and  $V_m h$ -phase spaces during the action potential upstroke. Figure 2.6 shows these trajectories.

There appears to be a stable manifold in the  $V_m m$ -phase plane to which trajectories are rapidly attracted. However, in the  $V_m h$ -phase plane this is not the case. While no stable manifold appears to exist in the  $V_m h$ -phase plane, the trajectories do appear to all be translations of approximately the same curve  $h(V_m, h_0)$  in the  $h_0$  direction. Unfortunately, I have been unable to extract the

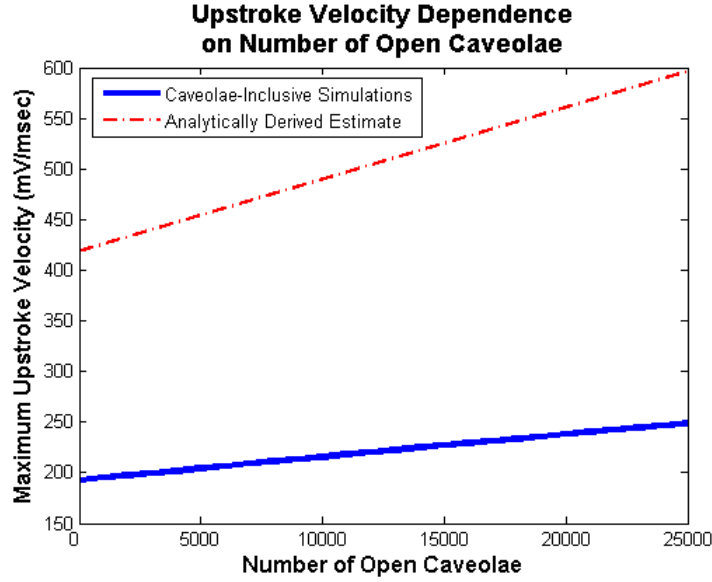


Figure 2.5: Graphs of the maximum upstroke velocity as a function of the number of open caveolae from the caveolae-inclusive model simulations (blue solid line) and using the dichotomous time scales approach which results in equation (2.14) (red dashed-dotted line). Here I have assumed that  $m(V_m) = m_\infty(V_m)$ ,  $h(V_m) \equiv h_0$ , and  $j(V_m) \equiv j_0$ . A severe discrepancy is evident using this method for analytically deriving the expected linear relationship between maximum upstroke velocity and number of open caveolae. Obviously, assuming such fast changes in  $m$  and neglecting the changes in the  $h$ -gate and  $j$ -gate values during the upstroke, as well as the contributions of other ionic currents, has resulted in a substantial over estimation of the maximum upstroke velocity.

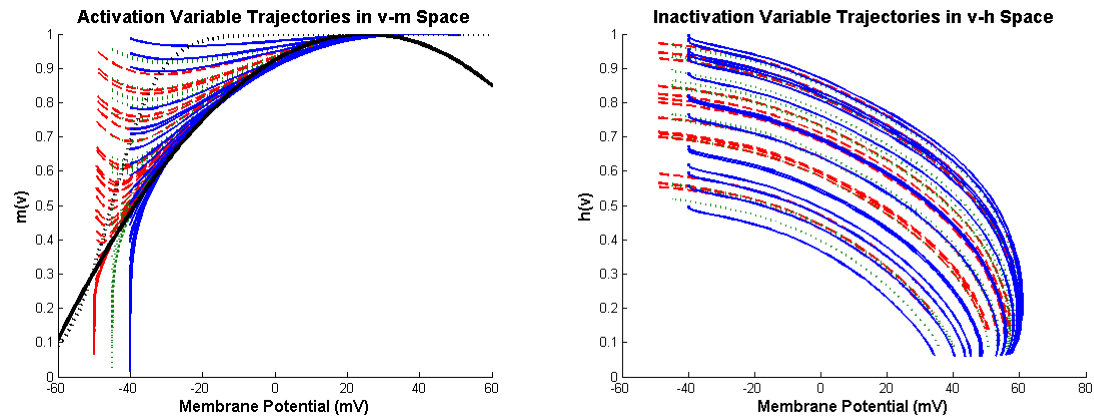


Figure 2.6: These figures show the trajectories of the activation variable  $m$  and inactivation variable  $h$  as functions of membrane potential during the upstroke phase of the action potential for various initial values of each. Trajectories were produced by initiating action potentials by instantaneously depolarizing the membrane to potentials of -50 (red dashed curves), -45 (green dotted curves), and -40 mV (blue solid curves). It appears that there does exist an attractive stable manifold to which the trajectories in  $vm$ -space tend, but no such attractive manifold in  $vh$ -space. For reference the curves  $m_\infty(V_m)$  (black dotted curve) and a curve which offers a good fit to the stable manifold (black solid curve) are superimposed in  $vm$ -space. Note that this clearly shows  $m_\infty(V_m)$  is a poor approximation to the actual trajectories in  $vm$ -space.

equation for the stable  $V_m$ -manifold or the equations for the curves  $h(V_m, h_0)$  directly from the model equations. One possible alternative approach is to choose functions  $m(V_m)$  and  $h(V_m, h_0)$  that provide reasonable fits to the phase portrait data. The functions

$$m(V_m) = 1 - \frac{(V_m - 25)^2}{8.1 \cdot 10^3} \quad (2.15)$$

and

$$h(V_m, h_0) = h_0 - \frac{(V_m + 65)^3}{2.4 \cdot 10^6} \quad (2.16)$$

provide such fits. Then with  $E_{Na} = 66$  mV and  $h_0 = j_0 = 0.67$  which are the initial values used to generate Figure 2.4 the incorporation of (2.15) and (2.16) into the function  $\phi$  yields

$$\phi(V_m) = -6700 \left(1 - \frac{(V_m - 25)^2}{8.1 \cdot 10^3}\right)^3 \left(0.67 - \frac{(V_m + 65)^3}{2.4 \cdot 10^6}\right) (V_m - 66) \quad (2.17)$$

so

$$\begin{aligned} \frac{d\phi}{dV_m} = & -6700 \left(1 - \frac{(V_m - 25)^2}{8.1 \cdot 10^3}\right)^2 \left[ -\frac{6(V_m - 25)(V_m - 66)}{8.1 \cdot 10^3} \left(0.67 - \frac{(V_m + 65)^3}{2.4 \cdot 10^6}\right) \right. \\ & \left. - \left(3 - \frac{3(V_m - 25)^2}{8.1 \cdot 10^3}\right) \frac{(V_m + 65)^2 (V_m - 66)}{2.4 \cdot 10^6} + \left(1 - \frac{(V_m - 25)^2}{8.1 \cdot 10^3}\right) \left(0.67 - \frac{(V_m + 65)^3}{2.4 \cdot 10^6}\right) \right] \end{aligned} \quad (2.18)$$

which clearly has a zero with multiplicity 2 at  $V_m = 115$  mV, and three other real zeros numerically determined to be at  $V_m = 58.59$  mV,  $V_m = 86.52$  mV, and  $V_m = -2.97$  mV. Of these zeros, only  $V_m = -2.97$  mV is in the physiologically relevant range, so we conclude that this is the membrane potential at which  $\frac{dV_m}{dt}$  is maximized. Given this,  $\phi(-2.97) \approx 194400$ , and with  $\overline{g_{Na}} = 1.064 \mu\text{S}$  and

$$\gamma_{Na} = 0.000018 \mu\text{S}$$

$$\max \frac{dV_m}{dt} = \frac{dV_m}{dt}(V_m^*) = 194400 (\overline{g_{Na}} + n\gamma_{Na}) \approx 3.5n + 206840 \text{ mV/sec} \quad (2.19)$$

So in mV/msec (as are the units in Figure 2.4) the linear relationship becomes

$$\max \frac{dV_m}{dt} \approx 0.0035n + 207 \text{ mV/msec} \quad (2.20)$$

In Figure 2.7 I plot this line along with the data points in Figure 2.5.A., and see that while the intercept is substantially closer to the actual value of 193 mV/msec than the intercept calculated using the previous method, this method of analytically extracting the linear relationship produces a slope that is far greater than that generated by simulations with the caveolae-inclusive model. This discrepancy, while disappointing, is not entirely unexpected since by using the reduced model (2.7) and assuming  $j(V_m) = j_0$ , I have neglected not only the slight decrease in  $j$  that occurs during the upstroke, but have neglected all of the other ionic currents (in particular the outward potassium current which would slow the rate of change of  $V_m$  somewhat). It is likely that if these additional factors could be more fully accounted for, the analytically derived linear relationship would have matched the simulation results much better.

## 2.6 Conclusions

In this chapter, I have demonstrated a viable method for estimating the density of caveolae in a cardiac cell that is based on inspections of sodium

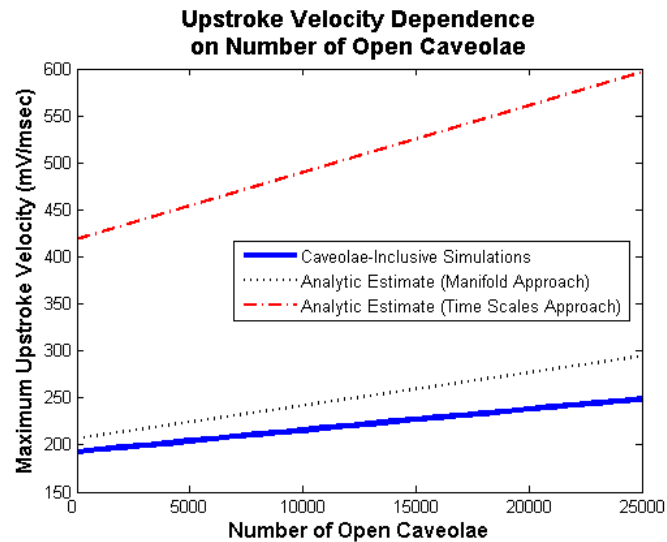


Figure 2.7: A discrepancy is still evident using this method for analytically deriving the expected linear relationship (black dotted line) between maximum upstroke velocity and number of open caveolae, but the discrepancy is much less pronounced than it was in Figure 2.5 (Linear relationship using dichotomous time scales approach is reproduced here as the red dash-dotted line). While this stable manifold approach for analytically extracting the linear relationship appears to work much better than the dichotomous time scales approach, there are obviously subtle interactions between membrane potential and the gating mechanisms involved in the upstroke of the action potential that have still not been captured by this method.

I-V curves. While more targeted experiments which measure both sodium single-channel conductance at various sodium concentrations and changes in whole-cell sodium conductance due to caveolae are necessary to refine these estimates, the results support the conclusions of visual inspections of electron micrographs of rat cardiac cells which show a similar density of caveolae on the subsarcolemma[29]. It appears reasonable to conclude that rat cardiac cells whose total capacitance is approximately 100 pF likely contain between 20000 and 25000 caveolae.

Furthermore, I have shown that incorporating the resultant increase in sodium current due to the opening of all of these caveolae into an existing mathematical model of rat cardiac action potential generates sodium I-V curves that are in good agreement with experimental data. I then used this caveolae-inclusive model to determine the influence these additional caveolar sodium currents may have on action potential morphology. It appears that the inclusion of caveolar sodium current from 25000 caveolae should affect the action potential duration very little, but should result in a 5.2% increase in the height of peak overshoot (measured relative to resting membrane potential) and a nearly 30% increase in maximum upstroke velocity. In addition, I have shown that the increases in maximum upstroke velocity appear to be directly proportional to the number of caveolae that are open at the time of stimulus and have attempted to extract this linear relationship from the caveolae-inclusive model.

These findings are important because increases in maximum upstroke velocity are known to increase conduction speed of the excitatory wave in cardiac tissue. For instance, the 1983 experimental study conducted by Walton and Fozzard[26] which investigated the relationship between maximum upstroke velocity and conduction speed of the excitatory wave concluded that the normalized conduction velocity is directly related to the square root of the normalized maximum upstroke velocity. Therefore, since the inclusion of 25000 open caveolae in the model results in a maximum upstroke velocity that is 129% of baseline, it suggests that the caveolar-associated PKA-independent  $\beta$ -adrenergic pathway alone can be expected to increase conduction velocity by up to 14%.

## **CHAPTER 3**

### **SIMPLIFIED THREE-VARIABLE MODEL**

#### **3.1 Introduction to the Three-Variable Model**

While the physiological detail of models such as the Pandit model[17] provide highly accurate simulations, their complexity is limiting from a mathematical perspective. Not only does their complexity render them computationally expensive, but it makes the process of extracting specific dependencies between variables and parameters cumbersome, at best, and often impossible. With large, coupled, nonlinear systems, the application of mathematical tools such as phase portrait analysis, stability analysis, asymptotic analysis, and bifurcation theory becomes intractable.

For this reason several simpler models of action potential have been developed that preserve qualitative features of the more complicated models, while at the same time allowing for rigorous mathematical analysis. Among these are the Fitzhugh-Nagumo model[32, 33] which is a dimensional reduction of the original Hodgkin-Huxley model, the Fenton-Karma model[34] offering a similar simplification of standard cardiac models, and the Mitchell-Schaeffer model[18], a two-current model which provides qualitatively accurate reproduction of the cardiac action potential morphology and restitution properties. In this chapter, I offer a new model based on the last of these which retains much of the simplicity and low-dimensionality of the original

two-current model, but incorporates a caveolar sodium current.

### 3.2 Mitchell-Schaeffer Two-Current Model

The Mitchell-Schaeffer model[18], shown here as system (3.1), is system of two nonlinear coupled ordinary differential equations based in part on the work of Fenton and Karma[34, 35].

$$\begin{aligned} \frac{dv}{dt} &= \frac{hw^2(1-v)}{\tau_{in}} - \frac{v}{\tau_{out}} \\ \frac{dh}{dt} &= \begin{cases} \frac{-h}{\tau_{close}} & v \geq v_{gate} \\ \frac{1-h}{\tau_{open}} & v < v_{gate} \end{cases} \end{aligned} \quad (3.1)$$

The variable  $v$  represents a normalized membrane potential that ranges from zero to one. The gating variable  $h$  also ranges from zero to one and governs the voltage-dependence of the inward current. The right hand side of the first ordinary differential equation can be thought of as the sum of a voltage-gated inward current and an ungated outward current, respectively. Often a periodic forcing term called the stimulus current,  $I_{stim}$ , is included in the first ordinary differential equation if the model is used to simulate cardiac pacing. Single action potentials, however, can be simulated without this term if suitable initial conditions are chosen (i.e. if  $h_0$  is near its resting value, and  $v_0$  is above threshold). A typical action potential generated by this model is shown in Figure 3.1.

The shape of this action potential differs significantly from the shape generated by the Pandit model[17]. This is due to the fact that the Pandit

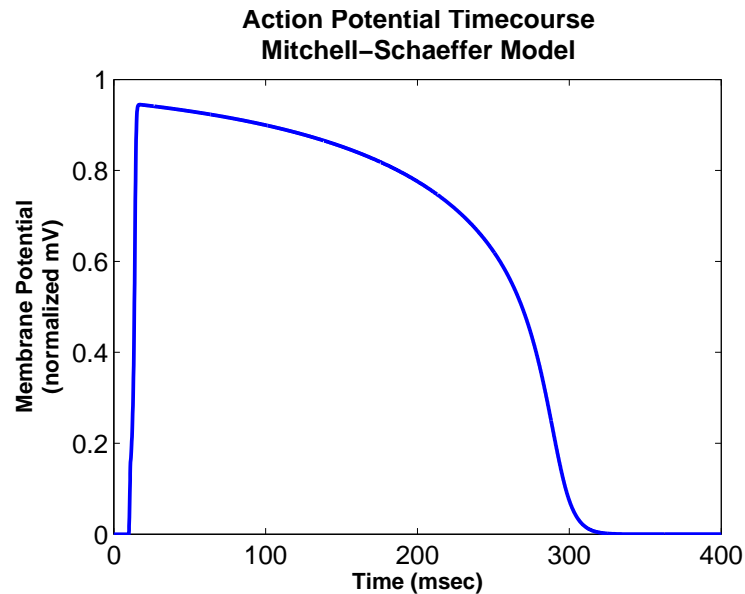


Figure 3.1: This figure shows an action potential generated by the Mitchell-Schaeffer two-current model. Note that it exhibits the characteristic four-phase morphology - upstroke, plateau, repolarization, recovery - of all cardiac action potentials, but has a much more pronounced plateau phase than a rat action potential since this model was designed to simulate the frog cardiac action potential. Nevertheless, the simplicity and analytic accessibility of this model makes it an appealing choice for use as a guide in developing a simplified model of rat cardiac action potential.

model[17] is rat-specific, while the Mitchell-Schaeffer model was designed for comparisons with the frog cardiac action potential. The same general features are present in both, though. There is a rapid depolarization phase caused by an initial strong inward current followed by a plateau phase (much less pronounced in the rat action potential) caused by opposing inward and outward currents, and then a repolarization phase occurring once the outward current dominates. Upon repolarization the cell membrane is returned to its stable resting state poised for the arrival of the next suprathreshold depolarizing stimulus.

Mitchell and Schaeffer derive a one-dimensional iterative map directly from their model which calculates action potential duration as a function of the previous diastolic interval - a restitution portrait. Despite the Mitchell-Schaeffer model's simplicity, the qualitative features of its associated restitution portrait are in excellent agreement with the rate dependent features of cardiac action potential demonstrated by Hall et al[36] in a 1999 experimental study. The restitution portrait is characterized by increasingly rapid pacing leading first to cardiac alternans - alternation between action potentials with normal duration and those with an abbreviated duration - and eventually to a 2:1 Wenkebach pattern in which an action potential is elicited by every other stimulus[18]. These results suggest that while mathematically simple, the Mitchell-Schaeffer two-current model[18] provides an accurate portrayal of whole-cell electrodynamics.

### 3.3 Formulation of the Three-Variable Model

Due to this combination of simplicity and physiological relevance the two-current model is appealing for use in this research, but it bears one significant shortfall; there is only a single term,  $I_{in}$ , to account for all inward currents. In effect, this model combines the dominant inward currents - carried by sodium and calcium - into a single voltage-gated inward current. Since this research is primarily focused on the effects of increasing the sodium current alone, it becomes necessary to distinguish between the sodium and calcium components of  $I_{in}$ , if the Mitchell-Schaeffer model[18] is to be adapted for use in this research. Doing so results in a three-current model of cardiac action potential in which each of the dominant ionic currents - sodium, calcium, and potassium - is assigned its own term.

I achieve this de-coupling of the sodium and calcium currents by introducing a second gating variable,  $p$ , analogous to the  $d$ -gate in the Beeler-Reuter[14] and Pandit[17] models of cardiac action potential. The term  $(1 - \frac{p}{2})$  is also incorporated into the calcium current and this plays a gating role similar to the  $f$ -gate in the Beeler-Reuter model[14] and the  $f_{11}$ -gate in the Pandit model[17]. By eliminating the independent inactivation gate ( $f$ -gate) in this model, one less differential equation is necessary. The choice of using  $(1 - \frac{p}{2})$  to stand in for inactivation is due to the fact that in the Pandit model, the time course of  $(1 - \frac{d}{2})$  provides a rough approximation to the time course of the  $f_{11}$ -gate which has a value of approximately 1 when the cell is at rest (and  $d = 0$ )

and does not decay completely to zero during the action potential. It should be noted that this is only a rough approximation since the time constants of calcium activation and inactivation are substantially different and  $f_{11}$  does not reach a minimum of less than 0.5. However, it is believed that any lack of accuracy in modeling calcium inactivation is worth the increase in analytic tractability that a three-, rather than four-, variable model affords.

Additionally, my new model needs to simulate the rat cardiac action potential specifically, so I choose parameter values that provide an optimal fit (after rescaling) with the action potential produced by the Pandit model[17].

System (3.2) is the formulation of my new model

$$\begin{aligned}
 \frac{dv}{dt} &= \underbrace{\frac{\kappa h v^2 (1-v)}{\tau_{Na}}}_{I_{Na}+I_{cav}} + \underbrace{\frac{p(1-\frac{p}{2})(1-v)}{\tau_{Ca}}}_{I_{Ca}} - \underbrace{\frac{v}{\tau_K}}_{I_K} \\
 \frac{dh}{dt} &= \begin{cases} \frac{-h}{\tau_{hc}} & v \geq v_h \\ \frac{1-h}{\tau_{ho}} & v < v_h \end{cases} \\
 \frac{dp}{dt} &= \begin{cases} \frac{-p}{\tau_{pc}} & v < v_p \\ \frac{1-p}{\tau_{po}} & v \geq v_p \end{cases}
 \end{aligned} \tag{3.2}$$

In this formulation, the parameter  $\kappa$  modulates the amount of caveolar sodium current that is present. A value of  $\kappa = 1$  means that total sodium current is 100% of baseline (the scenario in which no caveolae are open) whereas a value of  $\kappa > 1$  means that some caveolae are open, resulting in an augmentation of the total sodium current.

The protocol for eliciting an action potential with this model will be to

choose initial conditions  $v = 0.21$ ,  $h = 1$ , and  $p = 0$  and let the model evolve due to the system of equations (3.2). Doing so is tantamount to applying an instantaneous depolarizing stimulus that drives the membrane potential to the superthreshold value of 0.21 at  $t = 0$ . The specific choice of the initial value  $v = 0.21$  will be explained in the following section where I also determine the parameter values which provide an optimal fit with the Pandit model.

### 3.3.1 Preliminary Parameter Selection

The behavior of this system depends upon the choice of nine parameter values - four time constants related to the channel gating kinetics, three parameters related to the strength of the ionic currents, and two threshold potentials related to the transition of the channels from open conformation to closed/inactive conformations. What is needed is a set of parameter values which ensures that the action potential morphology and ionic current time courses are consistent with those generated by the Pandit model[17] of rat action potential. As a method of first approximation, I devise specific comparisons between these two models which allow for the extraction of parameter values. This set of values pinpoints a location in the parameter space which hopefully is near the optimal set of parameter values. I then conduct a systematic search in this vicinity for values which optimize the fit with the Pandit model.

In order to make the necessary comparisons the action potentials must be on the same scale. However, the voltage in the system of equations (3.2) has

been normalized so that it ranges from 0 to 1. If the three-variable model is thought of in the context of the Hodgkin-Huxley formalism, one can gain insight into how this normalization is achieved and can derive the appropriate change of variables so that meaningful comparisons can be made. In this context, the driving force for potassium is  $(v - 0)$ , suggesting a rescaled potassium Nernst potential of 0 mV.

Likewise, the driving force for both sodium and calcium is  $(v - 1)$ , suggesting that the rescaled Nernst potential for each is +1 mV. Recall that due to the relatively high permeability of the resting membrane to potassium compared to sodium and calcium, the resting membrane equilibrates near the potassium Nernst potential. In this case, the resting potential for the Pandit model is -81.36 mV. Also, in the Pandit model, the Nernst potentials for sodium and calcium are each approximately +66 mV.

Therefore, defining the membrane potential in the Pandit model as  $\bar{v}$ , the relation  $v = \frac{(\bar{v} + 81.36)}{(66 + 81.36)} = \frac{(\bar{v} + 81.36)}{(147.36)}$  provides us with a way to transform the voltage between the physiological scale and the normalized scale. Additionally, the time constants for the currents are scaled in the following manner:  $\tau_{Na} = \frac{C_m \overline{\tau_{Na}}}{0.68}$ ,  $\tau_{Ca} = C_m \overline{\tau_{Ca}}$ , and  $\tau_K = C_m \overline{\tau_K}$  where  $C_m$  is membrane capacitance. Lastly, to ensure that the initial value of the sodium inactivation gate has a value of 0.68, let us scale  $h$ ,  $\tau_{ho}$ , and  $\tau_{hc}$  in the following manner:  $h = \frac{\bar{h}}{0.68}$ ,  $\tau_{ho} = \frac{\overline{\tau_{ho}}}{0.68}$ , and  $\tau_{hc} = \frac{\overline{\tau_{hc}}}{0.68}$ . The physiologically scaled version of the three-variable model then has the form:

$$\begin{aligned}
\frac{d\bar{v}}{dt} &= -\left(\frac{1}{C_m}\right) \left( \underbrace{\frac{\kappa\bar{h} \left(\frac{\bar{v} + 81.36}{147.36}\right)^2 (\bar{v} - 66)}{\bar{\tau}_{Na}}}_{I_{Na} + I_{cav}} + \underbrace{\frac{\bar{p} \left(1 - \frac{\bar{p}}{2}\right) (\bar{v} - 66)}{\bar{\tau}_{Ca}}}_{I_{Ca}} + \underbrace{\frac{\bar{v} + 81.36}{\bar{\tau}_K}}_{I_K} \right) \\
\frac{d\bar{h}}{dt} &= \begin{cases} \frac{-\bar{h}}{\bar{\tau}_{hc}} & \frac{\bar{v} + 81.36}{147.36} \geq v_h \\ \frac{0.68 - \bar{h}}{\bar{\tau}_{ho}} & \frac{\bar{v} + 81.36}{147.36} < v_h \end{cases} \\
\frac{d\bar{p}}{dt} &= \begin{cases} \frac{-\bar{p}}{\bar{\tau}_{pc}} & \frac{\bar{v} + 81.36}{147.36} < v_p \\ \frac{1 - \bar{p}}{\bar{\tau}_{po}} & \frac{\bar{v} + 81.36}{147.36} \geq v_p \end{cases}
\end{aligned} \tag{3.3}$$

Notice that  $\bar{\tau}_{Na}$ ,  $\bar{\tau}_{Ca}$  and  $\bar{\tau}_K$  have units  $sec/\mu F$  (or equivalently,  $1/\mu S$ ),  $\bar{\tau}_{hc}$ ,  $\bar{\tau}_{ho}$ ,  $\bar{\tau}_{pc}$ , and  $\bar{\tau}_{po}$  have units of seconds,  $\bar{v}$  has units mV, and  $\bar{h}$ ,  $\bar{p}$ ,  $v_h$ ,  $v_p$  and  $\kappa$  are dimensionless. For the purposes of optimizing parameters, I deal exclusively with this model and assume no caveolar contribution (i.e. we assume  $\kappa = 1$ ) so that my results can be compared directly with those produced by the unmodified Pandit model. I also use the same protocol for eliciting an action potential in both models. Instantaneously depolarizing the membrane in the Pandit model over a range of values reveals that the threshold potential is approximately  $\bar{v} = -57$  mV, which corresponds to a normalized threshold potential of  $v \approx 0.165$ . So, choosing  $V_m(0) > -57$  mV while setting the remaining initial conditions to the resting values will result in an action potential. For the purposes of the parameter selection process Let us choose  $V_m(0) = \bar{v}(0) = -50$  mV. This corresponds to a normalized initial membrane potential of  $v = 0.21$ .

### 3.3.1.1 Selecting $\bar{\tau}_K$

Due to the relative simplicity of the potassium current term, I shall begin the search for an optimal set of parameter values with a derivation of  $\bar{\tau}_K$ .

I seek a set of parameter values which produces an action potential morphology that is as close to the morphology of the Pandit model-generated action potential as possible. Likewise, I expect the morphologies of the individual ionic currents to also match those generated by the Pandit model as closely as possible. By initiating an action potential with the Pandit model using an instantaneous depolarizing pulse which drives the membrane to -50 mV, the maximum potassium current that is achieved is approximately 1.75 nA. Since, in the three-variable model, the potassium current is a linear function of membrane potential, this maximum must be achieved when membrane potential reaches its peak. The peak overshoot of the simulated action potential needs to be approximately 50 mV, so by substitution then, it is necessary that

$$I_{K,max} = \frac{50 + 81.36}{\overline{\tau_K}} = 1.75 \quad (3.4)$$

which yields the parameter value  $\overline{\tau_K} \approx 75 \text{ sec}/\mu F$ .

### 3.3.1.2 Selecting $v_p$ , $\overline{\tau_{po}}$ , and $\overline{\tau_{pc}}$

In order for the calcium current to match that generated by the Pandit model, the following equation must hold.

$$\frac{\bar{p} \left(1 - \frac{\bar{p}}{2}\right) (\bar{v} - 66)}{\overline{\tau_{Ca}}} = g_{CaL} d \left[ \left(0.9 + \frac{Ca_{inact}}{10}\right) f_{11} + \left(0.1 - \frac{Ca_{inact}}{10}\right) f_{12} \right] (V_m - E_{CaL}) \quad (3.5)$$

Since  $E_{CaL} \approx 66 \text{ mV}$  throughout the action potential and since I am choosing parameters so that  $\bar{v} \approx V_m$ , we need only to satisfy the equation,

$$\frac{\bar{p} \left(1 - \frac{\bar{p}}{2}\right)}{\overline{\tau_{Ca}}} = g_{CaL} d \left[ \left(0.9 + \frac{Ca_{inact}}{10}\right) f_{11} + \left(0.1 - \frac{Ca_{inact}}{10}\right) f_{12} \right] \quad (3.6)$$

In other words, parameter values related to the calcium gating mechanism are required so that

$$d \left[ \left( 0.9 + \frac{Ca_{inact}}{10} \right) f_{11} + \left( 0.1 - \frac{Ca_{inact}}{10} \right) f_{12} \right] \quad (3.7)$$

is proportional to

$$\bar{p} \left( 1 - \frac{\bar{p}}{2} \right) \quad (3.8)$$

Plotting the time course of (3.7) during an action potential reveals that it reaches a maximum value of approximately 0.9, so since (3.8) has a maximum of 0.5, parameter values  $v_p$ ,  $\overline{\tau_{po}}$ , and  $\overline{\tau_{pc}}$  are sought such that the time course of  $1.8\bar{p} \left( 1 - \frac{\bar{p}}{2} \right)$  is a best fit with (3.7).

Since the ordinary differential equation governing  $\bar{p}$  is piecewise linear in  $\bar{p}$ , it can be solved explicitly for a given membrane potential time course yielding

$$\bar{p}(t) = \begin{cases} 0 & 0 \leq t < t_1^{\bar{p}} \\ \left( 1 - e^{-\frac{(t-t_1^{\bar{p}})}{\overline{\tau_{po}}}} \right) & t_1^{\bar{p}} \leq t \leq t_2^{\bar{p}} \\ e^{-\frac{(t-t_2^{\bar{p}})}{\overline{\tau_{pc}}}} & t > t_2^{\bar{p}} \end{cases} \quad (3.9)$$

where  $t_1^{\bar{p}}$  represents the first time at which  $\frac{\bar{v} + 81.36}{147.36} = v_p$  and  $t_2^{\bar{p}}$  is the second time at which  $\frac{\bar{v} + 81.36}{147.36} = v_p$ . Here it is assumed that the  $\bar{p}$ -gates are all closed at resting membrane potential (i.e.,  $\bar{p}_0 = 0$ ). A naive search of the parameter space suggests that the values  $v_p \approx 0.8$ ,  $\overline{\tau_{po}} \approx 0.0005$  seconds, and  $\overline{\tau_{pc}} \approx 0.009$  seconds offer a very close fit as illustrated in Figure (3.2).

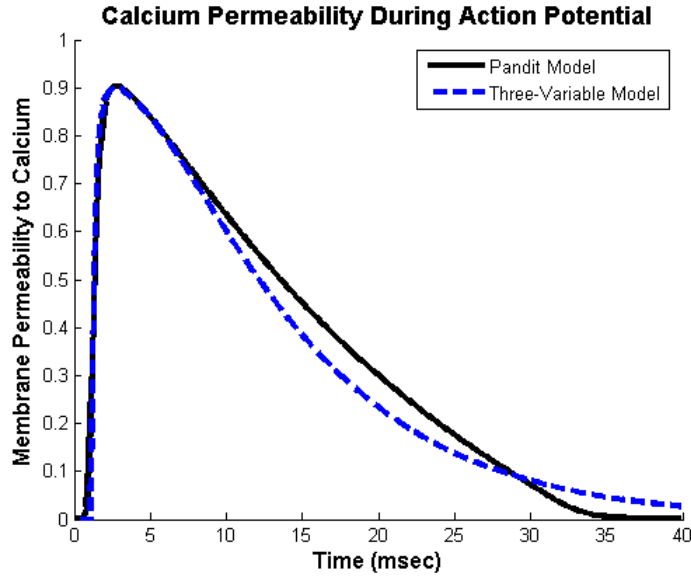


Figure 3.2: This plot shows the time course of the membrane permeability to calcium (—) in the Pandit model given by (3.7) and that of the three-variable model (- - -) given by (3.8) provided the time course of the membrane potential is the time course of the Pandit-model generated action potential. In (3.8)  $\bar{p}(t)$  is defined as in (3.9). The parameter values  $v_p \approx 0.8$ ,  $\overline{\tau_{po}} \approx 0.0005$  seconds, and  $\overline{\tau_{pc}} \approx 0.009$  seconds appear to offer a very close fit between (3.7) and (3.8) suggesting that these parameter values are near those which would optimize the overall fit of the calcium currents in the two models.

### 3.3.1.3 Selecting $\overline{\tau_{Ca}}$

In the simulations using the Pandit model, the peak calcium current of -1.182 nA occurs approximately 7 msec after the stimulus. At this time, the membrane permeability to calcium, given by (3.7), is approximately 0.76 and the membrane potential is approximately 14.68 mV. Then at the time of peak calcium current one should expect that

$$1.8\bar{p} \left(1 - \frac{\bar{p}}{2}\right) \approx 0.76 \quad \Rightarrow \quad \bar{p} \left(1 - \frac{\bar{p}}{2}\right) \approx 0.42 \quad (3.10)$$

and

$$\bar{v} \approx 14.68 \quad (3.11)$$

These approximations suggest that

$$I_{Ca,max} \approx \frac{0.42 \cdot (14.68 - 66)}{\overline{\tau_{Ca}}} \approx -1.182 \quad (3.12)$$

which yields a value of  $\overline{\tau_{Ca}} \approx 18.3 \text{ sec}/\mu F$ .

### 3.3.1.4 Selecting $v_h$ , $\overline{\tau_{ho}}$ , and $\overline{\tau_{hc}}$

I approach the selection of  $v_h$ ,  $\overline{\tau_{ho}}$ , and  $\overline{\tau_{hc}}$  in the same manner as I approached the selection of  $v_p$ ,  $\overline{\tau_{po}}$ , and  $\overline{\tau_{pc}}$ , with one minor modification. Since at this stage in the research I am only concerned with modeling a single action potential and since the  $\bar{h}$ -gate's only role is to rapidly inactivate sodium current and terminate the upstroke phase of the action potential, it is not necessary to worry about the recovery of the  $\bar{h}$ -gate later in the repolarization phase and subsequent diastolic interval. So, for the purposes of this investigation it can

be assumed that the  $\bar{h}$ -gate does not recover at all (i.e.  $\overline{\tau_{ho}}$  can be chosen to be very large, say on the order of 1000 seconds). In future research when the behavior of cells which are being paced by periodic depolarizing stimuli is of interest, this recovery from inactivation will become important.

In order for the sodium current to match that generated by the Pandit model then, the following equation must hold.

$$\frac{\bar{h} \left( \frac{\bar{v} + 81.36}{147.36} \right)^2 (\bar{v} - 66)}{\overline{\tau_{Na}}} = g_{Na} m^3 h (V_m - E_{Na}) \quad (3.13)$$

Since  $E_{Na} \approx 66$  mV throughout the action potential and since I am choosing parameters so that  $\bar{v} \approx V_m$ , it is only necessary to satisfy the equation,

$$\frac{\bar{h} \left( \frac{\bar{v} + 81.36}{147.36} \right)^2}{\overline{\tau_{Na}}} = g_{Na} m^3 h \quad (3.14)$$

In other words, let us select parameter values related to the sodium gating mechanism such that

$$m^3 h \quad (3.15)$$

is proportional to

$$\bar{h} \left( \frac{\bar{v} + 81.36}{147.36} \right)^2 \quad (3.16)$$

As was the case for  $\bar{p}$ , the ordinary differential equation governing  $\bar{h}$  is piecewise linear in  $\bar{h}$  for a given membrane potential time course and so can be solved explicitly. Additionally, since I am only concerned with the inactivation of  $\bar{h}$ , I need only solve this “piece” of the differential equation, yielding

$$\bar{h}(t) = \begin{cases} 0.68 & t < t_1^{\bar{h}} \\ 0.68e^{-\frac{(t-t_1^{\bar{h}})}{\tau_{hc}}} & t_1^{\bar{h}} \leq t \end{cases} \quad (3.17)$$

where  $t_1^{\bar{h}}$  represents the first time at which the membrane potential increases above  $v_h$ . Matters can be simplified even further  $v_h$  is chosen at or below the normalized initial value of the membrane potential. By inspection of the equation for  $h_\infty$ , the voltage-dependent steady-state value of the  $h$ -gate in the Pandit model (see Appendix A), it is easy to see that the inflection point for  $h_\infty$  occurs at the membrane potential -76.1 mV ( $\approx 0.036$  in normalized membrane potential). The value of the membrane potential at this inflection point value provides a good estimate for the voltage at which inactivation of the sodium current begins in earnest, so let us set  $v_h = 0.036$  in this model. Since the initial instantaneous depolarization is higher than this, we may claim that for the duration of the action potential  $\bar{h}(t) = 0.68e^{-\frac{t}{\tau_{hc}}}$  with  $t = 0$  denoting the time of stimulus.

Plotting the time course of (3.15), the membrane permeability to sodium, during an action potential reveals that it reaches a maximum value of approximately 0.45, so in order to ensure that (3.16) is scaled to exhibit this same peak current, (3.16) must be multiplied by a factor of

$$\frac{0.45}{\max_t \left( \bar{h} \left( \frac{\bar{v} + 81.36}{147.36} \right)^2 \right)} \quad (3.18)$$

Of course, the value of  $\max_t \left( \bar{h} \left( \frac{\bar{v} + 81.36}{147.36} \right)^2 \right)$  is dependent upon the choice of  $\overline{\tau_{hc}}$ , so the task reduces to choosing  $\overline{\tau_{hc}}$  in such a way that

$$\frac{0.45}{\max_t \left( \bar{h} \left( \frac{\bar{v} + 81.36}{147.36} \right)^2 \right)} \left( \bar{h} \left( \frac{\bar{v} + 81.36}{147.36} \right)^2 \right) \quad (3.19)$$

provides the best fit with (3.15). A sweep of a large range of values suggests that  $\overline{\tau_{hc}} \approx 0.00045$  seconds provides such a fit as is illustrated in figure (3.3).

Note that in the Pandit model, the membrane permeability to sodium remains near zero for a short time after the stimulus, while in the three-variable model this permeability instantaneously jumps to approximately 0.35 upon the arrival of the stimulus. This difference is due to the fact that sodium activation in the three-variable model is represented by  $\left( \frac{\bar{v} + 81.36}{147.36} \right)^2$  which obviously reacts, without delay, to changes in membrane potential. Nevertheless, the overall shape of the curves is a relatively good match and so it can be concluded that the parameter values  $v_h \approx 0.036$ ,  $\overline{\tau_{hc}} \approx 0.00045$  seconds, and  $\overline{\tau_{ho}} \approx 1000$  seconds, provide relatively good estimates for the optimal values.

### 3.3.1.5 Selecting $\overline{\tau_{Na}}$

In the simulations using the Pandit model, the peak sodium current of approximately -20.66 nA occurs approximately 0.82 msec after the stimulus. At this time, the membrane permeability to sodium is approximately 0.403 and the membrane potential is approximately -3.13 mV. Then at the time of peak sodium current it is expected that

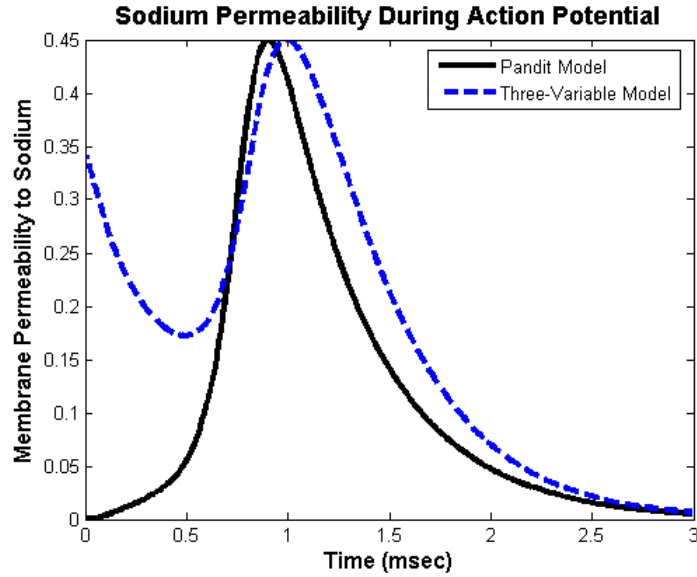


Figure 3.3: This plot shows the time course of the membrane permeability to sodium (—) in the Pandit model given by (3.15) and that of the three-variable model (- - -) given by (3.19) provided the time course of the membrane potential is the time course of the Pandit-model generated action potential. In (3.19),  $\bar{h}(t) = 0.68e^{-\frac{t}{\bar{\tau}_{hc}}}$  with  $\bar{\tau}_{hc} = 0.00045$  seconds and  $\frac{0.45}{\max\left(\bar{h}\left(\frac{\bar{v} + 81.36}{147.36}\right)^2\right)} = 11.25$ . It appears that this choice of time constant provides a reasonably good fit between (3.7) and (3.19) suggesting that this parameter value is near the value which would optimize the overall fit of the sodium currents in the two models. However, one major difference between the two plots is evident at the beginning of their time courses. In the Pandit model, the membrane permeability to sodium at the time of the stimulus is essentially zero, while in the three-variable model this permeability instantaneously jumps to approximately 0.35 upon the arrival of the stimulus, a phenomenon which is discussed further in the text.

$$11.2535\bar{h} \left( \frac{\bar{v} + 81.36}{147.36} \right)^2 \approx 0.403 \quad \Rightarrow \quad \bar{h} \left( \frac{\bar{v} + 81.36}{147.36} \right)^2 \approx 0.0358 \quad (3.20)$$

and

$$\bar{v} \approx -3.13 \quad (3.21)$$

These approximations suggest that

$$I_{Na,max} \approx \frac{0.0358 \cdot (-3.13 - 66)}{\overline{\tau_{Na}}} \approx -20.66 \quad (3.22)$$

which yields the estimate  $\overline{\tau_{Na}} \approx 0.12 \text{ sec}/\mu F$ .

### 3.3.2 Preliminary Results

Incorporating this set of parameter values into the three-variable model generates results that are summarized in Figure 3.4. These values appear to produce an action potential morphology which is quite similar to that generated by the Pandit model with the only noteworthy differences being a higher peak overshoot and a more rapid repolarization in the case of the three-variable model. An examination of the individual currents suggests that the higher peak overshoot is the result of a substantially larger sodium current in the three-variable model than in the Pandit model. This higher peak overshoot in turn necessarily results in a larger potassium current which is responsible for repolarization. In addition, peak sodium current occurs about 0.6 msec earlier in the three-variable model than in the Pandit model. This is the result of the fact that membrane permeability to sodium exhibits a slight delay after

the stimulus in the Pandit model, while it reacts instantaneously to changes in membrane potential as already discussed in reference to Figure 3.3. Nevertheless, this set of parameter values provides us with a good starting point in parameter space from which to search for an optimal set.

### 3.3.2.1 Optimization of Parameter Values

I refine these estimates using a simple Monte Carlo method. The method is as follows. We begin by fixing the parameter values which need no further optimization. These are  $v_h = 0.036$  and  $\overline{\tau_{ho}} = 1000$ , leaving seven parameters left to be optimized. Consider the preliminary values of these seven remaining parameters,  $v_p = 0.8$ ,  $\overline{\tau_{Na}} = 0.12$ ,  $\overline{\tau_{hc}} = 0.00045$ ,  $\overline{\tau_K} = 75$ ,  $\overline{\tau_{Ca}} = 18.3$ ,  $\overline{\tau_{po}} = 0.0005$ , and  $\overline{\tau_{pc}} = 0.009$ , to be a point,  $q_0$ , in seven-dimensional parameter space. Construct a randomly generated set of  $N$  points,  $q_1, q_2, \dots, q_N$ , in a specified neighborhood of  $q_0$  and for each point assess how close the resulting action potential morphology and ionic current time courses are from those generated by the Pandit model.

This means that we must also have a measure of the “distance” between the results generated by the two models. It shall be expected that the models share several key characteristics. First, the peak overshoot should be nearly the same for each model. Not only is this an important component of overall action potential morphology, but enforcing this requirement ensures that the peak potassium currents are also similar. Second, the maximum upstroke

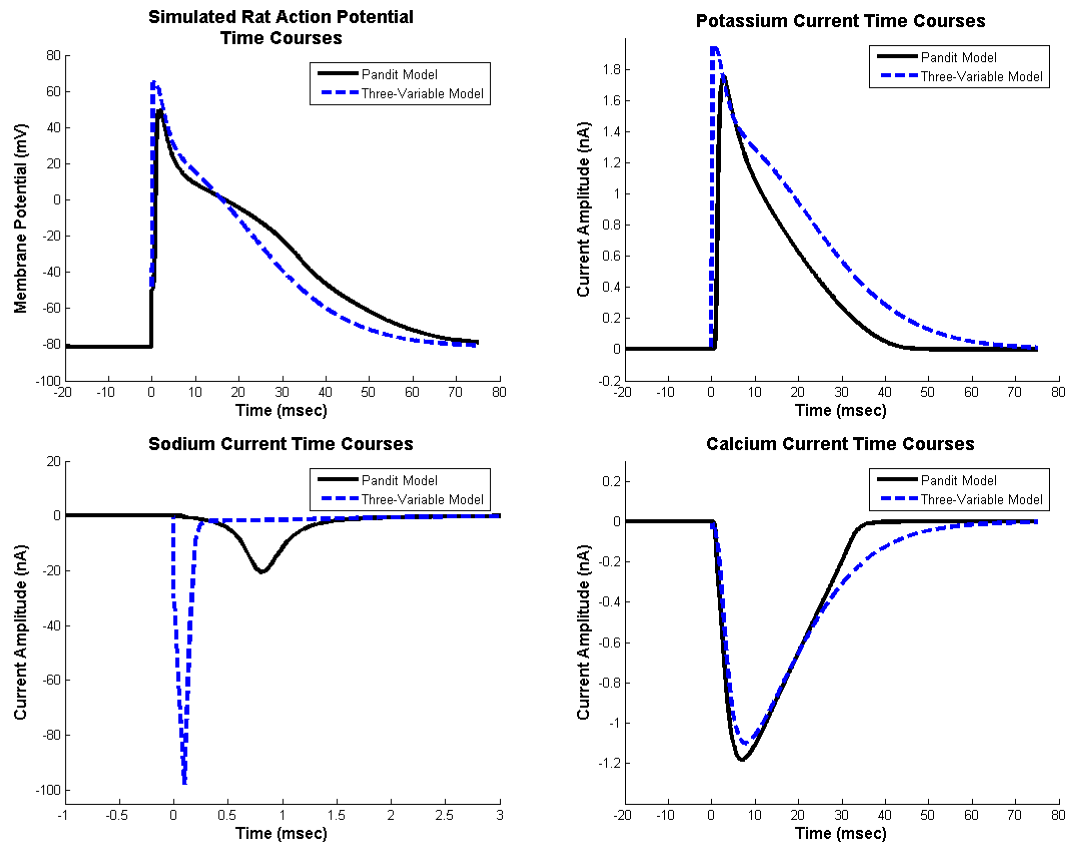


Figure 3.4: These plots illustrate that our initial estimates for the parameter values yield results that are quite consistent with those of the Pandit model. The action potential morphologies, calcium current time courses, and potassium current time courses are all similar in their peaks and proportions. The sodium current generated by the three-variable model, however, is larger than that generated by the Pandit model by a factor of about 4 or 5.

velocities of the action potentials should be similar. Third, the peak sodium currents and peak calcium currents should be similar. Fourth, the maximum upstroke velocity of the two action potentials should be similar. Fifth, the overall shape of the action potentials should be similar.

To ensure that these key characteristics are shared by both models let us begin by identifying a subset of  $q_1, q_2, \dots, q_N$  such that each set of parameter values in this subset yields results satisfying the following four constraints:

$$\frac{\left| \max_t V_m - \max_t \bar{v} \right|}{\max_t V_m - \min_t V_m} < \varepsilon \quad (3.23)$$

$$\frac{\left| \max_t \frac{dV_m}{dt} - \max_t \frac{d\bar{v}}{dt} \right|}{\max_t \frac{dV_m}{dt}} < 2\varepsilon \quad (3.24)$$

$$\frac{\left| \max_t |I_{Na}^P| - \max_t |I_{Na}^{TV}| \right|}{\max_t |I_{Na}^P|} < 5\varepsilon \quad (3.25)$$

$$\frac{\left| \max_t |I_{Ca}^P| - \max_t |I_{Ca}^{TV}| \right|}{\max_t |I_{Ca}^P|} < 5\varepsilon \quad (3.26)$$

for a given  $\varepsilon$  where  $I_S^{TV}$  and  $I_S^P$  are the currents associated with ion species  $S$  for the three-variable and Pandit models, respectively. Call this subset the admissible set of parameter values and denote it  $q_1^*, q_2^*, \dots, q_{N^*}^*$ . Then let us choose as our energy function for the deviation between the outputs of each model, the sum of the absolute values of the differences between the membrane potential at each time step. In other words, if  $t_1, t_2, \dots, t_M$  is a discretization of time and  $\bar{v}_{j,i}$  is the membrane potential in the three-variable model at time  $t_j$  when

parameter set  $q_i^*$  is used and  $V_{m,j}$  is membrane potential in the Pandit model at time  $t_j$ . Then the energy function is

$$E_i = \sum_{j=1}^M |\bar{v}_{j,i} - V_{m,j}| \quad (3.27)$$

We seek the 7-tuple  $q_k^*$  in the admissible set such that  $E_k \leq E_i$  for all  $i = 0, 1, 2, \dots, N^*$ , and the hope is that such a set of parameter values provides a good candidate for the optimal set of parameter values. Of course, there is no reason, beyond heuristics, to assume that the energy function (3.27) provides the best measure of the difference between the two models, nor is there any guarantee that the point  $q_k^*$  identifies the global minimum of the energy function. One could define an energy function which measured the variation between the individual ion currents in each model as well, but this would necessitate a method for determining how to weight the variation in each characteristic. An inspection of the results achieved by calculating parameter values with my energy function makes a convincing argument that such a parameter set leads to a model which captures the relevant characteristics of the Pandit model with sufficient accuracy. Using this Monte Carlo method approach with  $N = 80000$  and  $\varepsilon = 0.015$  generates the set of “optimized” parameter values shown in Table 3.1.

### 3.3.3 Comparison with the Pandit Model

While significantly simpler than the Pandit model, the three-variable model using the parameter values in Table 3.1 still preserves the morphology

Parameter	Value	Meaning
$\kappa$	N/A	Variable, dimensionless parameter related to the number of open caveolae
$\overline{\tau_{Na}}$	0.2817	Time constant for the sodium current (in $sec/\mu F$ )
$\overline{\tau_{Ca}}$	21	Time constant for the calcium current (in $sec/\mu F$ )
$\overline{\tau_K}$	71	Time constant for the potassium current (in $sec/\mu F$ )
$\overline{\tau_{hc}}$	0.000342	Time constant for the closing of the $\bar{h}$ -gate (in sec)
$\overline{\tau_{ho}}$	1000	Time constant for the opening of the $\bar{h}$ -gate (in sec)
$v_h$	0.036	Threshold voltage at which $\bar{h}$ -gate changes direction (in units of $v$ )
$\overline{\tau_{pc}}$	0.0118	Time constant for the closing of the $\bar{p}$ -gate (in sec)
$\overline{\tau_{po}}$	0.00063	Time constant for the opening of the $\bar{p}$ -gate (in sec)
$v_p$	0.689	Threshold voltage at which $\bar{p}$ -gate changes direction (in units of $v$ )

Table 3.1: Optimized parameter values for the physiologically scaled three-variable model.

of the rat action potential and reproduces the ionic currents seen in the Pandit model quite well. The resulting action potential and sodium, potassium, and calcium currents for each model are shown superimposed upon one another in Figure 3.5. As mentioned earlier, sodium activation in the three-variable model reacts instantaneously to changes in membrane potential. This means that even under an instantaneous depolarizing pulse that lifts the membrane potential above threshold, the Pandit model will exhibit a delay in sodium activation that is absent in the three-variable model. This complicates the comparison of the action potential time courses generated by each of these models. Given the same instantaneous depolarizing stimulus, the action potentials will necessarily be out of phase by the length of the delay in the Pandit model. Thus, for the purposes of determining whether the three-variable model accurately reproduces results generated by the Pandit model, I apply the stimulus in the three-variable model 0.6 msec after it is applied in the Pandit model so that the upstroke of the action potentials are synchronized. I am therefore comparing not the time courses per se, but rather the waveforms generated by the two models.

Figure 3.5 illustrates the fact that for appropriately chosen parameter values, the three-variable model can generate an action potential that is nearly indistinguishable from that produced by the Pandit model while retaining a simplicity that allows for far more rigorous mathematical analysis. Now with this simplified model of rat cardiac action potential, I begin an investigation

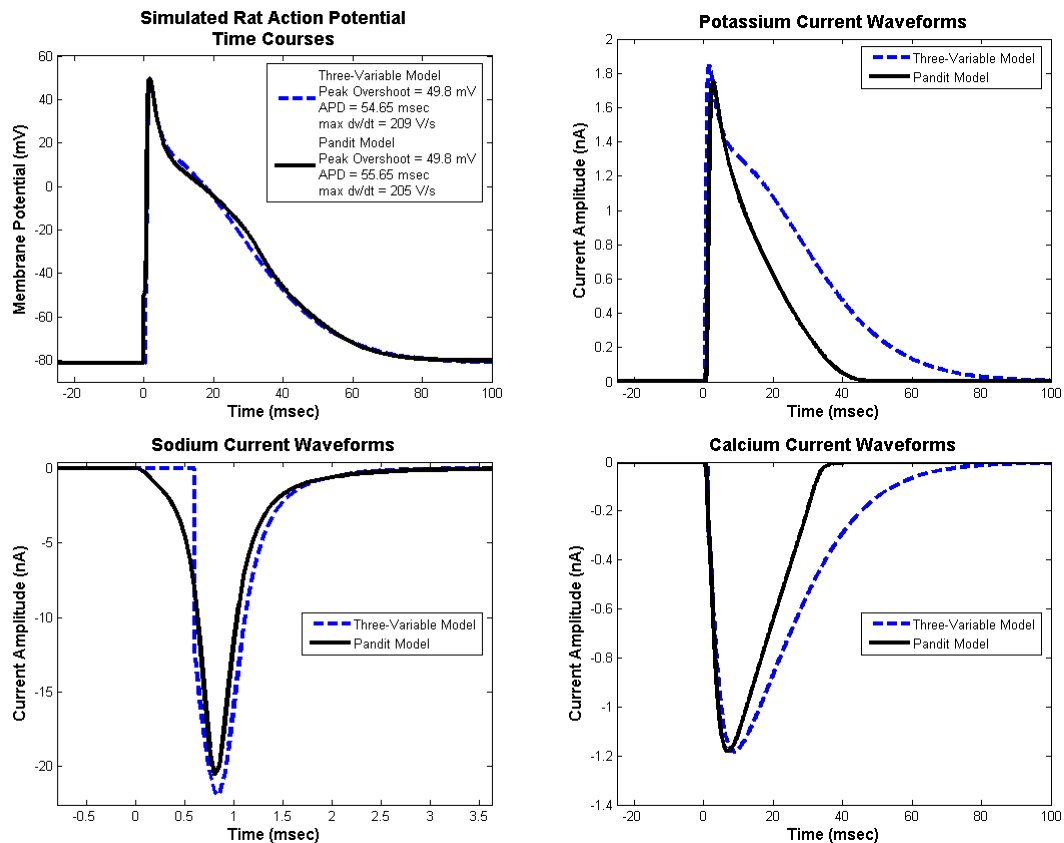


Figure 3.5: With parameter values optimized using the method explained in the text the three-variable model can generate an action potential morphology that is nearly identical to that produced by the Pandit model. Additionally, the underlying sodium, potassium, and calcium currents exhibit nearly identical morphologies between the two models. The only differences between these results are the 0.6 msec delay in action potential initiation in the three-variable model (discussed in the text) and the slightly slower decay to extinction of the potassium and calcium currents in the three-variable model. In other important respects such as peak voltage overshoot, action potential duration, and maximum upstroke velocity, there is good agreement between the models.

of the effects of caveolar sodium currents on the three-variable model action potential and compare the results with those generated by the Pandit model.

### 3.4 Simulation Protocols

As with the Pandit model, there are two things I wish to test with this model - whether it can replicate the electrophysiological data related to the PKA-independent  $\beta$ -adrenergic response that have been shown experimentally, and if so, what effects these additional sodium currents have on action potential morphology. Of particular interest are the effects on quantities such as maximum upstroke velocity, maximum overshoot, and action potential duration (APD). To do this, consider the three-variable model simulation shown in Figure 3.5 to be baseline, just as was done in the previous chapter, and compare these results with those generated when we augment the normal sodium current with caveolar sodium current. Note that in the caveolar-inclusive model, whole-cell sodium conductance is given by  $(\overline{g_{Na}} + n\gamma_{Na})$  and  $n$  is varied from 0 to 25000 to simulate differing degrees of  $\beta$ -adrenergic stimulation. This results in increases to whole-cell sodium conductance of up to approximately 42%. To simulate the same increases in sodium conductance in the three-variable model,  $\kappa$  is varied from 1 to 1.42.

#### 3.4.1 Voltage-Clamp Protocol

I conduct the same computational voltage-clamp experiments as I did in the previous chapter. Whole-cell  $I_{Na}$  is elicited from cells conditioned at a hold-

ing potential of -100 mV before clamping the cell at test potentials between -80 and +50 mV in 5 mV increments. These voltage clamp experiments are done first using  $\kappa = 1$  to simulate no open caveolae and then the experiments are conducted using a range of  $\kappa$ -values between 1 and 1.42 and the results are compared to baseline. As with the corresponding laboratory experiments, I report the results in the form of I-V curves. Since the three-variable model does not account for changes in ion concentrations, I simulate the lower extracellular sodium concentrations present in the experiments by Lu et al[1] by changing the Nernst potential for sodium from 66 mV to 18 mV and reducing the whole-cell sodium conductance. It was assumed in the previous chapter that single-channel sodium conductance changes from 18 pS under physiological sodium concentrations to approximately 2.2 pS under the low extracellular sodium concentrations at which the relevant experiments were conducted. So, for the purposes of the voltage-clamp the time constant associated with the sodium current is multiplied by  $18^{1/2.2}$ .

### 3.4.2 Action Potential Protocols

To elicit action potentials with the three-variable model, I use the instantaneous voltage jump protocol as was used earlier in this chapter to compare the Pandit and three-variable models instead of the transient injection of a depolarizing current as was employed by Pandit et al[17] in their study. A transient depolarizing stimulus is not applied because the sodium activation

in the three-variable model reacts instantaneously to changes in membrane potential and even a brief 5 msec depolarizing stimulus of 0.6 nA will overlap substantially with the upstroke of the action potential making it impossible to determine the extent to which changes in caveolar sodium current effect action potential morphology.

As in the Pandit model, an increase in sodium current, in the absence of changes in other ionic currents, must cause an increase in the rate at which membrane voltage changes. I quantify this change by plotting maximum upstroke velocity of the action potential as a function of the number of open caveolae which in the case of the three-variable model is equivalent to varying the value of  $\kappa$  from 1 to 1.42. Action potentials are elicited with  $\kappa$ -values that are increased in increments of 0.01. The maximum upstroke velocity in each trial is recorded after each trial and these velocities are then plotting against  $\kappa$ . APD in each trial is also recorded and these too are plotted against  $\kappa$  to expose any dependence that might exist.

### 3.5 Results

The following simulations provide insight into how an increase in sodium current affects action potential morphology and in particular, how the upstroke velocity of the action potential depends upon the amount of extra sodium current in the three-variable model. I compare these results with the results generated using the caveolae-inclusive model in order to ensure that this simpli-

fied model still yields results that are consistent with a more physiologically detailed model.

### 3.5.1 Replication of Experimental Data

Let us first examine the sodium current-voltage curves that the three-variable model generates with and without the inclusion of open caveolae. As in the previous chapter, I assume that a 100 pF cell contains between 20000 and 25000 caveolae that can be opened via  $\beta$ -adrenergic stimulation. Figure 3.6 shows the resulting current-voltage curves alongside those produced by the caveolae-inclusive model for comparison. By construction this model produces the same approximately 34% and 42% increases in maximum peak sodium current for 20000 and 25000 caveolae, respectively, that were seen using the caveolae-inclusive model and the same sodium Nernst potential. The differences between the two models, however, lead to noticeable differences between the two sets of curves. The caveolae-inclusive model exhibits a steep peak  $I_{Na}$  dependence upon membrane potential between -50 mV and -35 mV reaching a maximum peak current amplitude near -30 mV. While the three-variable model exhibits a much more gradual increase in peak current amplitude reaching its maximum amplitude near -15 mV. Beyond about -5 mV it then exhibits a much steeper dependence upon membrane potential. The maximum peak  $I_{Na}$  in the three-variable model is also about  $2/3$  that of the caveolae-inclusive model.

These differences are likely due to the differences in sodium gating be-

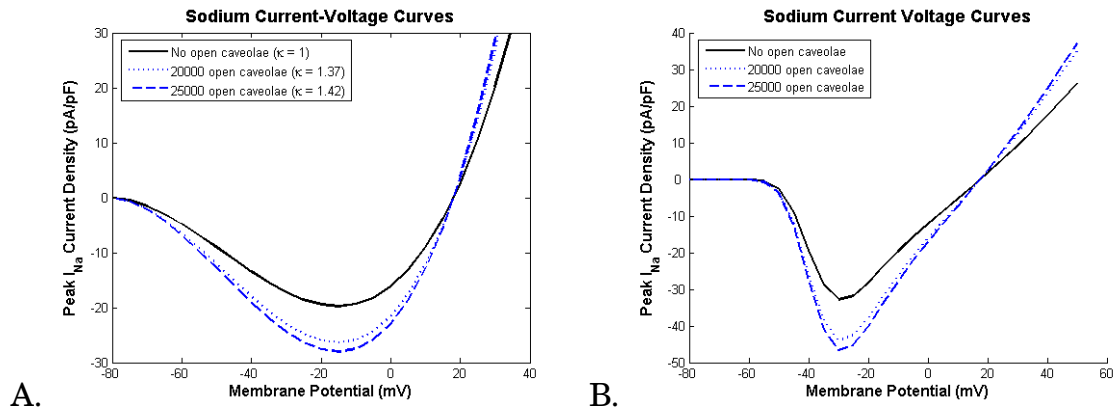


Figure 3.6: This figure illustrates the effects that caveolar sodium current has on sodium current-voltage curves in the three-variable model (A) and compares them to the corresponding changes seen in the caveolae-inclusive model (B). The solid black curves depicts baseline sodium current response to the voltage-clamp protocol, while the blue curves depict the augmented response due to caveolae which have opened to present the sarcolemma with additional sodium channels. In the case of the three-variable model, the dotted and dashed blue curves were generated by selecting  $\kappa = 1.37$  and  $\kappa = 1.42$ , respectively. These choices of  $\kappa$  correspond to the inclusion of 20000 and 25000 open caveolae on the cell's sarcolemma and result in the desired 34% and 42% increases to maximum peak sodium current that were seen with the caveolae-inclusive model.

tween the two models. Recall that the caveolae-inclusive model uses the Hodgkin-Huxley formalism in the formulation of the ionic currents while the three-variable model has a much simpler inactivation mechanism and an activation mechanism that does not exhibit any delay relative to changes in membrane potential. As a consequence, one would expect the sodium current in the three-variable model to be non-negligible at potentials only slightly above rest. In contrast, the lack of sodium activation that occurs at these membrane potentials in the caveolae-inclusive model results in only a small amount of sodium current before inactivation dominates. Despite these differences, the overall shape of the current-voltage curves are quite similar, so it is likely that the changes in action potential morphology caused by caveolar sodium current in the three-variable model will mimic the changes seen with the more physiologically detailed model. These changes are investigated in the next section.

### 3.5.2 Caveolar Effects on Action Potential

The effects of caveolar sodium current on the action potential morphology in the three-variable model are similar to those in the caveolae-inclusive model. Caveolar sodium current increases maximum upstroke velocity and peak overshoot, but has little effect on morphology after the peak voltage is reached. Figure 3.7 summarizes the effects that the inclusion of 25000 caveolae per cell have on action potential morphology in the three-variable model.

The most noticeable effect of caveolar sodium current is an increase in

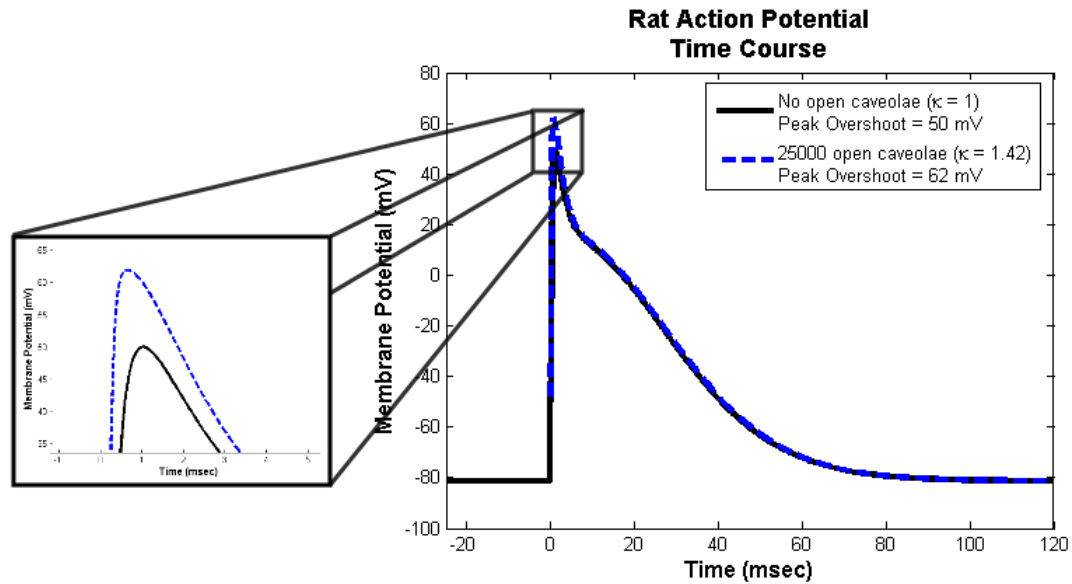


Figure 3.7: Action potential morphology using the three-variable model with and without caveolar sodium current.

peak voltage from approximately 50 mV to 62 mV, a 9% increase in overall height of the action potential (Recall that there was similar increase of approximately 5% in peak overshoot in the caveolae-inclusive model). As with the caveolae-inclusive model, the effects on maximum upstroke velocity are less apparent, so the relationship between caveolar sodium current and maximum upstroke velocity are illustrated in Figure 3.8.A. Note that in agreement with the caveolae-inclusive model and other studies[24, 26, 25, 27], there exists a nearly linear relationship between maximum upstroke velocity and percent increase to sodium current (regulated by changing  $\kappa$  in this case). Action potential duration on the other hand exhibits little dependence upon percent increase to sodium current.

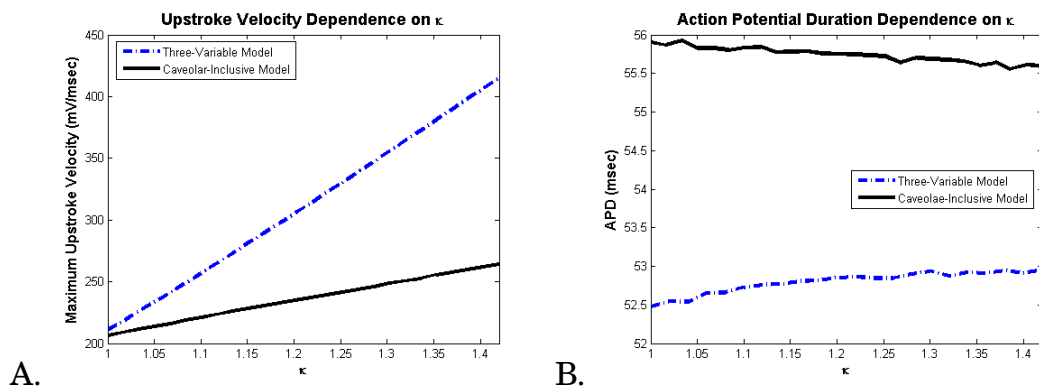


Figure 3.8: The relationships between upstroke velocity and  $\kappa$  and between action potential duration and  $\kappa$  in the three-variable model exhibit similarities with the corresponding relationships seen using the caveolae-inclusive model. A. Maximum upstroke velocity exhibits a nearly linear dependence upon  $\kappa$  just as seen with the caveolae-inclusive model. However, the same proportional increase in sodium current in the three-variable model results in a much greater increase in maximum upstroke velocity than in the caveolar-inclusive model. In the case of the maximum upstroke velocity, there exists a strong positive relationship. An increase of 0.0168 to  $\kappa$  is equivalent to the addition of 1000 open caveolae in the caveolae-inclusive model. Such an increase to  $\kappa$  in the three-variable model yields a 3.6% increase to maximum upstroke velocity from baseline. This is a substantially greater rate of increase than the corresponding 1.2% increase seen with the caveolae-inclusive model. B. As with the caveolae-inclusive model, APD is relatively unaffected by increases in sodium current in the three-variable model. In the three-variable model APD as a function of  $\kappa$  exhibits a slight upward trend with the addition of 25000 caveolae (i.e.  $\kappa = 1.42$ ) leading to only a 1% increase in APD.

These results suggest that the dominant relationship between sodium current and maximum upstroke velocity is linear, so as in the previous chapter, I wish to derive that linear relationship directly from the model equations.

### 3.6 Asymptotic Analysis

In this section I conduct an asymptotic analysis in order to extract this linear relationship directly from the three-variable model. For simplicity, I shall conduct this analysis on the normalized version of the model and then translate the results into the scale used in the non-normalized version so that meaningful comparisons can be made. Critical to this analysis is the observation that because of the way in which calcium activation is designed in this model, the maximum upstroke velocity occurs prior to activation of the calcium current. This means that the initial upstroke of the action potential is overwhelmingly determined by the interplay between sodium and potassium, so for the purposes of analyzing the action potential upstroke, the model reduces to the system

$$\begin{aligned}\frac{dv}{dt} &= \frac{\kappa hv^2(1-v)}{\tau_{Na}} - \frac{v}{\tau_K} \\ \frac{dh}{dt} &= \frac{-h}{\tau_{hc}}\end{aligned}\tag{3.28}$$

for times shortly after the initial stimulus. Where  $v = \frac{\bar{v} + 81.36}{147.36}$ ,  $\tau_{hc} = \frac{\bar{\tau}_{hc}}{0.68}$ ,  $\tau_{Na} = \frac{C_m \bar{\tau}_{Na}}{0.68}$ ,  $\tau_K = C_m \bar{\tau}_K$ . For simplicity, let  $a = \frac{\kappa}{\tau_{Na}}$ ,  $b = \frac{1}{\tau_{hc}}$ , and  $c = \frac{1}{\tau_K}$ . Then

$$\begin{aligned}\frac{dv}{dt} &= ahv^2(1-v) - cv \\ \frac{dh}{dt} &= -bh\end{aligned}\tag{3.29}$$

Note that with  $C_m = 10^{-4} \mu\text{F}$ , and the optimized parameter values  $\overline{\tau_{hc}} = 0.000342$ ,  $\overline{\tau_{Na}} = 0.2817$ , and  $\overline{\tau_K} = 71$ , the parameter values in this normalized version become  $\tau_{hc} \approx .000503$ ,  $\tau_{Na} \approx 0.00004$ , and  $\tau_K \approx 0.0071$  yielding  $a \approx 25000\kappa$ ,  $b \approx 2000$ ,  $c \approx 141$ . This means that even, though,  $c \ll b \ll a$ ,  $\frac{dh}{dt}$  is certainly not close to zero initially and suggests that changes in  $h$  cannot be neglected.

Differentiation of (3.29) yields,

$$\begin{aligned}
\frac{d^2v}{dt^2} &= 2ahv\frac{dv}{dt} + av^2\frac{dh}{dt} - 3ahv^2\frac{dv}{dt} - av^3\frac{dh}{dt} - c\frac{dv}{dt} \\
&= 2ahv\frac{dv}{dt} - abhv^2 - 3ahv^2\frac{dv}{dt} + abhv^3 - c\frac{dv}{dt} \\
&= (2ahv - 3ahv^2 - c)\frac{dv}{dt} - abh(v^2 - v^3) \\
&= (2ahv - 3ahv^2 - c)(ah(v^2 - v^3) - cv) - abh(v^2 - v^3) \\
&= 2a^2h^2v(v^2 - v^3) - 3a^2h^2v^2(v^2 - v^3) - ach(v^2 - v^3) \dots \\
&\quad - 2achv^2 + 3achv^3 + c^2v - abh(v^2 - v^3)
\end{aligned} \tag{3.30}$$

Obviously, solving  $\frac{d^2v}{dt^2} = 0$  presents some challenges, so as a first approximation, let us simplify the right hand side of (3.30) by applying  $c \ll b \ll a$  and eliminating the terms which contain  $c$  or  $b$ . As already mentioned, this will likely lead to errors since doing so is tantamount to assuming that the potassium current also plays no role in the upstroke of the action potential and that the maximum upstroke velocity is reached before  $h$  has had a chance to change appreciably. That is, doing so assumes that the upstroke of the action potential can be modeled by the single differential equation

$$\frac{dv}{dt} = ahv^2(1 - v) \tag{3.31}$$

where  $h = h_0 = 1$ . This reduces (3.30) to

$$\begin{aligned}
\frac{d^2v}{dt^2} &= 2a^2h^2v(v^2 - v^3) - 3a^2h^2v^2(v^2 - v^3) \\
&= a^2h^2v(v^2 - v^3)(2 - 3v)
\end{aligned} \tag{3.32}$$

The only zeros, denoted  $v^*$ , of the right hand side of (3.32) are  $v^* = 0$ ,  $v^* = 1$ , and  $v^* = 2/3$ , because  $a \neq 0$  and  $h \neq 0$ . Since  $\left. \frac{dv}{dt} \right|_{v^*=0} = \left. \frac{dv}{dt} \right|_{v^*=1} = 0$ , and  $\frac{dv}{dt} > 0$  for  $v \in (0, 1)$ , we may conclude that the maximum upstroke velocity occurs at  $v^* = 2/3$ . Conversion back into the physiological scale yields  $\bar{v}^* = \left(\frac{2}{3}\right) 147.36 - 81.36 = 16.9$  mV and an approximate maximum upstroke velocity of

$$\begin{aligned} \left. \frac{dv}{dt} \right|_{\bar{v}^*=16.9} &= - \left( \frac{1}{C_m} \right) \left( \frac{\kappa (0.68) \left( \frac{16.9 + 81.36}{147.36} \right)^2 (16.9 - 66)}{\bar{\tau}_{Na}} \right) mV/sec \\ &= 526980 \kappa mV/sec \\ &\approx 527 \kappa mV/msec \end{aligned} \quad (3.33)$$

Obviously, since  $\kappa = 1$  in the three-variable model yields a maximum upstroke velocity of approximately  $210 mV/msec$ , this method of estimation is highly inaccurate and illustrates that, as expected, neglecting the change in  $h$ -value (and perhaps also the contribution of potassium) is not appropriate.

Let us continue to neglect the potassium current, but account for the inactivation of sodium current. During the upstroke, the membrane potential is above  $v_h$  so  $h(t) = e^{-t/\tau_{hc}}$  can be substituted into (3.31) yielding the separable differential equation

$$\frac{dv}{dt} = a e^{-bt} v^2 (1 - v) \quad (3.34)$$

that can be solved using the method of partial fractions as follows

$$\begin{aligned}
& \frac{1}{v^2(1-v)}dv = ae^{-bt}dt \\
\Rightarrow & \int_{v_0}^v \frac{1}{\nu^2(1-\nu)}d\nu = \int_0^t ae^{-bs}ds \\
\Rightarrow & \int_{v_0}^v \frac{\nu+1}{\nu^2}d\nu + \int_{v_0}^v \frac{1}{1-\nu}d\nu = a \int_0^t e^{-bs}ds \\
\Rightarrow & \int_{v_0}^v \frac{1}{\nu}d\nu + \int_{v_0}^v \frac{1}{\nu^2}d\nu + \int_{v_0}^v \frac{1}{1-\nu}d\nu = -\frac{a}{b}e^{-bt} + \frac{a}{b} \\
\Rightarrow & \ln v - \ln v_0 - \frac{1}{v} + \frac{1}{v_0} - \ln(1-v) + \ln(1-v_0) = -\frac{a}{b}e^{-bt} + \frac{a}{b} \\
\Rightarrow & \ln \frac{v}{v_0} - \frac{1}{v} + \frac{1}{v_0} + \ln \frac{(1-v_0)}{(1-v)} = -\frac{a}{b}e^{-bt} + \frac{a}{b} \\
\Rightarrow & \frac{1}{v_0} - \frac{1}{v} + \ln \frac{v(1-v_0)}{v_0(1-v)} = -\frac{a}{b}e^{-bt} + \frac{a}{b} \\
\Rightarrow & a - b \left( \frac{1}{v_0} - \frac{1}{v} + \ln \frac{v(1-v_0)}{v_0(1-v)} \right) = ae^{-bt}
\end{aligned} \tag{3.35}$$

Thus equation (3.34) can be rewritten as

$$\frac{dv}{dt} = \left( a - b \left( \frac{1}{v_0} - \frac{1}{v} + \ln \frac{v(1-v_0)}{v_0(1-v)} \right) \right) v^2(1-v) \tag{3.36}$$

Under conversion back into the physiological scale this becomes

$$\frac{d\bar{v}}{dt} = - \left( \frac{1}{C_m} \right) \left( \frac{0.68\kappa}{\bar{\tau}_{Na}} - \frac{C_m}{\bar{\tau}_{Kc}} \left( \frac{147.36}{\bar{v}_0 + 81.36} - \frac{147.36}{\bar{v} + 81.36} + \ln \frac{(\bar{v} + 81.36)(66 - \bar{v}_0)}{(\bar{v}_0 + 81.36)(66 - \bar{v})} \right) \right) \left( \frac{\bar{v} + 81.36}{147.36} \right)^2 (\bar{v} - 66) \tag{3.37}$$

Assuming  $\bar{v}^* \approx 16.9$  mV still provides a reasonable approximation for the voltage at which the maximum upstroke velocity occurs, and assuming  $v_0 = -50$  mV, the approximate maximum upstroke velocity as a function of  $\kappa$  is given by

$$\begin{aligned}
\left. \frac{dv}{dt} \right|_{\bar{v}^*=16.9} &= - \left( \frac{1}{C_m} \right) \left( \frac{0.68\kappa}{\bar{\tau}_{Na}} - \frac{C_m}{\bar{\tau}_{Kc}} \left( \frac{147.36}{-50 + 81.36} - \frac{147.36}{16.9 + 81.36} + \ln \frac{(16.9 + 81.36)(66 + 50)}{(-50 + 81.36)(66 - 16.9)} \right) \right) \\
& \quad \left( \frac{16.9 + 81.36}{147.36} \right)^2 (16.9 - 66) \text{ mV/sec} \\
&= 526980\kappa - 332000 \text{ mV/sec} \\
&= 527\kappa - 332 \text{ mV/msec}
\end{aligned} \tag{3.38}$$

Superimposing this line on the graph of the numerically generated relationship between maximum upstroke velocity and  $\kappa$ -value produces the plot in Figure

3.9.

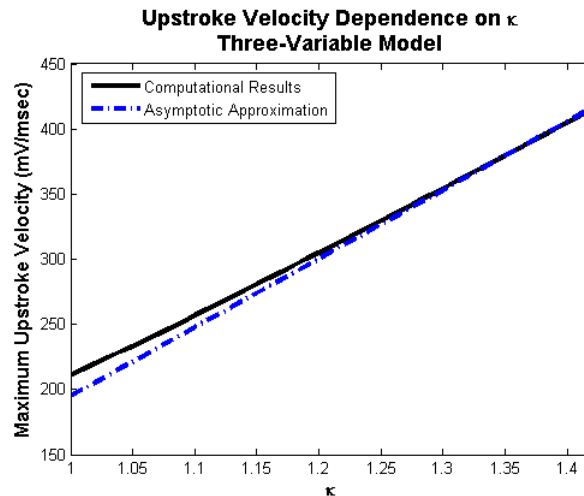


Figure 3.9: The computationally derived relationship between maximum upstroke velocity and  $\kappa$ -value shown along with the analytically extracted linear relationship between maximum upstroke velocity and  $\kappa$ -value. Notice that there is very close agreement between the two graphs suggesting that the dominant relationship between upstroke velocity and caveolar sodium current is, in fact, linear.

### 3.7 Conclusions

While a high degree of physiological detail in a mathematical model produces numerical results that are very accurate, these gains in accuracy must be weighed against their computational expense and analytical intractability. What has been presented in this chapter is a much simpler model that succeeds in capturing the general morphology of the rat action potential and the morphologies of the underlying ionic currents using a system of only three differential equations as opposed to the 26 differential equations used in the Pandit model[17].

Admittedly, this simplified model does exhibit some departures from physiological accuracy. The shapes of the sodium I-V curves with this three-variable model for instance are somewhat inaccurate, and the upstroke velocity of the action potential with this model appears to exhibit a much stronger dependence upon caveolar sodium current than does the more physiologically detailed caveolae-inclusive model. Nevertheless, much of the relevant response to caveolar sodium current is still captured and it is this model's simplicity that allows us to analytically extract the linear relationship between maximum upstroke velocity and the amount of caveolar sodium current, something that proved impossible using the caveolae-inclusive model.

The main difference between this model and the caveolae-inclusive model is the absence of a separate sodium activation variable in the three-variable model with the requisite delayed response to changes in membrane potential.

This leads to more rapid activation than occurs in reality and is likely the reason for the inaccuracies in the sodium I-V curves and the response of the upstroke velocity to changes in caveolar sodium current. In future refinements of this model, a major goal will be the inclusion of an activation gating mechanism which is more physiologically accurate, but which does not significantly impact the model complexity so that similar analyses can still be carried out.

## CHAPTER 4 STOCHASTIC CAVEOLAE MODEL

### 4.1 Introduction to the Stochastic Caveolae Model

Thus far, this project has focused exclusively on the normal functioning of caveolae and their effects on current modulation in healthy cells. I now explore a possible arrhythmogenic role for caveolae. Recall that caveolae open as a result of an interaction between  $G_s\alpha$ , released upon  $\beta$ -adrenergic stimulation, and caveolin-3, the primary scaffolding protein in caveolae. How this interaction causes opening of the caveolar neck and the manner in which the opening occurs are still open questions, but it is known that the interaction between  $G_s\alpha$  and caveolin-3 that facilitates opening occurs at a single  $G_s\alpha$  amino acid (41histidine)[2].

However, it appears that caveolin-3 dysfunction plays a role in the development of disease and arrhythmias. Mutations in *CAV3*, the gene responsible for the expression of caveolin-3, are known to be associated with a variety of pathologies including muscular dystrophy[37, 38, 39], hyperCKemia[37], myopathy[37, 39, 40, 41], sudden infant death syndrome[42], arrhythmias in acquired heart disease (e.g. hypertrophy and myocardial infarction)[43], and Long QT Syndrome[3]. In this chapter, I shall focus on links between caveolin-3 and the last of these, Long-QT Syndrome (LQTS).

In 2006, Vatta et al[3] demonstrated links between mutant caveolin-3

and a certain type of LQTS, a condition that collectively refers to any of a number of genetically distinct arrhythmogenic pathologies affecting cardiac myocyte repolarization. Their study showed, human ventricular myocytes, like those of rat, also exhibit colocalization of caveolin-3 and  $\text{Na}_v1.5$  sodium channels to caveolae, and that expression of certain types of mutant caveolin-3 correlates with the incidence of LQT3-like symptoms in patients and the presence of a late, persistent sodium current in cells expressing these mutant proteins. While the specific processes by which the mutations cause this unique type of LQTS (denoted LQT9) are yet unknown, these findings provide additional evidence that that caveolae play a critical role in cardiac electrodynamics and that caveolae-associated pathologies can contribute to arrhythmogenesis.

Here I use a new mathematical model of caveolar dynamics to propose a hypothesis for the underlying cause of this link between mutant caveolin-3 and LQT9. Given that caveolin-3 is known to be critically involved in the opening and closing of caveolae, I hypothesize that the caveolin-3 mutation alters caveolar opening dynamics. The aim in this investigation is to test the hypothesis that abnormal caveolar opening dynamics offers a plausible link between mutant caveolin-3 and persistent sodium current in LQT9.

In this study, I demonstrate that stochastic opening of a cardiomyocyte's caveolae produces a late, persistent sodium current similar to that measured experimentally in caveolin-3 mutant cells[3]. Furthermore, action potential simulations with this stochastic caveolae model exhibit a substantial delay in

repolarization and early afterdepolarizations (EADs), two hallmarks of LQTS. I conclude that mutant caveolin-3-induced caveolar stochasticity offers a plausible explanation for the mechanism by which caveolin-3 mutation can cause LQTS. I also seek to provide motivation for additional experimental investigations into caveolae function and into possible caveolae-related arrhythmogenic mechanisms.

## **4.2 Mathematical Modeling**

### **4.2.1 Conceptual Foundations**

In order to understand the contribution of caveolae to whole-cell current one must first understand the behavior of a single caveolae in both its open and closed states. As with the caveolae-inclusive model and the three-variable model, it is assumed in this model that each closed caveolae contains exactly one sodium channel and that the transitions between a caveolae's open and closed states occur rapidly enough to be neglected. Also, since it is well established experimentally that sodium channels residing in closed caveolae are electrically isolated from the extracellular environment[21], a caveolae which closes at rest will render the sodium channel it sequesters fixed in its closed state for as long as the caveolae remains closed. Consider for instance a single stochastically opening caveolae and the sodium channel it sequesters. Note that at resting membrane potentials there is an overwhelming probability that a sodium channel on the sarcolemma will be in its closed state. So, when the

cell membrane is at rest, the caveolar membrane potential will equilibrate to this steady-state value and no opening or closing will change its state or the state of the sequestered sodium channel.

If this caveolae is in its open state upon arrival of the depolarizing stimulus, then the sequestered sodium channel will merely respond like any other sodium channel on the sarcolemma. It will open, conduct, inactivate, and remain in its inactive state until the caveolar membrane potential has returned to the resting membrane potential long enough for the channel to recover from inactivation. If on the other hand, the caveolae is closed upon the arrival of the depolarizing stimulus, the sodium channel will remain in its closed state. This is because current can neither flow through the caveolar neck nor through the closed sodium channel in the caveolar membrane, so no change to caveolar membrane potential can occur. It is only if this caveolae opens later in the action potential, when the sarcolemma is still sufficiently depolarized, that its sodium channel will open, conduct, and inactivate.

In both of these cases, however, if the caveolae subsequently closes while the caveolar membrane is still depolarized, the sodium channel will remain fixed in its inactive state. This means that any subsequent openings prior to the repolarization of the myocyte will yield no further sodium current. Therefore, any accounting of caveolar sodium contribution need only consider the distribution of caveolar first openings throughout the action potential.

The whole-cell caveolar sodium current at any given time is then the

sum of all the sodium currents through each of the caveolae which are open at that time. However, unlike whole-cell currents treated in the manner of Hodgkin and Huxley, the time courses of currents through sodium channels sequestered by different caveolae will be different depending upon the time course taken by the sarcolemmal potential while different caveolae are open. In other words,  $m^3(t^*)h(t^*)j(t^*)$  does not represent the proportion of caveolar sodium channels which are in their open state at time  $t^*$  as is the case with sarcolemmal sodium channels which all react as a set of identical channels. Rather, caveolar sodium channels can be grouped into sets of identical channels only if they are sequestered by caveolae which open at the same time after the stimulus. Sodium channels embedded in caveolae which have very recently opened will be in the early stages of activation, while sodium channels embedded in caveolae which have been open for a relatively long time will have begun entering their inactive state. Therefore, in a model of stochastic caveolae, the time courses of the gating variables are dependent upon both the time from stimulus and the time from caveolar opening. We shall see that this leads to a partial differential equation formulation for the sodium gating variables.

## 4.2.2 Caveolar Opening as a Poisson Process

### 4.2.2.1 The Poisson Random Variable

Consider an event that recurs randomly in time. We say that the events occur in accordance with a Poisson process having rate  $\lambda$ , if the occurrences

satisfy the following three assumptions:

1. The probability of exactly one event occurring in the interval  $[t, t + \Delta t]$  is  $\lambda\Delta t + o(\Delta t)$ ;
2. The probability of two or more events occurring in the interval  $[t, \Delta t]$  is  $o(\Delta t)$ ; and
3. Events that occur in any two non-overlapping intervals are independent of one another.

In such a scenario,  $\lambda$  represents the expected number of events in an interval one unit of time in length[44]. In the absence of any experimental data regarding the opening dynamics of caveolae expressing mutant caveolin-3, the assumption that they open stochastically according to a Poisson process seems reasonable and appropriately simple. Then supposing that a single caveolae is expected to experience an average of  $\lambda$  opening events in any given unit interval of time, we derive the probability density function of caveolar first openings as follows.

#### 4.2.2.2 First Opening Probability Density Function

Any accounting of caveolar sodium contribution need only consider the distribution of caveolar first openings throughout the action potential. Assuming that the opening events of a single caveolae occur according to a Poisson process, if we let  $N(t)$  represent the number of times a caveolae experiences an

opening event in a time interval of length  $t$ , then probability of such an event happening  $k$  times (the event denoted  $N(t) = k$ ) is given by

$$P(N(t) = k) = e^{-\lambda t} \frac{(\lambda t)^k}{k!} \quad (4.1)$$

Now let  $X$  denote the time from stimulus until its first opening event occurs.

Then, we have

$$P(X > t) = P(N(t) = 0) = e^{-\lambda t} \quad (4.2)$$

Thus the cumulative distribution function for  $X$  is given by,

$$P(X \leq t) = P(N(t) \geq 1) = 1 - e^{-\lambda t} \quad (4.3)$$

Differentiating yields the associated probability density function of first openings of caveolae

$$\rho(t) = \lambda e^{-\lambda t} \quad (4.4)$$

The area under the curve  $\rho(t)$  between  $[t, t + \varepsilon]$  is the probability that a given caveolae opens for the first time between  $t$  and  $t + \varepsilon$  units of time after the stimulus. Furthermore, if the number of caveolae,  $n$ , is large, then

$$n\rho(t)\Delta t \quad (4.5)$$

provides a good approximation of the number of caveolae which experience a first opening in the interval  $[t, t + \Delta t]$  provide we select a  $\Delta t$  small enough. Since we estimate that a single cardiac cell contains approximately 20000-30000 caveolae, we can be assured of the validity of this approximation and can use this continuum density approach.

### 4.2.2.3 The Poisson Rate Parameter

Assuming that events occur according to a Poisson process, the probability of exactly one event occurring in the interval  $[t, t + \Delta t]$  is  $\lambda\Delta t + o(\Delta t)$ , so the Poisson rate parameter,  $\lambda$ , can be thought of as the expected average rate at which the events happen. In experimental studies, the value of the Poisson rate parameter,  $\lambda$ , is calculated empirically, but due to the theoretical nature of this investigation, we lack a means to reasonably estimate its value.

In the context of stochastically opening caveolae, a large  $\lambda$  means caveolae are expected to experience opening events with a relatively high frequency, while a small  $\lambda$  means a relatively low frequency. Alternatively, when considering the actions of many caveolae during an action potential as we do here, a large  $\lambda$  means that most of the caveolae open for the first time within a short time of the stimulus, while a small  $\lambda$  means that there are still many caveolae which have not yet opened for the first time late in the action potential.

It is important to note that  $\lambda$  gives no information about the rate at which caveolae close, an important concern when estimating the amount of current conducted through caveolae. To ensure that caveolae remain open long enough for their sodium channels to contribute fully, we must make an assumption about the relative scales of the kinetics involved. It has been well established by way of voltage clamp experiments that voltage-gated sodium channels in their closed conformation react very quickly to sufficient depolarization of the membrane. Inspection of sodium current time courses in these

experiments indicates that most sodium channels in a membrane patch open within the first 5 msec of the depolarizing step and have entered their inactive state by about 10 msec into the depolarizing step. Of course due to the stochastic nature of the individual channel gates, some react even quicker, some react slower, and some may not react at all. Furthermore, the time constants of these processes are also voltage dependent. Nevertheless, the proportion of channels which have not completed the cycle from closed to open to inactive within the first 10 msec of sensing most suprathreshold levels of depolarization is negligible. For this reason, let us assume that the kinetics of caveolae are substantially slower than the kinetics of the sodium channels they contain. Doing so means that caveolae can be expected remain open long enough for sodium inactivation to occur, so a caveolae's behavior after its first post-stimulus opening is of no consequence.

#### 4.2.3 Formulation of the Stochastic Caveolae Model

Due to the stochasticity in both caveolar opening dynamics and caveolar sodium channel kinetics, any truly stochastic model would necessarily be complicated and computationally taxing. While further experimental data may provide evidence that such a model is necessary to accurately capture caveolar dynamics, accounting for the behavior of individual caveolae and individual ion channels in this manner is cumbersome and beyond the scope of this project. Instead I leverage the fact that cells contain a large number of caveolae in

order to formulate a deterministic model that accurately reflects the caveolar stochasticity.

There are enough caveolae in a single cardiac cell that not only can their opening dynamics be approximated with a deterministic model, but enough caveolae are open at any given time that the sodium channels they contain can be regarded as a large subpopulation of sarcolemmal sodium channels and treated with the same deterministic, Hodgkin-Huxley formalism. In this framework, caveolar sodium channels differ from sarcolemmal sodium channels only in the complexity of their gating mechanisms. A closed caveolar neck acts as a secondary gating mechanism which not only prevents the flow of ions, but also prevents the ion channel gates from reacting to changes in membrane potential on the sarcolemma.

When a caveolar neck is closed, the state of the gates in its sodium channel remain fixed and it is only when the caveolar neck opens and the caveolar membrane potential equilibrates with the potential difference across the sarcolemma that the channel gates begin to react. So a model of caveolar current must not only account for how many caveolae are open at a given time, but also must account the history of each open caveolae. By history it is meant the time course of the caveolar membrane's voltage since the opening of its caveolar neck and the corresponding time courses of the gating variables associated with each caveolae's sodium channel. Since the voltage across the sarcolemma varies, caveolae which open at different times present their sodium channels to

the sarcolemma under different conditions. This means that caveolar sodium channels which are presented to the sarcolemma at different times, will have different time courses.

From a modeling standpoint, the dependence of the channel gate dynamics on the caveolar opening dynamics forces the gating variables to be functions of not only the time since the depolarizing stimulus, but also the time since caveolar first opening. So, letting  $t$  represent time since stimulus and  $\tau$  represent time of caveolar first opening,  $m(t, \tau)$  satisfies the boundary value problem

$$\begin{cases} \frac{\partial m}{\partial t} = \frac{m_{\infty}(V_m(t)) - m}{\tau_m(V_m(t))} & \text{in } 0 \leq \tau < t \\ m = m_{\infty}(V_m(0)) & \text{on } t = \tau \end{cases} \quad (4.6)$$

$h(t, \tau)$  satisfies

$$\begin{cases} \frac{\partial h}{\partial t} = \frac{h_{\infty}(V_m(t)) - h}{\tau_h(V_m(t))} & \text{in } 0 \leq \tau < t \\ h = h_{\infty}(V_m(0)) & \text{on } t = \tau \end{cases} \quad (4.7)$$

and  $j(t, \tau)$  satisfies

$$\begin{cases} \frac{\partial j}{\partial t} = \frac{j_{\infty}(V_m(t)) - j}{\tau_h(V_m(t))} & \text{in } 0 \leq \tau < t \\ j = j_{\infty}(V_m(0)) & \text{on } t = \tau \end{cases} \quad (4.8)$$

where  $V_m(t)$  is the potential difference across the sarcolemma at time  $t$ .

To understand the meaning of  $m$ ,  $h$ , and  $j$  in this context, consider the set of caveolae which open at time  $\tau$ . Since there are approximately  $n\rho(\tau)\Delta\tau$  caveolae which open at time  $\tau$ , then at time  $T > \tau$  the amount of sodium current due to caveolae which opened at time  $\tau$ , is  $\gamma_{Na}n\rho(\tau)m^3(t, \tau)h(t, \tau)j(t, \tau)\Delta\tau (V_m(t) - E_{Na})$

where  $\gamma_{Na}$  represents the sodium single-channel conductance. The total caveolar sodium current at time  $t$  is then the sum of all the sodium currents due to all caveolae which have opened since the stimulus (at  $t = 0$ ). Since a continuous function is used to model the caveolar first opening, this sum of currents is represented as the following integral

$$I_{cav}(t) = \left( \int_0^t \gamma_{Na} n \lambda e^{-\lambda \tau} m^3(t, \tau) h(t, \tau) j(t, \tau) d\tau \right) (V_m(t) - E_{Na}) \quad (4.9)$$

where  $m$ ,  $h$ , and  $j$  satisfy (4.6), (4.7), and (4.8), respectively. Note that this formulation leads to an underestimation of the caveolar sodium current in the initial spike. This slight underestimation is negligible and is of little consequence in this work since this research is primarily interested in the effects caveolar sodium currents on repolarization.

### 4.3 Simulation Protocols

I use this model to simulate two different experimental protocols: sodium current under voltage clamp conditions and whole cell action potential generation. The voltage clamp simulations are then compared to the experimental results of Vatta et al[3] showing good qualitative agreement and the simulated action potentials exhibit the delays in repolarization, a characteristic of LQTS.

#### 4.3.1 Voltage-Clamp Protocol

Consider a standard voltage-clamp experiment in which the membrane is fixed at a conditioning voltage until it reaches its steady-state and is then stepped up to a fixed, depolarized test potential for an arbitrarily long interval

of time. In normal cases, the time course of the sodium current under these conditions will exhibit a rapid spike upon the step up to the test potential followed by rapid, and complete, decay to zero. In the case of mutant caveolin-3, however, Vatta et al[3] discovered that the decay in sodium current was incomplete and a small, essentially constant sodium current remained long after the step to a depolarized potential. Typically such late, persistent sodium currents are attributed to a  $Na_v1.5$  gain-of-function channelopathy. However, in the case of mutant caveolin-3, no such channelopathy has been directly identified. In this section, the stochastic caveolae model is used to simulate the same voltage clamp experiment and can generate a similar late, persistent sodium current in the absence of any simulated channelopathy.

During a voltage-clamp experiment, the membrane potential is fixed, so every caveolar sodium channel experiences identical conditions upon their presentation to the sarcolemma no matter when during the application of the test potential their caveolae opens. Therefore, the caveolar current can be simplified somewhat since the time courses of the  $m$ - and  $h$ -gates are the same for every caveolar sodium channel. For given conditioning and test potentials,  $V_{cond}$  and  $V_{test}$ , respectively, it is only necessary to calculate the solutions  $m(t)$ ,  $h(t)$ , and  $j(t)$  to the initial value problems

$$\begin{cases} \frac{dm}{dt} = \frac{m_{\infty}(V_{test}) - m}{\tau_m(V_{test})} \\ m(0) = m_{\infty}(V_{cond}) \end{cases}, \quad (4.10)$$

$$\begin{cases} \frac{dh}{dt} = \frac{h_{\infty}(V_{test}) - h}{\tau_h(V_{test})} \\ h(0) = h_{\infty}(V_{cond}) \end{cases} \quad (4.11)$$

and

$$\begin{cases} \frac{dj}{dt} = \frac{j_{\infty}(V_{test}) - j}{\tau_j(V_{test})} \\ j(0) = j_{\infty}(V_{cond}) \end{cases} \quad (4.12)$$

and use them to calculate the caveolar sodium current. Since  $m_{\infty}(V_{test}) = m_{\infty}$ ,  $h_{\infty}(V_{test}) = h_{\infty}$ ,  $j_{\infty}(V_{test}) = j_{\infty}$ ,  $\tau_m(V_{test}) = \tau_m$ ,  $\tau_h(V_{test}) = \tau_h$ , and  $\tau_j(V_{test}) = \tau_j$  are all constant the solutions are simply:

$$m(t) = m_{\infty} - (m_{\infty} - m(0)) e^{-\frac{t}{\tau_m}}, \quad (4.13)$$

$$h(t) = h_{\infty} - (h_{\infty} - h(0)) e^{-\frac{t}{\tau_h}} \quad (4.14)$$

and

$$j(t) = j_{\infty} - (j_{\infty} - j(0)) e^{-\frac{t}{\tau_j}} \quad (4.15)$$

Now consider a partition of the interval  $[0, t]$  into  $k$  subintervals each of length  $\Delta t = \frac{t}{k}$  and call  $t_i = i\Delta t$  for  $i = 0, 1, 2, \dots, k$  in which  $t = 0$  corresponds to the time at which the depolarizing voltage step is made. Then the amount of whole-cell caveolar sodium current measured in the interval  $[0, t_1]$  denoted  $I_{vc,cav}(t_0)$  is

$$\begin{aligned} I_{vc,cav}(t_0) &\approx \gamma_{Na} n \lambda e^{-\lambda t_0} m^3(0) h(0) j(0) (V_{test} - E_{Na}) \\ &= \gamma_{Na} n \lambda m^3(0) h(0) j(0) (V_{test} - E_{Na}) \end{aligned} \quad (4.16)$$

since  $t_0 = 0$ .

Likewise, the whole-cell caveolar sodium current in the intervals  $[t_1, t_2]$  and  $[t_2, t_3]$  are

$$\begin{aligned} I_{vc,cav}(t_1) &\approx (\gamma_{Na} n \lambda m^3(t_1) h(t_1) j(t_1) (V_{test} - E_{Na}) + \gamma_{Na} n \lambda e^{-\lambda \cdot t_1} m^3(0) h(0) j(0) (V_{test} - E_{Na})) \Delta t \\ &= (\gamma_{Na} n \lambda m^3(t_1) h(t_1) j(t_1) + \gamma_{Na} n \lambda e^{-\lambda \cdot t_1} m^3(0) h(0) j(0)) (V_{test} - E_{Na}) \Delta t \end{aligned} \quad (4.17)$$

and

$$\begin{aligned} I_{vc,cav}(t_2) &\approx (\gamma_{Na} n \lambda m^3(t_2) h(t_2) j(t_2) + \gamma_{Na} n \lambda e^{-\lambda \cdot t_1} m^3(t_1) h(t_1) j(t_1) + \gamma_{Na} n \lambda e^{-\lambda \cdot t_2} m^3(0) h(0) j(0)) \cdot \\ &\quad (V_{test} - E_{Na}) \Delta t \end{aligned} \quad (4.18)$$

respectively.

Note that at time  $t_1$  the  $m$ -gates,  $h$ -gates and  $j$ -gates of the sodium channels in the  $n\lambda$  caveolae which experienced a first opening event in the previous interval have had time to evolve slightly according to the differential equations governing  $m$ ,  $h$ , and  $j$ , while the corresponding gates of the sodium channels in the  $n\lambda e^{-\lambda \cdot t_1}$  caveolae which are just experiencing their first opening event at that time have not yet changed from their initial steady-state values of  $m(0)$ ,  $h(0)$  and  $j(0)$ , respectively. Likewise, at time  $t_2$ , the  $m$ -gates,  $h$ -gates, and  $j$ -gates of the sodium channels in the  $n\lambda$  caveolae which experienced a first opening event in the first interval have had time to evolve even further and the  $m$ -gates,  $h$ -gates, and  $j$ -gates of the sodium channels in the  $n\lambda e^{-\lambda \cdot t_1}$  caveolae which experienced a first opening event in the second interval have had time to evolve slightly. Continuing this progression leads to

$$I_{vc,cav}(t_k) \approx \left( \sum_{i=0}^k \gamma_{Na} n \lambda e^{-\lambda \cdot t_i} m^3(t_{k-i}) h(t_{k-i}) j(t_{k-i}) \right) (V_{test} - E_{Na}) \Delta t \quad (4.19)$$

where the approximation will improve as the mesh becomes finer. Notice that

$t_{k-i} = t_k - t_i$ , so

$$I_{vc,cav}(t_k) \approx \left( \sum_{i=0}^k \gamma_{Na} n \lambda e^{-\lambda t_i} m^3(t_k - t_i) h(t_k - t_i) j(t_{k-i}) \Delta t \right) (V_{test} - E_{Na}) \quad (4.20)$$

In the limit as  $\Delta t \rightarrow 0$ , this tends toward the convolution integral

$$I_{vc,cav}(t) = \left( \int_0^t \gamma_{Na} n \lambda e^{-\lambda \tau} m^3(t - \tau) h(t - \tau) j(t - \tau) d\tau \right) (V_{test} - E_{Na}) \quad (4.21)$$

Note that after substitution of (4.13), (4.14), (4.15) into this equation, we have an integral that can be solved explicitly.

### 4.3.2 Action Potential Protocol

Incorporating the whole-cell caveolar current in (4.9) into the Pandit model[17] (see Appendix A) as an additional sodium current allows us to simulate the effects of stochastic caveolae on action potential morphology. Interestingly, the morphology of the action potential appears highly dependent upon both the choice of  $\lambda$  and the caveolar density. Recall that  $\lambda$  represents the expected average rate of caveolae openings (openings per second in our simulations). In all cases, however, the inclusion of sodium current from stochastic caveolae results in a substantial delay in myocyte repolarization, and in some cases, reactivation of the calcium current leading to an early afterdepolarization (EAD), a secondary voltage spike late in the action potential.

I wish to characterize the ways in which action potential morphology depends upon both the choice of  $\lambda$  and the number of caveolae which experience stochastic opening (or equivalently, the density of caveolae experiencing

stochastic opening). To do so I use the following protocol in the computational experiments. For each of a variety of  $\lambda$  values and numbers of caveolae, a 3 nA depolarizing stimulus is applied to a resting cell for 1 msec to elicit an action potential. For a given number of caveolae, the action potentials resulting from a variety  $\lambda$ -values are plotted. The associated action potential durations are also plotted against  $\lambda$  to show this dependence. Note that APD is defined as the time the membrane potential spends above -66 mV (the voltage which is 10% of the way from the membrane's minimum possible potential of -81.36 mV and its maximum possible potential of 66 mV).

## 4.4 Results

### 4.4.1 Voltage-Clamp Results

The results of incorporating this caveolar current,  $I_{vc,cav}$ , into the Pandit model[17] as a supplementary sodium current are summarized in Figure 4.1. The blue dashed curve represents the transient sodium current through  $Na_v1.5$  sodium channels on the sarcolemma. The green dotted curve represents the current through caveolar sodium channels and the red solid curve represents the sum of these two currents. Note that scaling of the figure has cut off the peak of the current, but clearly shows a small, persistent sodium current.

Of course, since the caveolar first opening probability density function decays asymptotically to zero as a function of time, so also does the caveolar sodium current in this voltage clamp simulation (Figure 4.1.A.), but in the

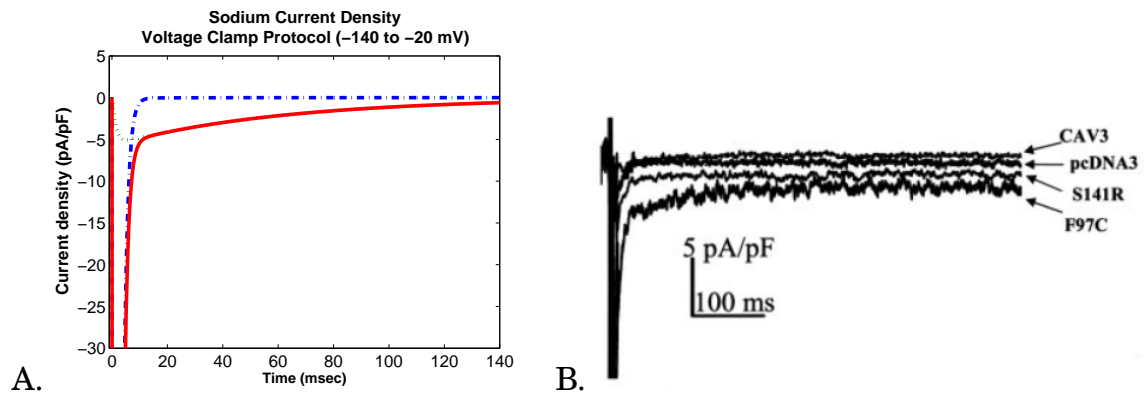


Figure 4.1: A late, persistent sodium current was observed when the membrane potential was conditioned at -140 mV and then stepped up to a sustained membrane potential of -20 mV. A. Model generated sodium current from sodium channels on the sarcolemma ( $-\cdot-\cdot-$ ), sodium current from sodium channels in stochastically opening caveolae ( $\cdot\cdot\cdot$ ), and the sum of these two sodium currents ( $-\text{—}$ ). B. Experimental data from Vatta et al[3] showing significant persistent sodium currents. Note the difference in time scales between the two figures. Since the model assumes caveolar sodium current only occurs during a caveolae's first opening after stimulus, the caveolar current will persist as long as there are caveolae left which have not already opened. In contrast, the experimental results in B. demonstrate a sodium current which persists for hundreds of milliseconds with no indication of decaying to zero. (Panel B reproduced from the 2006 paper by Vatta et al[3] with permission from the sole copyright holder, Wolters Kluwer-Lippincott Williams & Wilkins.)

short term (50-100 msec after complete inactivation of the sodium channels on the sarcolemma) these results are in close agreement with the those generated by Vatta et al (Figure 4.1.B.). One explanation for the lack of ultimate current decay in the experimental results is that perhaps there exists a mechanism by which some caveolar membranes will return to near resting potentials thereby allowing the sodium channels they contain to recover from inactivation. Subsequent opening of such a caveolae would allow for the reopening of its sodium channel and an additional inward sodium current. Further computational and experimental studies are necessary to determine if a caveolar mechanism may exist that could give rise to an indefinitely persistent current.

#### 4.4.2 Action Potential Morphology Results

Interestingly, the dynamics are highly dependent upon both our choice of  $\lambda$  and the number of caveolae present in the cell. In Chapter 2 an estimated 200-250 caveolae per pF, or 20000 to 25000 caveolae per simulated cell was calculated. What is found using the model of stochastic caveolae is that even for much smaller caveolar densities there are ranges of the Poisson rate parameter value which give rise to substantial delays in repolarization and in some cases reactivation of the calcium current leading to early afterdepolarizations. Furthermore, for larger caveolar densities nearer to the levels we expect, there are values  $\lambda$  that result in the total elimination of the repolarization phase. In such cases, the cell appears to settle into a new equilibrium at a membrane poten-

tial near plateau values, never returning to rest. The transitions between each of these characteristic behaviors are illustrated in Figure 4.2. For the sake of readability, only the results for select  $\lambda$ -values are shown in the left column, but the plots in the right column summarize how APD varies with  $\lambda$  for each of the selected caveolar densities.

While only representative time courses are shown, the general results indicate that for each  $n$ -value, the delay in repolarization is a nonmonotonic function of  $\lambda$ . Notice that in all three cases shown in Figure 4.2 relatively small and relatively large  $\lambda$ -values correspond to relatively small delays in repolarization whereas intermediate values correspond to much more substantial delays in repolarization. This should be expected if one considers the role of  $\lambda$  in the model. Small  $\lambda$ -values indicate low probability of caveolae opening leading to a small number of caveolar first openings throughout the action potential and little additional current. On the other hand, a large  $\lambda$ -value indicates a high probability of opening leading to many caveolae experiencing their first opening early in the action potential, leaving few to open for the first time late in the action potential during the repolarization phase. In both cases, the result is a relatively small delay in repolarization. However, when  $\lambda$  takes on intermediate values, a substantial delay in repolarization characterized by an increase in action potential duration is seen.

The difference between the three cases illustrated in Figure 4.2 is that as we increase the number of caveolae from 14000 to 18000 fundamental changes

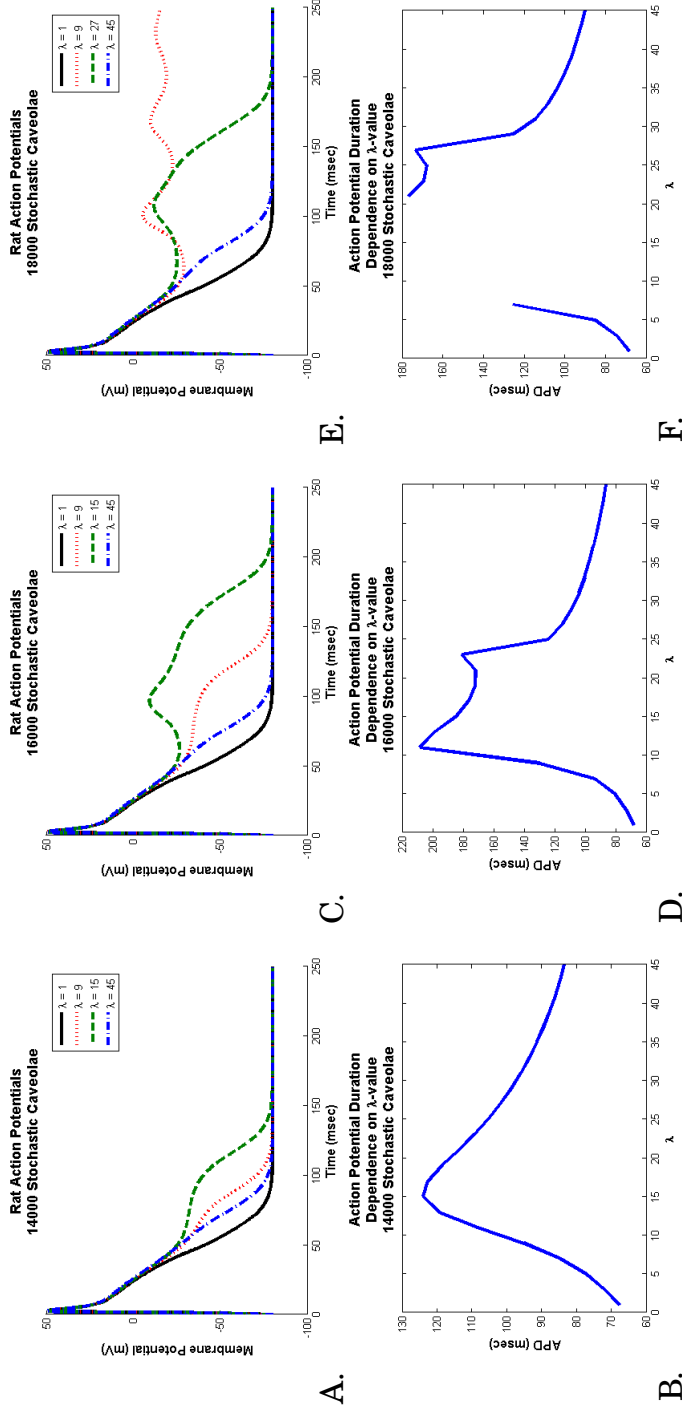


Figure 4.2: Effects of stochasticity in caveolar openings on action potential morphology and afterdepolarization formation. Graphs of the action potential morphologies with (A) 14000 caveolae for a range of  $\lambda$ -values and (B) the associated action potential duration dependence on  $\lambda$ . Early afterdepolarizations, along with more substantial delays in repolarization, do occur for a range of  $\lambda$ -values when the number of caveolae is increased to 16000 (C & D). Increasing the number of caveolae further to 18000 leads to early afterdepolarizations, and in a range of  $\lambda$ -values, the system settles into a new equilibrium (E). This complete extinguishing of the repolarization phase shows up as a discontinuity in the graph of action potential duration dependence on  $\lambda$ -value (F).

occur in the nature of the repolarization delays seen at intermediate  $\lambda$ -values. The inclusion of 14000 caveolae results in elongation of the action potential due entirely to the inward caveolar sodium current which persists late in the action potential, but for all values of  $\lambda$  the action potential time course is monotone decreasing after peak overshoot. If the number of caveolae is increased to 16000, then for a range of  $\lambda$ -values near  $\lambda = 15$ , a secondary spike (an early afterdepolarization) in membrane potential interrupts the repolarization phase. In Figure 4.3 we see that this secondary spike is caused by a reactivation of the calcium current which is consistent with the mechanisms identified experimentally. If we increase the number of caveolae still further to 18000, then we not only see EADs for certain values of  $\lambda$ , but for a range of  $\lambda$ -values between approximately 7 and 21 a train of EADs serves to extinguish repolarization altogether and the system tends toward a new steady-state at a substantially depolarized membrane potential.

A simple examination of the differential equations that constitute the Pandit model confirms that fact that this steady-state is, in fact, a true fixed point for the system and not a computational anomaly. This particular finding is puzzling, though, because it suggests that the resting membrane state is not a cardiac cell's only locally stable state. Whether this is a peculiarity of the Pandit model, or a true physiological feature of cardiac cells, is a topic for further investigation. What is most important, though, is the fact that stochasticity in caveolae can indeed lead to delays in repolarization and early

$v = -5.315$	$m = 0.9978$	$h = 8.62 \cdot 10^{-6}$	$j = 8.62 \cdot 10^{-6}$
$d = 0.8805$	$f_{11} = 0.0187$	$f_{12} = 0.0187$	$Ca_{inact} = 0.8281$
$r = 0.61367$	$s = 0.00299$	$s_{slow} = 0.00299$	$r_{ss} = 0.6279$
$s_{ss} = 3.42 \cdot 10^{-4}$	$y = 3 \cdot 10^{-6}$	$P_{C1} = 0.01986$	$P_{O1} = 0.00\bar{7}$
$P_{O2} = 1.46 \cdot 10^{-4}$	$P_{C2} = 0.9722$	$HTRPNCa = 0.14$	$LTRPNCa = 0.0327$
$[Ca^{2+}]_i = 8.77 \cdot 10^{-4}$	$[Na^+]_i = 7.0589$	$[K^+]_i = 131.9$	$[Ca^{2+}]_{ss} = 0.002076$
$[Ca^{2+}]_{JSR} = 0.2954$	$[Ca^{2+}]_{NSR} = 0.2978$		

Table 4.1: Values of the variables at a superthreshold fixed point of the Pandit system.

afterdepolarizations.

In some cases of increased caveolar density, there are ranges of  $\lambda$ -values for which repolarization remains incomplete and the system settles into a new equilibrium at a membrane potential substantially above threshold (See Table 4.1). Evidently, for certain values of  $n$  and  $\lambda$ , the extra depolarizing caveolar sodium current along with the calcium current reactivation that it induces serve to maintain the cell's relatively depolarized state long enough to allow slower variables to migrate into new basins of attraction and for the system to equilibrate at this new fixed state.

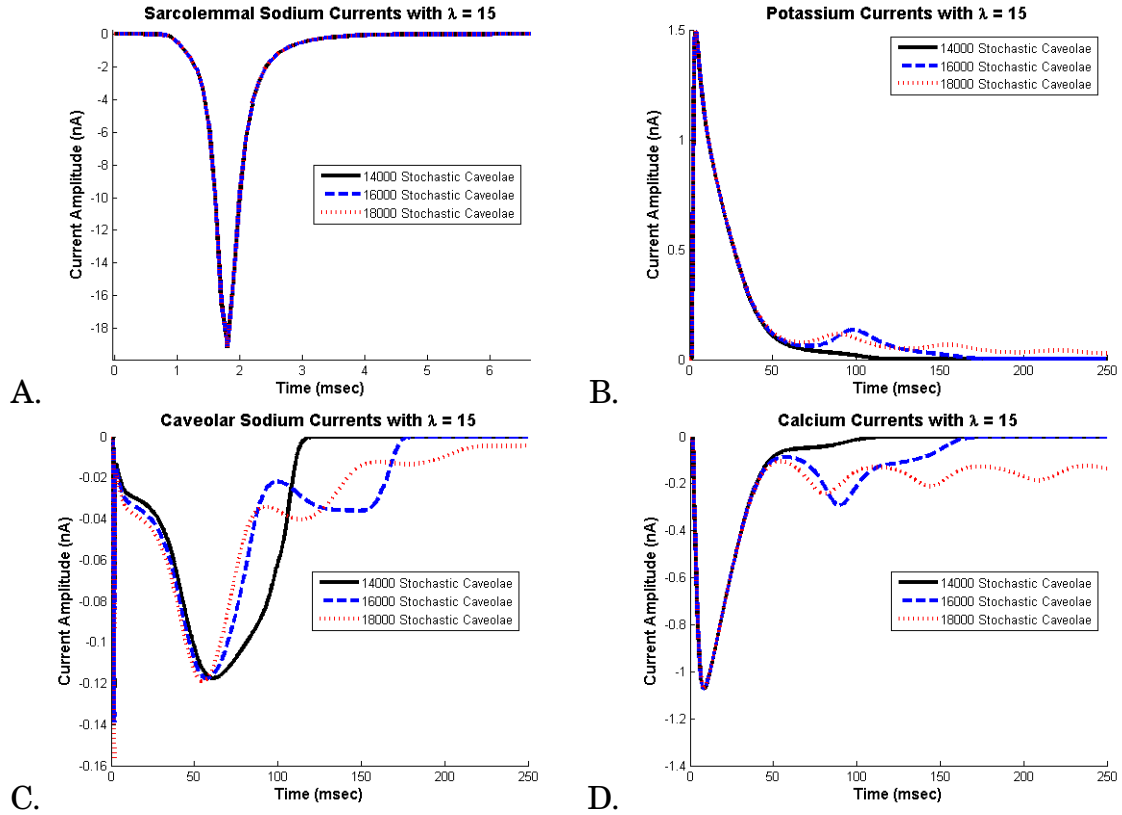


Figure 4.3: This figure illustrates the differences in the time courses of the ionic currents that result from fixing  $\lambda$  at an intermediate value and varying the number of caveolae. In this scenario,  $\lambda$  is fixed at 15 and plots of A. the transient sodium current,  $I_{Na}$ , B. the potassium current,  $I_t$ , C. the caveolar sodium current,  $I_{cav}$ , and D. the L-type calcium current,  $I_{CaL}$ , associated with 14000, 16000 and 18000 stochastic caveolae have been superimposed upon one another. Notice that when 16000 and 18000 caveolae are included, calcium re-activation occurs leading to a single early afterdepolarization with 16000 caveolae and a series of afterdepolarizations with 18000 caveolae. In the case of 18000 caveolae, repolarization is delayed long enough for the slower variables to enter the basin of attraction for a new fixed point and the system settles into a new equilibrium state.

### 4.5 Stochasticity in the Three-Variable Model

We have seen that the incorporation of stochastic caveolae into the formulation of a physiologically detailed model results in significant changes in action potential morphology, most significantly, a delay in repolarization, the emergence of early afterdepolarizations, and in some cases equilibration of the system at a new steady-state. Of interest is whether the action potential generated by the far simpler three-variable model would exhibit these same changes if it were to include caveolar stochasticity.

To determine this, I formulate a stochastic caveolar sodium current in the same way as was done in the case of the Pandit model. I then simulate action potentials for a variety of caveolar densities and  $\lambda$ -values, and plot the results. Recall that the stochastic caveolar current that was incorporated into the Pandit model was defined as follows:

$$I_{cav}(t) = \left( \int_0^t \gamma_{Na} n \lambda e^{-\lambda\tau} m^3(t, \tau) h(t, \tau) j(t, \tau) d\tau \right) (V_m(t) - E_{Na}) \quad (4.22)$$

in which  $m$ ,  $h$ , and  $j$  were governed by a set of complicated partial differential equations. In the three-variable model, there is no differential equation governing sodium activation and the differential equation associated with  $h$  is much simpler. Also, recall that the parameter  $\kappa$  was used in the three-variable model to denote the total sodium conductance with  $\kappa = 1$  meaning 100% of the sarcolemmal sodium conductance and no contribution from caveolar sodium channels and  $\kappa = 1.42$  meaning a 42% increase in whole-cell sodium conductance due to the inclusion of 25000 sodium channel-containing caveolae.

Therefore, the maximum caveolar conductance is denoted  $(\kappa - 1)$ . This is used in place of the product  $\gamma_{Na}n$  in this formulation of caveolar current. So the caveolar current in the context of the three-variable model is

$$I_{cav}(t) = \frac{\left( \int_0^t (\kappa - 1) \lambda e^{-\lambda\tau} \bar{h}(t, \tau) d\tau \right) \left( \frac{\bar{v} + 81.36}{147.36} \right)^2 (\bar{v} - 66)}{\bar{\tau}_{Na}} \quad (4.23)$$

with  $\bar{h}(t, \tau)$  governed by

$$\frac{\partial \bar{h}}{\partial t} = \begin{cases} \frac{-\bar{h}}{\bar{\tau}_{hc}} & \frac{\bar{v} + 81.36}{147.36} \geq v_h \\ \frac{0.68 - \bar{h}}{\bar{\tau}_{ho}} & \frac{\bar{v} + 81.36}{147.36} < v_h \end{cases} \quad (4.24)$$

for  $0 \leq \tau < t$  and  $\bar{h} = 0.68$  on  $t = \tau$ . These equations use the optimal parameter values derived in the previous chapter.

When this caveolar sodium current is incorporated into the three-variable model, the effects on action potential morphology are similar to, but less pronounced than, the effects seen when stochastic caveolae are incorporated into the more physiologically detailed Pandit model. These results are summarized in Figure 4.4.

In this case, the inclusion of caveolar stochasticity introduces a noticeable delay in repolarization, but this delay is relatively small in comparison to the delays seen in Figure 4.2 and the maximum delays occur at  $\lambda$ -values which are an order of magnitude greater than those at which maximum delays were elicited with the more physiologically detailed model. Additionally, this model fails to exhibit the early afterdepolarizations or the tendency to equilibrate at a new steady-state seen in Figure 4.2. The reason for this is likely due to the fact

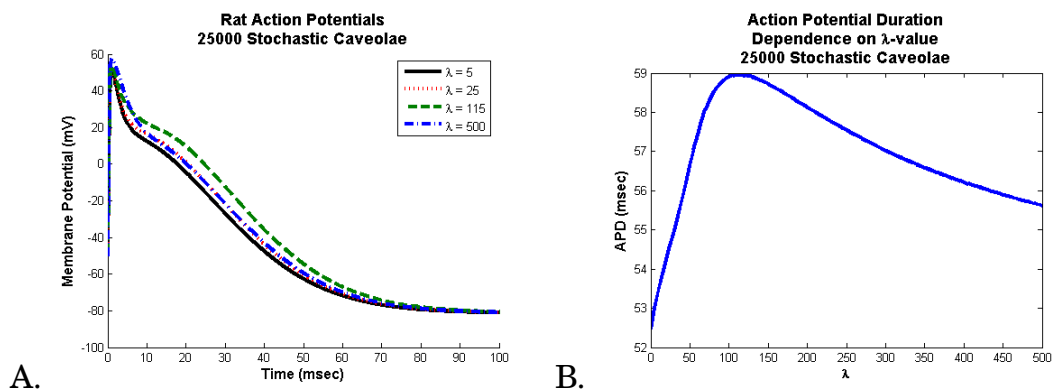


Figure 4.4: This figure shows the effects that incorporating stochastic caveolae into the three-variable model has on the simulated action potential morphology. As in Figure 4.2 action potentials have been plotted for select values of  $\lambda$  (A) and action potential duration as a function of  $\lambda$ -value (B). In this case,  $\kappa = 1.42$  was used to simulate the inclusion of 25000 stochastic caveolae in our simulated cell. These plots indicate a noticeable delay in repolarization as expected from the same computational experiment using the physiologically detailed model of stochastic caveolae. However, the delays in repolarization generated by the physiologically detailed model were substantially more pronounced even with far fewer stochastic caveolae than are the delays seen in this figure. Furthermore, the maximum delays occurred at  $\lambda$ -values that are an order of magnitude greater than those at which the maximum delays occur using this model. Also the system does not tend towards a secondary equilibrium for any caveolar densities or  $\lambda$ -values as did the physiologically detailed model.

that in the three-variable model, the time constant associated with the closing of the  $\bar{h}$ -gate is fixed at a very small value in order to counteract the sodium activation which reacts instantaneously to changes in membrane potential.

In contrast,  $\tau_h$  in the Pandit model varies in a voltage-dependent manner over three orders of magnitude during an action potential. A plot of  $\tau_h$  as a function of membrane potential is shown in Figure 4.5. Note that  $\tau_h$  reaches a peak of approximately 0.1 seconds near -60 mV and decays in either direction from this point, but even at its minimum  $\tau_h$  is no less than 0.00045 seconds and during most of the plateau and repolarization phases,  $0.001 < \tau_h < 0.01$ . This means that even though the number of caveolae experiencing their first opening tapers off, the rate at which the  $h$ -gate changes conformation slows markedly near the end of the repolarization phase. Therefore, while fewer non-inactive caveolar sodium channels are presented to the sarcolemma during repolarization, those which are presented experience much slower inactivation and so can contribute current much longer.

On the other hand,  $\tau_{hc}$  is fixed at 0.000342 seconds in the three-variable model independent of membrane potential. This means that during most of the three-variable model-generated action potential, inactivation of the caveolar sodium channels occurs much more rapidly than is physiologically accurate leading to a smaller overall caveolar sodium current especially late in the action potential and the much less pronounced delays in repolarization seen in Figure 4.4. Nevertheless, a noticeable delay in repolarization is still evi-

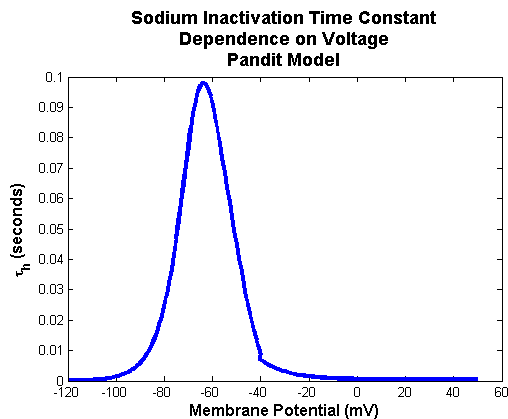


Figure 4.5: The graph of  $\tau_h$  showing high variability.

dent with the three-variable model of stochastic caveolae lending additional credence to our hypothesis that stochastic flickering of caveolae constitutes a plausible explanation for the emergence of a persistent sodium current in cases of mutant caveolin-3.

## 4.6 Conclusion

By incorporating stochasticity into the opening dynamics of caveolae a late, persistent sodium current under voltage clamp conditions like those seen in the case of mutant caveolin-3 can be simulated. In addition, this model of stochastic caveolae produces action potentials which exhibit a delay in repolarization and early afterdepolarizations. Both of these are electrophysiological features associated with Long-QT Syndrome. Importantly, this model does not include any changes in sodium channel kinetics. In contrast to the mechanism proposed by Vatta et al in which a mutant caveolin-3/ $\text{Na}_v1.5$  interac-

tion induces a gain-of-function channelopathy[3], these findings indicate that if caveolin-3 mutation results in stochastically flickering caveolae, arrhythmic effects could emerge solely as a product of this caveolar stochasticity.

Of course, since the caveolar first opening probability density function decays asymptotically to zero as a function of time, so also does the caveolar sodium current in this voltage clamp simulation. Therefore, this model is unable to simulate a truly persistent sodium current, but in the short term (50-100 msec after sarcolemmal sodium channels have completely inactivated) the results are still in close agreement with the those generated by Vatta et al[3]. One explanation for the lack of ultimate current decay in the experimental results is that perhaps there exists a mechanism by which some caveolar membranes can return to near resting potentials thereby allowing the sodium channels they contain to recover from inactivation. Subsequent opening of such caveolae would allow for the reopening of their sodium channels and an additional inward sodium current. Further computational and experimental studies are necessary to determine if a caveolar mechanism may exist that could give rise to an indefinitely persistent current.

Additionally, from a mathematical point of view, interesting questions arise related to the transitions the system undergoes as the caveolar density is increased. Clearly, some sort of bifurcation occurs between 14000 caveolae per cell and 16000 caveolae per cell which leads to the reactivation of calcium and an early afterdepolarization. A subsequent bifurcation occurs between 16000

and 18000 caveolae per cell which drives the system toward a new equilibrium for certain  $\lambda$ -values. A full characterization of the way in which the dynamics of membrane potential change with changes in caveolar density and  $\lambda$ -value might provide additional insight into the possible role that caveolar stochasticity plays in arrhythmogenesis and represents an interesting direction to pursue in future work.

The findings we discussed in this chapter suggest that an entirely new biophysical mechanism may underpin certain types of Long-QT Syndrome - one that is based on pathological caveolar kinetics rather than pathological channel kinetics. Given these results, and the results of previous experimental studies of caveolar function, it is likely that caveolae play a substantial, but largely unrecognized, role in cardiac electrophysiology. New experiments investigating this role are needed if a more detailed understanding of both cardiac  $\beta$ -adrenergic response and possible caveolae-related arrhythmogenic mechanisms is to be gained.

## CHAPTER 5 CONCLUSIONS AND FUTURE WORK

The objectives of this research were three-fold: First, to develop a physiologically detailed model of rat action cardiac action potential that incorporates emerging data related to the effects of caveolae on sodium current. Second, to develop a second model that replicates the results generated by the more detailed model, but which is simple enough to allow for more rigorous mathematical analysis so that explicit dependencies between parameter values and physiologically relevant quantities can be extracted. Third, to use modifications of these models to test a novel hypothesis surrounding the link between caveolar dysfunction and a serious cardiac condition called Long-QT Syndrome.

All three of these objectives were achieved. The caveolae-inclusive model which is based largely on an existing model of rat action potential succeeded in replicating experimental results and suggests ways that caveolar sodium current might impact overall cardiac function. The three-variable model succeeded in replicating much of the same behavior seen in the caveolae-inclusive model, but did so using a substantially lower-dimensional system of ordinary differential equations. The incorporation of caveolar stochasticity into both of these models resulted in a delay in cell repolarization suggesting that such stochasticity provides a plausible mechanism through which caveolin-3 mutation might lead to Long-QT Syndrome.

This work provides new insight into the multi-faceted role that caveo-

lar sodium current may play in heart function and proposes new hypotheses which will hopefully inform future experimentation. What follows is a summary of these insights and hypotheses as well as a discussion of the challenges encountered in this research and ways that these challenges might be met in future studies. This chapter will also discuss some of the many avenues of exploration that were beyond the scope of this investigation, but which constitute paths my research will take in the future.

## 5.1 Summary of Key Findings

### 5.1.1 Derivation of Caveolae Density Estimates

I have demonstrated a viable method for estimating the density of caveolae in a cardiac cell that is based on inspections of sodium I-V curves. This method predicts that cardiac caveolae exist at densities in the range of approximately 2-7 caveolae per  $\mu m^2$ . These predictions are in very good agreement with estimates made using other methods[29, 19]. One minor pitfall related to the derivation of caveolar density was a lack of consistency between the two sets of experimental data. The sodium I-V curves generated from the experimental studies both report results in terms of current density, but there was an order of magnitude difference between those results. Undoubtedly, some of this variation can be explained by the fact that the experiments were done at slightly different sodium concentrations, but another explanation offered by Dr. Shibata, in whose lab the experiments were conducted, was that con-

trol for cell size may not have been as good in the 1999 results as they were in the 2008 results. Another related pitfall was the lack of a solid estimate for sodium single-channel conductance at the sodium concentrations that were used in the experiments. It appears that no study has to date been done which systematically explores the dependence of single-channel conductance on both the extracellular and intracellular ion concentrations. Such a study would help to provide more accurate measurements of the number of caveolae which are opening due to  $\beta$ -adrenergic stimulation.

### 5.1.2 Caveolar Sodium Current Increases Upstroke Velocity

My simulations using the caveolae-inclusive model suggest that while the overall shape of the action potential should be largely unaffected by increases in sodium current due to the opening of caveolae, the upstroke velocity of the action potential should increase substantially. The addition of 25000 caveolar sodium channels in a 100 pF simulated cardiac cell resulted in a nearly 30% increase in maximum upstroke velocity. This increase appeared to be linear with respect to percent increase in sodium current, a result that is consistent with other computational and experimental data[24, 26, 27]. These findings are important because increases in maximum upstroke velocity are known to increase conduction speed of the excitatory wave in cardiac tissue with a normalized conduction velocity that is reported to be directly proportional to the square root of the normalized maximum upstroke velocity[26].

Since the inclusion of 25000 caveolar sodium channels in the model results in a maximum upstroke velocity that is 129% of baseline, I expect the opening of caveolae would increase conduction velocity by up to 14%. While investigation of conduction velocity in  $\beta$ -agonist treated cardiac tissue patches are necessary to test this result, this finding suggests that the PKA-independent pathway of  $\beta$ -adrenergic stimulation may play a significant role in modulating the speed of the excitatory wave in the heart.

### 5.1.3 Linear Upstroke Velocity Dependence

While the caveolae-inclusive model was far too complex to allow for a rigorous mathematical analysis, the three-variable model provided an accurate replication of its action potential morphology with a simplicity that made analysis much simpler. One unfortunate consequence of the complexity in the caveolae-inclusive model was that even though computational results indicated a nearly linear dependence of maximum upstroke velocity on caveolar sodium current, the actual linear relationship could not be derived directly from the model. In contrast, it was possible to extract an explicit linear relationship between these two quantities in the three-variable model and the agreement with the computational results was quite good. As previously mentioned, however, the degree to which the maximum upstroke velocity depended upon the caveolar sodium current differed between these two models. Future incarnations of the three-variable model will simulate the activation gating mechanisms more

accurately. Hopefully, an explicit linear relationship that is physiologically accurate can be extracted from these refined models.

#### 5.1.4 Caveolar Dysfunction as LQTS Mechanism

Links are known to exist between mutations in *CAV3*, the gene encoding the caveolae structural protein caveolin-3, and a variety of pathological conditions affecting skeletal and cardiac muscle[37, 42, 38, 39, 41, 40, 43, 3]. One of these, a type of Long-QT Syndrome (LQT9) is characterized by a late, persistent sodium current and a delay in repolarization of cardiac cells. Since it is known that caveolin-3 is critically involved in the opening of caveolae in cells which are treated by a  $\beta$ -agonist[2], I hypothesized that caveolin-3 mutations might alter the opening dynamics of caveolae leading to similar sodium currents that persisted late in the action potential and inhibited repolarization. By incorporating caveolar stochasticity into the two aforementioned models of rat action potential, I was able to generate persistent sodium currents like those seen experimentally, delays in cell repolarization, and in some cases, early afterdepolarizations, a common indication of LQTS.

Importantly, this model does not include any changes in channel kinetics to which many types of LQTS have been attributed. These findings present an entirely new possibility, that changes in caveolar dynamics might underpin certain types of LQTS. This has important implications for the use of  $\beta$ -agonist/ $\beta$ -blocker therapies for a variety of conditions. Knowing more about the ways in

which caveolin-3 mutation and the  $\beta$ -agonist- $G_s$ - $\alpha$ -caveolin pathway affect caveolar opening dynamics and modulate whole-cell sodium current will be crucial to developing more targeted treatments for heart and heart-related conditions.

Additionally, from a mathematical point of view, interesting questions arise related to the transitions from normal to arrhythmogenic conditions in the dynamical systems used to model stochasticity in caveolae. Why different combinations of caveolar densities and open rates give rise to such vastly different behavior is an interesting mathematical question on its own, but the solution might provide further insight into the underlying biophysical mechanisms that may be at work in these pathological cases.

## 5.2 Future Work

### 5.2.1 Single-Caveola Model

While conclusive evidence exists for the presence of functional  $\text{Na}_v1.5$  channels in the caveolar membrane, direct evidence for the presence of other channel types remains elusive. Unlike caveolar sodium current that can be isolated with the aid of a long-lasting, membrane impermeant sodium channel blocker, no such blockers exist for other channel types. Arguments for the presence of other channel types in the caveolar membrane rely on indirect evidence from studies using Western analysis, immunoelectron microscopy, and immunofluorescent confocal microscopy to show colocalization of  $\text{Ca}_v1.2a$  and  $\text{K}_v1.5$ , as well as  $\text{Na}_v1.5$ , channels to isolated caveolar membranes. In addi-

tion, the clustering of  $\text{Na}_v1.5$ ,  $\text{Ca}_v1.2$ , and  $\text{K}_v1.5$  channels with caveolin-3 has been demonstrated[21].

Therefore, it is quite likely that upon opening, caveolae present functioning calcium and potassium ion channels (and perhaps other transport proteins) as well as sodium ion channels to the sarcolemma. Electrophysiological ramifications of this on the intracaveolar environment and the states of the channels in the caveolar membrane needs to be explored. One possible method for approaching this question is to model single caveolae and their evolution in the closed state.

#### 5.2.1.1 Conceptual Foundations

The most important consideration related to this model is the stochastic nature of single ion channels. As mentioned in Chapter 1, the introduction of gating variables which are smooth, deterministic functions of time and voltage in the Hodgkin-Huxley equations belies the fact that, in reality, the opening and closing of individual ion channels are stochastic events. Consider the formulation of the sodium current, for instance:

$$I_{Na} = \overline{g_{Na}} m^3 h (V_m - E_{Na}) \quad (5.1)$$

where  $m$  and  $h$  are variables ranging from  $[0, 1]$  representing the proportion of  $m$ -gates and  $h$ -gates (among those gates in the many sodium channels being considered) which are in their open conformation. In the Hodgkin-Huxley

formalism these variables satisfy the differential equations:

$$\frac{dm}{dt} = \frac{m_{\infty}(v) - m}{\tau_m(v)} \quad (5.2)$$

$$\frac{dh}{dt} = \frac{h_{\infty}(v) - h}{\tau_h(v)} \quad (5.3)$$

Thus, the product  $\overline{g_{Na}}m^3h$  represents the total sodium conductance of the patch of membrane (or whole cell) being considered. At the level of individual channels as one would find in a single caveolae, however, this deterministic approximation fails. On this scale,  $m$  and  $h$  represent the probabilities that a given  $m$ -gate or  $h$ -gate, respectively, are in their open conformation.

For the purposes of conduction, individual sodium channels exist in one of two states - either permeable or impermeable to sodium ions. A sodium channel is permeable to sodium ions if all three of its  $m$ -gates and its single  $h$ -gate are open simultaneously, and otherwise is impermeable. So at the single channel level, equation 5.1 is nonsensical; single channels never offer partial permeability. Only when the number of channels under consideration is large (e.g. the number in a whole cell or large membrane patch) can we disregard this stochasticity and consider a deterministic approximation.

In the case of single caveolae which we assume typically contain only one sodium channel, stochasticity of individual channels becomes an important consideration. Similarly, any other ion channels, pumps, or exchangers that reside in a single-caveolae would necessarily exist in such small numbers

that stochasticity in their dynamics cannot be ignored either. Therefore, any model of single-caveolae electrodynamics must be formulated in a probabilistic manner.

#### 5.2.1.2 Formulation of a Single-Caveola Model

When the caveolae are closed, interactions between the intracaveolar space and intracellular space are dictated by the number and type of ion transporters in the caveolar membrane and the changes in intracaveolar ion concentrations. Like standard models of cardiac action potential, a single-caveola model would exploit the fact that the rate of change of membrane potential is directly proportional to the sum of the transmembrane ionic currents. However, unlike models that are formulated using the Hodgkin-Huxley formalism, these could not be deterministic equations. Instead, the channel gates would be allowed to change conformation between two states - open and closed - in a stochastic manner and the probabilities associated with each conformation would be functions of membrane potential. In addition, differential equations accounting for changes in the ionic concentrations within the intracaveolar space would need to be included since relatively small currents can substantially impact ionic concentrations in such small microdomains.

#### 5.2.1.3 Preliminary Work with a Deterministic Model

One first attempt at gaining an understanding of the way that a single caveola might evolve I made was to define a bulk caveolar compartment and

analyze the way in which the state of this compartment changed when no interaction with the extracellular space was allowed. The system 5.4 is the system of differential equations governing of the intracellular-intracaveolar interactions.

$$\begin{aligned}
 \frac{dV_c}{dt} &= - \left( \frac{1}{C_m} \right) I_c \\
 \frac{dm_c}{dt} &= \frac{\bar{m} - m_c}{\tau_m} \\
 \frac{dh_c}{dt} &= \frac{\bar{h} - h_c}{\tau_h} \\
 \frac{dj_c}{dt} &= \frac{\bar{j} - j_c}{\tau_j} \\
 \frac{d[Na]_c}{dt} &= 10^{-6} \frac{I_c}{F \cdot Vol_c}
 \end{aligned} \tag{5.4}$$

where the sodium current through the bulk caveolar membrane is denoted

$$I_c = n\gamma_{Na}m_c^3h_cj_c(V_c - E_{Na_c}) \tag{5.5}$$

and  $E_{Na_c} = \frac{RT}{F} \ln \left( \frac{[Na]_c}{[Na]_i} \right)$  represents the sodium Nernst potential across the caveolar membrane.

#### 5.2.1.4 Evolution of the Closed Bulk Caveolar Space

Figure 5.1 illustrates the evolution of the bulk caveolar membrane potential as a function of time from caveolar closing. In this simulation, it is assumed that the caveola closes during the diastolic interval when the caveolar membrane is initially at the cell's resting membrane potential, the intracaveolar environment is initially identical to the extracellular environment, and the only ion transporters contained in the caveolar membrane are sodium channels.

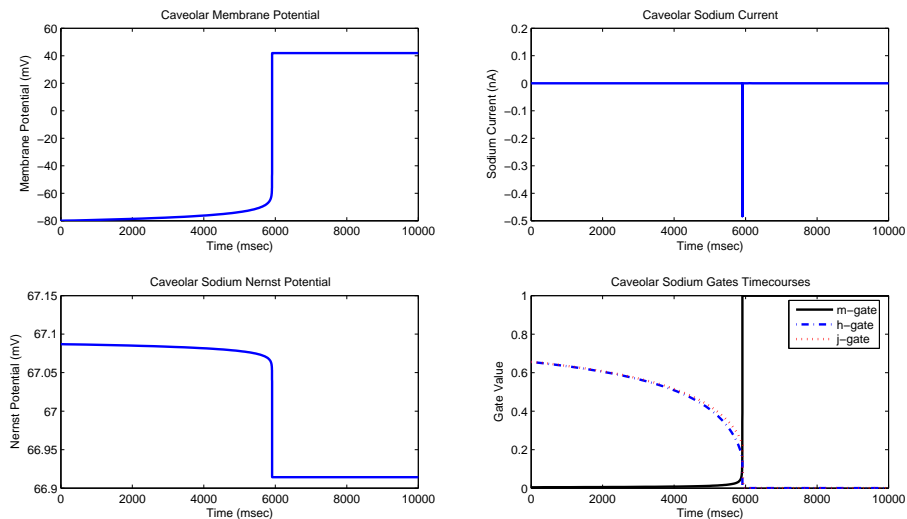


Figure 5.1: Evolution of the caveolar state from close at -80 mV steady state values

It appears that the caveolar membrane initially reacts very slowly to the slight depolarizing sodium current. Eventually, however, the  $m$ -gate value increases enough to produce a brief window current during which the voltage jumps rapidly to a steady state near +40 mV and the sodium channels inactivate. Since, the only ion transporters present in the caveolar membrane are sodium channels, the caveolar membrane is prevented from repolarizing and the sodium channels remain locked in their inactivated state until the caveola opens again.

Of course this deterministic model is not particularly relevant since the values of the gating variables provide probabilities that gates are in their open states. In reality, there would be no trickle of sodium current in a closed caveola

that would slowly lead to a spike. Such a spike would occur as a random event which was just more likely at certain potentials than others. Developing a model which truly accounts for the stochasticity at the level of caveolae is a direction I plan to take this work.

### 5.2.2 The Capacitance Question

One consideration that has been ignored throughout this research is the fact that the opening of many caveolae may have non-negligible effects on whole-cell capacitance. As has been mentioned, each  $\text{cm}^2$  of membrane has a capacitance of approximately 1 microfarad. As well as presenting additional sodium channels to the sarcolemma, the opening of caveolae must necessarily increase the area of the plasma membrane surrounding the cell. One would expect that an increase in capacitance then must accompany this increase in surface area. Whether this increase in capacitance is truly linear with respect to the area of caveolar membrane presented to the sarcolemma, or whether the distinct shape of the caveolae in some way mitigates the expected increase in capacitance is unknown. To this point no experiments have measured changes in whole-cell capacitance caused by the opening of caveolae, so I cannot be sure of the extent to which my decision to neglect these possible changes has affected my results.

As a preliminary attempt to assess how the opening of caveolae might affect whole-cell capacitance, let us suppose that the opening of a caveolae in-

creases the whole-cell capacitance by  $1 \mu\text{F}$  per  $\text{cm}^2$  of membrane that constitutes the caveolae. To help us get a sense of scale, assume as we have throughout, that a cell with a whole-cell capacitance of  $100 \text{ pF}$  has between 20000 and 25000 caveolae each with a diameter of approximately  $75 \text{ nm}$ . With these numbers, the opening of all a cell's caveolae would result in an increase of between  $3.5$  and  $4.4 \text{ pF}$  to whole-cell capacitance (i.e. a  $3.5\%$  to  $4.4\%$  increase in whole cell capacitance). Since increasing capacitance results in a decrease in the rate at which membrane potential changes, we would suspect that such an increase would counteract (to a small degree) the increases in upstroke velocity and peak overshoot that we have shown should result from the caveolar sodium current. We would also suspect that this would slow the repolarization phase of the action potential as well. Figure 5.2 illustrates the changes in action potential morphology that result from simulating the combined effects of caveolar sodium current and these increases to whole-cell capacitance.

A next step in refining the models I have developed will be to account for the changes in capacitance that surely occur when caveolae open and systematically assess the ways that these changes impact the results I have presented in this research.

### 5.2.3 A Spatially-Extended Model

Lastly, I plan to formulate spatially-extended PDE versions of these models. Understanding the caveolar contributions to single-cell behavior is

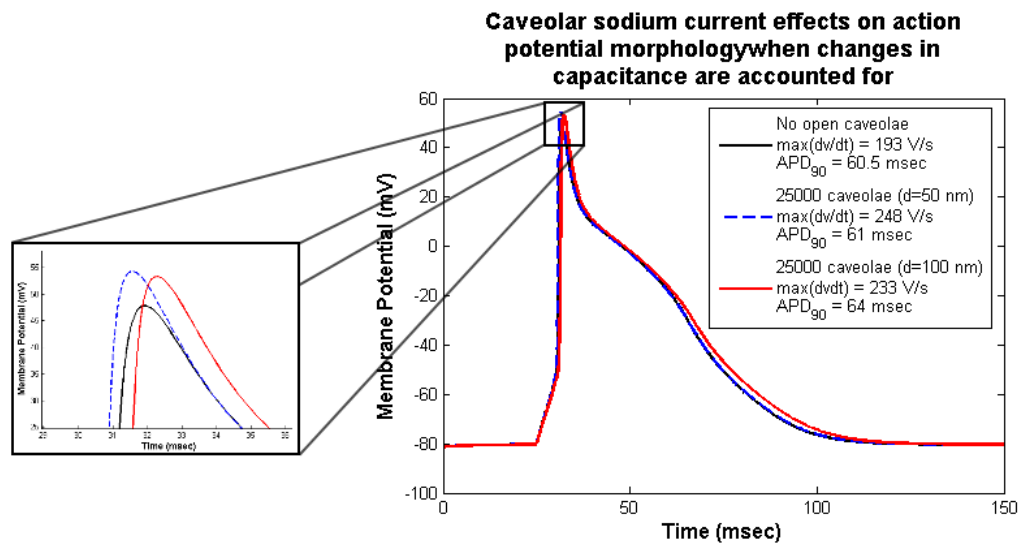


Figure 5.2: Accounting for capacitance in the caveolae-inclusive model. It appears that even accounting for the added capacitance maximum upstroke velocity would be increased, but less so if the caveolar diameters were assumed to be 100 nm as opposed to 50 nm. Note that doubling the diameter of the caveolae would result in a four-fold increase in the surface area of the caveolar membrane added to the sarcolemma. While the increase in capacitance due the larger caveolae is still not enough to counteract the increase to maximum upstroke velocity due to the additional sodium current, it is enough to noticeably slow changes in  $\frac{dv}{dt}$  late in the action potential leading to a slight increase in APD.

a critical first step in understanding the effects that caveolae have on whole-heart electrodynamics, but there are many other factors that come into play when many cells are coupled together. There tremendous variation in the molecular composition of cells in different parts of the heart, and even transmurally in small sections of tissue. Cells with different types and densities of ion channels may react differently to the addition of caveolar sodium current and the molecular constituents of the caveolae themselves may be different depending upon cell type and location. Additionally, cell remodeling that occurs as a result of cardiac infarction or other tissue injury can have substantial impacts on the electrodynamics of cells. Testing the way in which the  $\beta$ -adrenergic response of caveolae impacts propagation through a heterogeneous patch of tissue will be an important next step in understanding the role that caveolae play in overall heart function and it is a direction I will take this research in the future.

## APPENDIX PANDIT MODEL OF RAT ACTION POTENTIAL

The system of 26 nonlinear, coupled, ordinary differential equations as

developed by Pandit et al[17]:

$$\begin{aligned}
\frac{dv}{dt} &= -\left(\frac{1}{C_m}\right) (I_{Na} + I_{CaL} + I_t + I_f + I_{K1} + I_B + I_{NaK} + I_{NaCa} + I_{CaP}) \\
\frac{dm}{dt} &= \frac{m_\infty - m}{\tau_m} \\
\frac{dh}{dt} &= \frac{h_\infty - h}{\tau_h} \\
\frac{dj}{dt} &= \frac{j_\infty - j}{\tau_j} \\
\frac{dd}{dt} &= \frac{d_\infty - d}{\tau_d} \\
\frac{df_{11}}{dt} &= \frac{f_{11\infty} - f_{11}}{\tau_{f_{11}}} \\
\frac{df_{12}}{dt} &= \frac{f_{12\infty} - f_{12}}{\tau_{f_{12}}} \\
\frac{dCa_{inact}}{dt} &= \frac{Ca_{inact\infty} - Ca_{inact}}{\tau_{Ca_{inact}}} \\
\frac{dr}{dt} &= \frac{r_\infty - r}{\tau_r} \\
\frac{ds}{dt} &= \frac{s_\infty - s}{\tau_s} \\
\frac{ds_{slow}}{dt} &= \frac{s_{slow\infty} - s}{\tau_{s_{slow}}} \\
\frac{dr_{ss}}{dt} &= \frac{r_{ss\infty} - r_{ss}}{\tau_{r_{ss}}} \\
\frac{ds_{ss}}{dt} &= \frac{s_{ss\infty} - s_{ss}}{\tau_{s_{ss}}} \\
\frac{dy}{dt} &= \frac{y_\infty - y}{\tau_y} \\
\frac{dP_{C1}}{dt} &= -k_a^+ [Ca^{2+}]_{SS}^n P_{C1} + k_a^- P_{o1} \\
\frac{dP_{o1}}{dt} &= k_a^+ [Ca^{2+}]_{SS}^n P_{C1} - k_a^- P_{o1} - k_b^+ [Ca^{2+}]_{SS}^m P_{o1} + k_b^- P_{o2} - k_c^- P_{o1} + k_c^- P_{C2} \\
\frac{dP_{C2}}{dt} &= k_c^+ P_{o1} - k_c^- P_{C2} \\
\frac{dP_{o2}}{dt} &= k_b^+ [Ca^{2+}]_{SS}^m P_{o1} - k_b^- P_{o2} \\
\frac{d[HTRPNCa]}{dt} &= k_{htrpn}^+ [Ca^{2+}]_i ([HTRPN]_{tot} - [HTRPNCa]) - k_{htrpn}^- [HTRPNCa] \\
\frac{d[LTRPNCa]}{dt} &= k_{ltrpn}^+ [Ca^{2+}]_i ([LTRPN]_{tot} - [LTRPNCa]) - k_{ltrpn}^- [LTRPNCa] \\
\frac{d[Na^+]_i}{dt} &= -\frac{(I_{Na} + I_{BNa} + 3I_{NaCa} + I_{NaK} + I_{f,Na})}{V_{myo}F} \\
\frac{d[K^+]_i}{dt} &= -\frac{(I_{ss} + I_{BK} + I_t + I_{K1} + I_{f,K} - 2I_{NaK})}{V_{myo}F} \\
\frac{d[Ca^{2+}]_i}{dt} &= \beta_i \left( J_{xfer} - J_{up} - J_{trpn} - \frac{(I_{BCa} - 2I_{NaCa} + I_{CaP})}{2V_{myo}F} \right) \\
\frac{d[Ca^{2+}]_{SS}}{dt} &= \beta_{ss} \left( J_{rel} \frac{V_{JSR}}{V_{SS}} - J_{xfer} \frac{V_{myo}}{V_{SS}} - \frac{(I_{CaL})}{2V_{SS}F} \right) \\
\frac{d[Ca^{2+}]_{JSR}}{dt} &= \beta_{JSR} (J_{tr} - J_{rel}) \\
\frac{d[Ca^{2+}]_{NSR}}{dt} &= J_{up} \frac{V_{myo}}{V_{NSR}} - J_{tr} \frac{V_{JSR}}{V_{NSR}}
\end{aligned}$$

with parameter values defined as follows:

$$\begin{aligned}
I_{Na} &= g_{Na} m^3 h j (v - E_{Na}) \\
m_{\infty} &= \frac{1}{1 + e^{-\frac{(v+45)}{6.5}}} \\
h_{\infty} = j_{\infty} &= \frac{1}{1 + e^{-\frac{(v+76.1)}{6.07}}} \\
E_{Na} &= \frac{RT}{F} \ln \left( \frac{[Na^+]_o}{[Na^+]_i} \right) \\
\tau_m &= \frac{0.00136}{\frac{0.32(v+47.13)}{1 - e^{-0.1(v+47.13)}} + 0.08e^{-\frac{v}{11}}} \\
\text{if } v &\geq -40 \text{ mV} \\
\tau_h &= 0.0004537 \left( 1 + e^{-\frac{(v+10.66)}{11.1}} \right) \\
\tau_j &= \frac{0.01163 (1 + e^{-0.1(v+32)})}{e^{-2.535 \cdot 10^{-7} v}} \\
\text{else} \\
\tau_h &= \frac{0.00349}{0.135e^{-\frac{(v+80)}{6.8}} + 3.56e^{0.079v} + 3.1 \cdot 10^5 e^{0.35v}} \\
\tau_j &= \frac{0.00349}{\left( \frac{v+37.78}{1 + e^{0.311(v+79.23)}} (-127140e^{0.2444v} - 3.474 \cdot 10^{-5} e^{-0.04391v}) + \frac{0.1212e^{-0.01052v}}{1 + e^{-0.1378(v+40.14)}} \right)} \\
I_{CaL} &= g_{CaL} d \left( \left( 0.9 + \frac{Ca_{inact}}{10} \right) f_{11} + \left( 0.1 - \frac{Ca_{inact}}{10} \right) f_{12} \right) (v - E_{CaL}) \\
d_{\infty} &= \frac{1}{1 + e^{-\frac{(v+15.3)}{5}}} \\
f_{11\infty} = f_{12\infty} &= \frac{1}{1 + e^{-\frac{(v+26.7)}{5.4}}} \\
E_{CaL} &= 65 \\
\tau_d &= 0.00305e^{-0.0045(v+7)^2} + 0.00105e^{-0.002(v-18)^2} + 0.00025 \\
\tau_{f_{11}} &= 0.105e^{-((v+45)/12)^2} + \frac{0.04}{1 + e^{\frac{(25-v)}{25}}} + \frac{0.0015}{1 + e^{\frac{(v+75)}{25}}} + 0.0017 \\
\tau_{f_{12}} &= 0.041e^{-((v+47)/12)^2} + \frac{0.08}{1 + e^{-\frac{(v+55)}{5}}} + \frac{0.0015}{1 + e^{\frac{(v+75)}{25}}} + 0.0017 \\
Ca_{inact\infty} &= \frac{1}{1 + 100 [Ca^2+]_{SS}} \\
\tau_{Ca_{inact}} &= 0.009 \\
I_t &= g_t r (as + bs_{slow}) (v - E_K) \\
r_{\infty} &= \frac{1}{1 + e^{-\frac{(v+10.6)}{11.42}}} \\
s_{\infty} = s_{slow\infty} &= \frac{1}{1 + e^{\frac{(v+45.3)}{6.8841}}} \\
\tau_r &= \frac{1}{45.16e^{0.3577(v+50)} + 98.9e^{-0.1(v+38)}} \\
\tau_s &= 0.55e^{-\left(\frac{v+70}{25}\right)^2} + 0.049 \\
\tau_{s_{slow}} &= 3.3e^{-\left(\frac{v+70}{30}\right)^2} + 0.049 \\
E_K &= \frac{RT}{F} \ln \left( \frac{[K^+]_o}{[K^+]_i} \right) \\
I_{ss} &= g_{ss} r_{ss} s_{ss} (v - E_K) \\
r_{ss\infty} &= \frac{1}{1 + e^{-\frac{(v+11.5)}{11.82}}}
\end{aligned}$$

$$\begin{aligned}
s_{ss\infty} &= \frac{1}{1 + e^{\frac{(v+87.5)}{10.3}}} \\
\tau_{r_{ss}} &= \frac{10}{45.16e^{0.3577(v+50)} + 98.9e^{-0.1(v+38)}} \\
\tau_{s_{ss}} &= 2.1 \\
I_{K1} &= \left( \frac{48}{e^{\frac{(v+37)}{25}} + e^{-\frac{(v+37)}{25}}} + 10 \right) \left( \frac{0.001}{1 + e^{-\frac{(v-E_K-76.77)}{17}}} \right) \dots \\
&\quad + \frac{g_{K1}(v-E_K-1.73)}{\left( 1 + e^{\frac{1.613F(v-E_K-1.73)}{RT}} \right) \left( 1 + e^{-\frac{[K^+]_o - 0.9988}{0.124}} \right)} \\
I_f &= g_f y (f_{Na} (v - E_{Na}) + f_K (v - E_K)) \\
y_\infty &= \frac{1}{1 + e^{\frac{(v+138.6)}{10.48}}} \\
f_{Na} &= 0.2 \\
f_K &= 1 - f_{Na} \\
\tau_y &= \frac{1}{0.11885e^{\frac{(v+80)}{28.37}} + 0.56236e^{-\frac{(v+80)}{14.19}}} \\
I_{BNa} &= g_{BNa} (v - E_{Na}) \\
I_{BK} &= g_{BK} (v - E_K) \\
I_{BCa} &= g_{BCa} (v - E_{CaL}) \\
I_B &= I_{BNa} + I_{BK} + I_{BCa} \\
I_{NaK} &= \bar{I}_{NaK} \left( \frac{1}{1 + 0.1245e^{\frac{0.1VF}{RT}} + 0.0365\sigma e^{\frac{VF}{RT}}} \right) \left( \frac{[K^+]_o}{[K^+]_o + k_{m,K}} \right) \\
\sigma &= \frac{e^{\frac{[Na^+]_o}{67.3}} - 1}{7} \\
I_{CaP} &= \bar{I}_{CaP} \left( \frac{[Ca^{2+}]_i}{[Ca^{2+}]_i + 0.0004} \right) \\
I_{NaCa} &= k_{NaCa} \left( \frac{[Na^+]_i^3 [Ca^{2+}]_o e^{0.03743\gamma_{NaCa}v} - [Na^+]_i^3 [Ca^{2+}]_i e^{0.03743(\gamma_{NaCa}-1)v}}{1 + d_{NaCa} ([Na^+]_i^3 [Ca^{2+}]_i + [Na^+]_i^3 [Ca^{2+}]_o)} \right) \\
J_{rel} &= \nu_1 (P_{o1} + P_{o2}) ([Ca^{2+}]_{JSR} - [Ca^{2+}]_{SS}) \\
f_b &= \left( \frac{[Ca^{2+}]_i}{K_{fb}} \right)^{N_{fb}} \\
r_b &= \left( \frac{[Ca^{2+}]_{NSR}}{K_{rb}} \right)^{N_{rb}} \\
J_{up} &= K_{SR} \frac{\nu_{max} f_b - \nu_{max} r_b}{1 + f_b + r_b} \\
J_{tr} &= \frac{[Ca^{2+}]_{NSR} - [Ca^{2+}]_{JSR}}{\tau_{tr}} \\
J_{xfer} &= \frac{[Ca^{2+}]_{SS} - [Ca^{2+}]_i}{\tau_{xfer}} \\
J_{trpn} &= \frac{d[HTRPNCa]}{dt} + \frac{d[LTRPNCa]}{dt} \\
\beta_i &= \left( 1 + \frac{[CMDN]_{tot} K_m^{CMDN}}{(K_m^{CMDN} + [Ca^{2+}]_i)^2} + \frac{[EGTA]_{tot} K_m^{EGTA}}{(K_m^{EGTA} + [Ca^{2+}]_i)^2} \right)^{-1} \\
\beta_{SS} &= \left( 1 + \frac{[CMDN]_{tot} K_m^{CMDN}}{(K_m^{CMDN} + [Ca^{2+}]_{SS})^2} \right)^{-1} \\
\beta_{JSR} &= \left( 1 + \frac{[CSQN]_{tot} K_m^{CSQN}}{(K_m^{CSQN} + [Ca^{2+}]_{JSR})^2} \right)^{-1}
\end{aligned}$$

$$[Na^+]_o = 140 \text{ mM}$$

$$[Ca^{2+}]_o = 1.2 \text{ mM}$$

$$[K^+]_o = 5.4 \text{ mM}$$

$$V_{cell} = 16 \text{ pL}$$

$$V_{nucleus} = 0.32 \text{ pL}$$

$$V_{mitochondria} = 5.76 \text{ pL}$$

$$V_{SS} = 0.0012 \cdot 10^{-6} \text{ pL}$$

$$V_{SR} = 0.56 \cdot 10^{-6} \text{ pL}$$

$$V_{JSR} = 0.056 \cdot 10^{-6} \text{ pL}$$

$$V_{NSR} = 0.504 \cdot 10^{-6} \text{ pL}$$

$$V_{myo} = 9.36 \cdot 10^{-6} \text{ pL}$$

$$C_m = 0.0001 \text{ } \mu\text{F}$$

$$F = 96487 \text{ coulombs/mol (Faraday's Constant)}$$

$$T = 295 \text{ }^\circ\text{K (absolute temperature)}$$

$$R = 8314.5 \text{ mJ/(mol}\cdot^\circ\text{K) (ideal gas constant)}$$

$$g_{Na} = 1.33 \cdot 0.8 \text{ } \mu\text{S}$$

$$g_{CaL} = 0.031 \text{ } \mu\text{S}$$

$$g_t = 0.4647 \cdot 0.035 \text{ } \mu\text{S}$$

$$g_{ss} = 0.007 \text{ } \mu\text{S}$$

$$g_{K1} = 0.024 \text{ } \mu\text{S}$$

$$g_{BNa} = 0.00008015 \text{ } \mu\text{S}$$

$$g_{BCa} = 0.0000324 \text{ } \mu\text{S}$$

$$g_{BK} = 0.000138 \text{ } \mu\text{S}$$

$$g_f = 0.00145 \text{ } \mu\text{S}$$

$$\bar{I}_{NaK} = 0.08 \text{ nA}$$

$$K_{m,Na} = 10 \text{ mM}$$

$$K_{m,K} = 1.5 \text{ mM}$$

$$\bar{I}_{CaP} = 0.004 \text{ nA}$$

$$k_{NaCa} = 0.000009984 \text{ mM}^{-4}$$

$$d_{NaCa} = 0.0001 \text{ mM}^{-4}$$

$$a = 0.583$$

$$b = 0.417$$

$$\gamma_{NaCa} = 0.5$$

$$\begin{aligned}
\tau_{sss} &= 2.1 \text{ sec} \\
E_{CaL} &= 65 \text{ mV} \\
\tau_{Ca_{inact}} &= 0.009 \text{ sec} \\
\nu_1 &= 1800 \text{ sec}^{-1} \\
K_{fb} &= 0.000168 \text{ mM} \\
K_{rb} &= 3.29 \text{ mM} \\
K_{SR} &= 1 \\
N_{fb} &= 1.2 \\
N_{rb} &= 1 \\
V_{maxf} &= 0.04 \text{ mM} \cdot \text{sec}^{-1} \\
V_{maxr} &= 0.9 \text{ mM} \cdot \text{sec}^{-1} \\
\tau_{tr} &= 0.0005747 \text{ sec} \\
\tau_{xfer} &= 0.0267 \text{ sec} \\
k_a^+ &= 1215000000000 \text{ mM}^{-4} \text{ sec}^{-1} \\
k_a^- &= 576 \text{ sec}^{-1} \\
k_b^+ &= 4050000000 \text{ mM}^{-3} \text{ sec}^{-1} \\
k_b^- &= 1930 \text{ sec}^{-1} \\
k_c^+ &= 100 \text{ sec}^{-1} \\
k_c^- &= 0.8 \text{ sec}^{-1} \\
LTRPN_{tot} &= 0.07 \text{ mM} \\
HTRPN_{tot} &= 0.14 \text{ mM} \\
k_{htrpn}^+ &= 200000 \text{ mM}^{-1} \text{ sec}^{-1} \\
k_{htrpn}^- &= 0.066 \text{ sec}^{-1} \\
k_{itrpn}^+ &= 40000 \text{ mM}^{-1} \text{ sec}^{-1} \\
k_{itrpn}^- &= 40 \text{ sec}^{-1} \\
CMDN_{tot} &= 0.05 \text{ mM} \\
CSQN_{tot} &= 15 \text{ mM} \\
EGTA_{tot} &= 10 \text{ mM} \\
K_m^{CMDN} &= 0.00238 \text{ mM} \\
K_m^{CSQN} &= 0.8 \text{ mM} \\
K_m^{EGTA} &= 0.00015 \text{ mM}
\end{aligned}$$

## REFERENCES

- [1] Lu, T., Lee, H.-C., Kabat, J. & Shibata, E. Modulation of rat cardiac sodium channel by the stimulatory g protein alpha subunit. *J. Physiol.* **518**, 371–384 (1999).
- [2] Palygin, O. A., Pettus, J. M. & Shibata, E. F. Regulation of caveolar cardiac sodium current by a single  $g_s\alpha$  histidine residue. *Am. J. Physiol. Heart Circ. Physiol.* **294**, H1693–H1699 (2008).
- [3] Vatta, M. *et al.* Mutant caveolin-3 induces persistent late sodium current and is associated with long-qt syndrome. *Circulation* **114**, 2104–2112 (2006).
- [4] Zaza, A. *The cardiac action potential*, chap. 3 (CRC press, 2000).
- [5] Aidley, D. J. *The Physiology of Excitable Cells* (Cambridge University Press, 1998), 4 edn.
- [6] Hille, B. *Ionic Channels of Excitable Membranes* (Sinauer Associates, 1991), 2 edn.
- [7] Bennett, P. B. & Johnson, J. *Molecular physiology of cardiac ion channels*, chap. 2 (CRC press, 2000).
- [8] Berne, R. M. & Levy, M. N. *Electrical activity of the heart*, chap. 22 (Mosby, 1998), 4 edn.
- [9] Murphy, R. A. *Contractile mechanism of muscle cells*, chap. 17 (Mosby, 1998), 4 edn.
- [10] Berne, R. M. & Levy, M. N. *The circuitry*, chap. 21 (Mosby, 1998), 4 edn.
- [11] Hodgkin, A. & Huxley, A. A quantitative description of membrane currents and its application to conduction and excitation in nerve. *J. Physiol.* **117**, 500–544 (1952).
- [12] DiFrancesco, D. & Noble, D. A model of cardiac electrical activity incorporating ionic pumps and concentration changes. *Phil. Trans. R. Soc. Lond. B* **307**, 353–398 (1985).

- [13] McAlister, R., Noble, D. & Tsien, R. Reconstruction of the electrical activity of cardiac purkinje fibers. *J. Physiol.* **251**, 1–59 (1975).
- [14] Beeler, G. W. & Reuter, H. Reconstruction of the action potential of ventricular myocardial fibres. *J. Physiol.* **268**, 177–210 (1977).
- [15] Luo, C. & Rudy, Y. A model of the ventricular cardiac action potential. depolarization, repolarization, and their interaction. *Cir. Res.* **68**, 1501–1526 (1991).
- [16] Keener, J. & Sneyd, J. *Mathematical physiology*, vol. 8 of *Interdisciplinary Applied Mathematics* (Springer-Verlag, New York, 1998).
- [17] Pandit, S., Clark, R., Giles, W. & Demir, S. A mathematical model of action potential heterogeneity in adult rat left ventricular myocytes. *Biophysical Journal* **81**, 3029–3051 (2001).
- [18] Mitchell, C. & Schaeffer, D. A two-current model for the dynamics of cardiac membrane. *Bull. Math. Bio.* **65**, 767–793 (2003).
- [19] Shibata, E. F. Personal communication.
- [20] Yarbrough, T., Lu, T., Lee, H.-C. & Shibata, E. Localization of cardiac sodium channels in caveolin-rich membrane domains: regulation of sodium current amplitude. *Circ. Res.* **90**, 443–449 (2002).
- [21] Shibata, E. *et al.* Autonomic regulation of voltage-gated cardiac ion channels. *J. Cardiovasc. Electrophysiol.* **17**, S34–S42 (2006).
- [22] Salpeter, S. R., Ormiston, T. M. & Salpeter, E. E. Cardiovascular effects of  $\beta$ -agonists in patients with asthma and copd: a meta-analysis. *Chest* **125**, 2309–2321 (2004).
- [23] Rosen, M. R., Pinto, J. M. & Boyden, P. A. *Neurohumoral modulation of cardiac electrophysiology*, chap. 5 (CRC press, 2000).
- [24] Walton, M. K. & Fozzard, H. A. Experimental study of the conducted action potential in cardiac purkinje strands. *Biophys. J.* **44**, 1–8 (1983).
- [25] Yamaoka, K. Does the maximum upstroke velocity of the action potential ( $\dot{V}_{max}$ ) represent available sodium conductance in frog ventricular cells? *Japanese J. Physiol.* **37**, 585–599 (1987).
- [26] Walton, M. K. & Fozzard, H. A. The conducted action potential: models and comparison to experiments. *Biophys. J.* **44**, 9–26 (1983).

- [27] Hunter, P., McNaughton, P. & Noble, D. Analytical models of propagation in excitable cells. *Prog. Biophys. Mol. Biol.* **30**, 99–144 (1975).
- [28] Brette, F. & Orchard, C. Density and sub-cellular distribution of cardiac and neuronal sodium channel isoforms in rat ventricular myocytes. *Biochemical and Biophysical Research Communications* **348**, 1163–1166 (2006).
- [29] Levin, K. & Page, E. Quantitative studies on plasmalemmal folds and caveolae of rabbit ventricular myocardial cells. *Circ Res* **46**, 244–255 (1980).
- [30] Luo, C. & Rudy, Y. A dynamic model of the cardiac ventricular action potential. i. simulations of ionic currents and concentration changes. *Circ. Res.* **74**, 1071–1096 (1994).
- [31] Albitz, R., Droogmans, G. & Nilius, B. The conductance of single cardiac sodium channels from guinea pig depends of the intracellular sodium concentration **1068**, 254–256 (1991).
- [32] Fitzhugh, R. Impulses and physiological states in theoretical models of nerve membrane. *Biophys. J.* **1**, 445–466 (1961).
- [33] Nagumo, J., Arimoto, S. & Yoshizawa, S. An active pulse transmission line simulating nerve axon. *Proc IRE.* **50**, 2061–2070 (1962).
- [34] Fenton, F. & Karma, A. Vortex dynamics in three-dimensional continuous myocardium with fiber rotation: Filament instability and fibrillation. *Chaos* **8**, 20–47 (1998).
- [35] Karma, A. Electrical alternans and spiral wave breakup in cardiac tissue. *Chaos* **4**, 461–472 (1994).
- [36] Hall, G., Bahar, S. & Gauthier, D. Prevalence of rate-dependent behaviors in cardiac muscle. *Phys. Rev. Lett.* **82**, 2995–3998 (1999).
- [37] Cagliani, R. *et al.* A cav3 microdeletion differentially affects skeletal muscle and myocardium. *Neurology* **61**, 1513–1519 (2003).
- [38] De Paula, F. *et al.* Mutations in the caveolin-3 gene: When are they pathogenic? *Am J Med Genetics* **99**, 303–307 (2001).
- [39] Hnasko, R. & Lisanti, M. Lessons from caveolin knockout mice and implications for human disease. *Mol Interventions* **3**, 445–464 (2003).

- [40] Woodman, S. *et al.* Caveolin-3 knock-out mice develop a progressive cardiomyopathy and show hyperactivation of the p42/44 mapk cascade. *J Biol Chem* **277**, 38988–38997 (2002).
- [41] Park, D. *et al.* Caveolin-1/3 double-knockout mice are viable, but lack both muscle and non-muscle caveolae, and develop a severe cardiomyopathic phenotype. *Am J Path* **160**, 2207–2217 (2002).
- [42] Cronk, L. *et al.* Novel mechanism for sudden infant death syndrome: Persistent late sodium current secondary to mutations in caveolin-3. *Heart Rhythm* **4**, 161–166 (2007).
- [43] Balijepallie, R. & Kamp, T. Caveolae, ion channels and cardiac arrhythmias. *Prog. Biophys. Mol. Biol.* **98**, 149–160 (2008).
- [44] Ross, S. *A First Course in Probability* (Prentice Hall, 2001), 6 edn.